

Electronic Thesis and Dissertation Repository

11-11-2019 2:30 PM

Micromechanics of plasticity of Zr-2.5%Nb alloy

Md Imran Khan, *The University of Western Ontario*

Supervisor: Klassen, Robert Jay, *The University of Western Ontario*

A thesis submitted in partial fulfillment of the requirements for the Doctor of Philosophy degree in Mechanical and Materials Engineering

© Md Imran Khan 2019

Follow this and additional works at: <https://ir.lib.uwo.ca/etd>



Part of the [Other Materials Science and Engineering Commons](#)

Recommended Citation

Khan, Md Imran, "Micromechanics of plasticity of Zr-2.5%Nb alloy" (2019). *Electronic Thesis and Dissertation Repository*. 6730.

<https://ir.lib.uwo.ca/etd/6730>

This Dissertation/Thesis is brought to you for free and open access by Scholarship@Western. It has been accepted for inclusion in Electronic Thesis and Dissertation Repository by an authorized administrator of Scholarship@Western. For more information, please contact wlsadmin@uwo.ca.

Abstract

Zirconium alloys are used in many thermal neutron fission reactors because of their very low neutron interaction cross-sections along with their excellent mechanical strength and corrosion resistance. Numerous experiments have been conducted on these alloys at the bulk scale to determine their mechanical properties. Recent advancements in micro-mechanical testing make it easier to study site specific mechanical properties for micron or submicron sized samples. Understanding the mechanical response of such small volumes of material is extremely important for developing accurate models to predict the ductile fracture toughness of these in-reactor materials. Pressure tubes made of Zr-2.5%Nb alloys are integral part of the CANDU reactors as they carry the fissile uranium fuel bundles and also transport the heavy water coolant to the core. During services in the reactor the insides surface of these tubes can develop micron sized scratches due to repeated sliding motion of the fuel bundles. In order to properly assess the impact of these flaws in the long run, good understanding of localized plastic deformation in very small regions near these surface scratches is important. Uniaxial compression tests were performed on 1 μ m diameter micro-pillars fabricated from the axial normal (AN) and transverse normal (TN) planes of an extruded and 22% cold-drawn Zr-2.5%Nb CANDU pressure tube to assess the effect of crystallographic orientations, α/β interfaces, irradiation temperature, and deformation temperature on the mechanical anisotropy and active plastic deformation mechanisms. Some of the micro-pillars were implanted with 8.5MeV Zr⁺ ions at room temperature and 300°C to simulate the effect of neutron irradiation. For the non-implanted α_{Zr} pillars compressed at 25°C the flow stress at 10% strain, $\sigma_{\varepsilon=10\%}$ was significantly higher than that reported for larger diameter

polycrystalline Zr-2.5%Nb pillars demonstrating the length-scale dependence of the mechanical strength of this material. The increasing of the Zr^{+} implantation temperature to 300°C results in reduced strength and onset of brittle cracking of the micropillars. This is attributed to the effect of concurrent thermal recovery of the implantation-induced crystal damage at 300°C on facilitating strain localization. The mechanical anisotropy of the micro-pillars was reduced as a result of increased implantation and test temperature. Strain hardening exponent, n varied between 0.2-0.3 for all test conditions. Increased serrations were observed in the stress-strain response of micropillars that were implanted at higher temperature (300°C). Resolved shear stress (RSS) for pillars oriented with the loading direction at various angles of misorientation relative to the basal plane normal was plotted and it was observed that the values follow a trend predicted by a mathematical/computational model involving deformation by simultaneous dislocation glide and twinning. Presence of α/β interface resulted in lowering of compressive strength for high temperature implanted and test samples. These observations, and the acquired test data reported in this thesis, are of significant benefit to the nuclear industry in performing accurate, ductile fracture toughness based life-time assessments of Zr-2.5% Nb pressure tubes currently operating in CANDU reactors.

Keywords

Zr-2.5%Nb CANDU pressure tubes; Zr^{+} ion implantation; micro-pillar; micro-compression; anisotropy; crystallographic orientation; high temperature test; micro-mechanical testing.

Summary for Lay Audience

Ontario relies greatly on nuclear energy for electricity generation. Approximately 60% of Ontario's power supply is generated by pressurized heavy water moderated nuclear reactors popularly known as CANDU reactors. One of the most critical components of these reactors are the pressure tubes made of the Zr-2.5%Nb alloy. During the operation of the reactors, the inside temperature of the pressure tube is about 300°C and the internal pressure is about 10 MPa. For the safe operation of the reactors, it is important to know the mechanical properties of the pressure tube materials at different temperatures and irradiation conditions. Mechanical properties of these tubes are known from tests performed on bulk samples (sample size bigger than a few millimeters). With the advancement of material testing technology, now it is possible to conduct experiments on very small sized samples (micrometer or nanometer). Information obtained from the experimental testing of micron sized samples can be used to improve the mathematical models for better prediction of material properties. In this project, we have prepared micron sized samples by using Focused Ion Beam-FIB milling and this allowed us to prepare mechanical test samples of single grains, and multiple grains with well characterized interfaces. These tiny samples were implanted with zirconium ions to simulate in-reactor neutron irradiation. We observed that the stress-strain values obtained are significantly different from the previously published values for bulk samples prepared from the same material. Also, we noticed that the interfaces behave differently during the deformation process for implanted and non-implanted samples. All these information will be valuable for proper maintenance of existing pressure tubes located in CANDU reactors.

Co-Authorship Statement

The thesis is written in a manuscript format. It contains three manuscripts, two of them are submitted and the other one will be submitted soon.

1) Md. Imran Khan and R. J. Klassen, Effect of Zr⁺ implantation and crystal orientation on the uniaxial deformation of Zr-2.5%Nb micro-pillars: Part 1, Deformation of single-phase α -Zr micro-pillars, submitted in Canadian Metallurgical Quarterly

2) Md. Imran Khan and R. J. Klassen, Effect of Zr⁺ implantation and crystal orientation on the uniaxial deformation of Zr-2.5%Nb micro-pillars: Part 2, Deformation of two-phase α/β micro-pillars, submitted in Canadian Metallurgical Quarterly

3) Md. Imran Khan and R. J. Klassen Deformation of Zr⁺ implanted Zr-2.5%Nb alloy at 250°C, to be submitted in Journal of Nuclear Materials

The research experiments were designed and performed by the candidate. In addition to that, the candidate performed data analysis, prepared draft manuscripts and corrected the manuscripts according to the suggestions of the supervisor, Dr Robert J. Klassen. Dr Robert J. Klassen gave suggestions regarding the interpretation of data and edited the manuscripts.

The help of the following people is gratefully acknowledged in different steps of samples preparation and experimentation. Dr. Todd Simpson helped in fabrication of the micro-pillars, Ivan Barker helped in EBSD mapping and Jack Hendricks assisted in ion implantation of the samples. Qingshan Dong helped me while conducting experiments at Queen's University and Dr Vineet Bhakhri helped during the experimental work at CNL.

Acknowledgments

I would like to thank my supervisor Dr Robert Klassen for his support and guidance throughout the course of my doctoral studies. I liked his open-door policy for the students. I had countless informal meetings with him, which helped me immensely to shape my thinking process.

I am thankful to all my group members. Dr Vineet Bhakhri helped me a lot in the beginning of my PhD journey. Dr AZM Ariful Islam and Dr Bipasha Bose were always there for useful discussions. Special thanks to Aria Khalili for helping me in some experimental works. I shared the office room SEB 2014 for a long time with Maissaa Tawfeeq, Meghan Balsdon, and Mahdi Bagheripoor. I would like to thank them all for our everyday conversations which made my life less stressful. I needed help from a number of people while preparing my samples. I would like to thank Ivan Barker from the Zaplab, Dr Todd Simpson from the nano-fabrication laboratory, and Jack Hendricks from the Tandetron laboratory. I am immensely grateful to Dr Hamid Abdolvand for his important discussions and help with some of the calculations.

Special thanks to the Bangladeshi community members living in London. They have made my life easier in every possible way they could. Life was difficult at times, as me and my wife Tammeen Siraj continued our PhD journey at Western University with our only daughter Ilham Khan. I had my PhD qualifier exam when Ilham was just 20 days old, now she is all set to start her kindergarten from September 2019. I would take this opportunity to thank my wife and daughter for supporting me throughout the journey.

Finally, I would like to thank my parents and siblings back home in Bangladesh, for the everyday skype calls.

Table of Contents

Abstract	ii
Summary for Lay Audience	iv
Co-Authorship Statement.....	v
Acknowledgments.....	vi
Table of Contents	viii
List of Tables	xii
List of Figures	xiii
List of Abbreviations	xviii
Chapter 1	1
1 Introduction	1
1.1 Structure of thesis	2
1.2 Novelties of this research:.....	3
References	4
Chapter 2.....	6
2 Literature Review.....	6
2.1 The operation of a CANDU reactor.....	6
2.2 Anisotropic deformation of Zr-2.5%Nb pressure tubes:.....	11
2.3 Size effects on the strength and ductility of metals	14
2.4 Micro-mechanical testing.....	18
2.5 Effect of particle irradiation on the mechanical response of Zirconium alloys:...	22
2.6 Effect of grain boundaries.....	24
2.7 Effect of particle irradiation on the microstructure of Zr alloys.....	26
2.8 Mechanical testing of Zr alloys at different length scales	28
2.9 Summary	36

References	37
Chapter 3.....	49
3 Experimental Design and Techniques.....	49
3.1 Material.....	49
3.2 Micropillar fabrication.....	50
3.3 Electron Backscattered Diffraction (EBSD).....	51
3.4 Ion implantation.....	53
3.5 Micro-compression.....	55
References	55
Chapter 4.....	57
4 Effect of Zr ⁺ irradiation damage and crystal orientation on the uniaxial deformation of Zr-2.5%Nb micro-pillars: Part 1, Deformation of single-phase α_{Zr} micro-pillars.....	57
4.1 Introduction.....	58
4.2 Procedure.....	61
4.3 Results.....	65
4.4 Discussion.....	74
4.4.1 Length-scale dependence of the average flow stress.....	79
4.4.2 Orientation dependence of the critical resolved shear stress.....	80
4.4.3 Other sources contributing to variability in the $\tau\varepsilon = 10\%$ - θ trend.....	82
4.5 Conclusions.....	84
4.6 Acknowledgements.....	86
References	86
Chapter 5.....	89
5 Effect of Zr ⁺ implantation and crystal orientation on the uniaxial deformation of Zr-2.5%Nb micro-pillars: Part 2, Deformation of two-phase α_{Zr}/β_{Nb} micro-pillars....	89

5.1	Introduction.....	89
5.2	Procedure	91
5.3	Results.....	95
5.4	Discussion.....	102
5.4.1	Role of the α_{Zr}/β_{Nb} interface on the average micro-pillar flow stress.....	102
5.4.2	Orientation dependence of the critical resolved shear stress	106
5.5	Conclusions.....	111
5.6	Acknowledgements.....	113
	References	114
	Chapter 6.....	116
6	Deformation of Zr^{+} implanted Zr-2.5%Nb alloy at 250°C	116
6.1	Introduction.....	117
6.2	Procedure	118
6.3	Results.....	121
6.4	Discussion.....	119
6.4.1	Cracking of Zr^{+} implanted micro-pillars.....	119
6.4.2	Effect of testing temperature on $\sigma_{0.2\%}$ of non-implanted micro-pillars.....	121
6.4.3	Effect of testing temperature on $\sigma_{0.2\%}$ of Zr^{+} implanted micro-pillars	122
6.4.4	Effect of Zr^{+} implantation and testing temperature on strain hardening of micro-pillars.....	124
6.4.5	Orientation dependence of $\tau_{0.2\%}$ of α -phase deformation at 250°C...	125
6.5	Conclusions.....	128
6.6	Acknowledgements.....	131
	References	131
	Chapter 7.....	136

7 Discussion and Future Works	136
7.1 Discussions	136
7.2 Future Works	139
Curriculum Vitae	141

List of Tables

Table 2.1: CRSS for basal, prismatic, pyramidal slip and twinning of αZr	13
Table 3.1: Experimental matrix	51
Table 4.1: Listing of micro-pillar compression tests performed in this study.....	65
Table 4.2: Listing of orientation angle θ between the axial loading direction and the $\langle 0001 \rangle$ crystal direction for the various αZr micro-pillars tested in compression at 25°C . Also shown are the calculated Schmid factors, m , associated with deformation by dislocation slip along the basal, prismatic, pyramidal slip systems, and compressive twinning. Also shown is the calculated critical resolved shear stress $\tau_{\varepsilon=0.10}$ determined as the product of the maximum calculated Schmid factor and the measured normal flow stress $\sigma_{\varepsilon=0.10}$	72
Table 4.3: Listing of orientation angle θ between the axial loading direction and the $\langle 0001 \rangle$ crystal direction for the various αZr micro-pillars implanted at 25°C and tested in compression at 25°C . Also shown are the calculated Schmid factors, m , associated with deformation by dislocation slip along the basal, prismatic, pyramidal slip systems, and compressive twinning. Also shown is the calculated critical resolved shear stress $\tau_{\varepsilon=0.10}$ determined as the product of the maximum calculated Schmid factor and the measured normal flow stress $\sigma_{\varepsilon=0.10}$	72
Table 4.4: Listing of orientation angle θ between the axial loading direction and the $\langle 0001 \rangle$ crystal direction for the various αZr micro-pillars implanted at 250°C and tested in compression at 25°C . Also shown are the calculated Schmid factors, m , associated with deformation by dislocation slip along the basal, prismatic, pyramidal slip systems, and compressive twinning. Also shown is the calculated critical resolved shear stress $\tau_{\varepsilon=0.10}$ determined as the product of the maximum calculated Schmid factor and the measured normal flow stress $\sigma_{\varepsilon=0.10}$	73
Table 5.1: Listing of the micro-pillar compression tests performed.....	94
Table 5.2: Approximate resolved shear stress ($\tau\varepsilon = 0.10\text{Eq. 1}$), basal misorientation angle θ of the α -phase of each of the $\alpha\text{Zr}/\beta\text{Nb}$ micro-pillars.	101
Table 6.1: Listing of micro-pillar compression tests performed in this study	121
Table 6.2: Listing of initial yield stress ($\sigma_{0.2\%}$), flow stress at 10% strain ($\sigma_{10\%}$), stress difference ($\Delta\sigma = \sigma_{10\%} - \sigma_{0.2\%}$), θ direction of the α -phase corresponding to the axial direction of the micro-pillar, maximum calculated Schmid factor m , and the critical resolved shear stress ($\tau_{0.2\%}$) for all the micro-pillars tested in this study	118

List of Figures

Figure 2.1: Schematic of a CANDU reactor core [4]	7
Figure 2.2: Schematic of a CANDU fuel channel [5].....	8
Figure 2.3: Zr-Nb binary phase diagram [6]. The vertical red line represents the position of the Zr-2.5%Nb pressure tube alloy	9
Figure 2.4: Schematic of Zr-2.5%Nb alloy microstructure	9
Figure 2.5: Schematic of Zr-2.5%Nb pressure tube section showing different directions of the pressure tube.	10
Figure 2.6: Typical grain structure of Zr-2.5%Nb pressure in CAUDU reactors. The light-colored α_{Zr} grains are surrounded by thin layer of dark-colored $\alpha_{\text{Zr}}/\beta_{\text{Nb}}$ eutectoid lamella [7].....	10
Figure 2.7: Transmission electron micrographs from carbon replicas of a pressure tube showing: (a) elongated α -grains in the axial/radial section and (b) curved flattened α -grains in the radial/transverse section[8]	11
Figure 2.8: (0001) basal pole figure of an extruded and cold drawn Zr-2.5%Nb CANDU pressure tube [10].....	12
Figure 2.9: Possible dislocation slip systems and twinning systems in hcp crystals [14] 14	
Figure 2.10: Load–displacement curves (with inferred secondary stress axis) obtained from in situ SEM compressive loading of both as-received (AR1) and hydride-containing (H1, H2) micropillars [22]	15
Figure 2.11: Typical load-displacement curves of micro-scale pre-cracked cantilevers tested at room temperature [24]	17
Figure 2.12: Dependence of yield stress on fluence [51].....	23
Figure 2.13: Comparison of ion implanted and un-implanted sample [52].....	24
Figure 2.14: (a) Tensile flow curves of pressure tube material tested in the axial direction (b) Tensile flow curves of pressure tube material tested in the transverse direction [75] 31	
Figure 2.15: Typical flow curves for irradiated specimens for transverse and longitudinal directions at 250°C [1].....	32

- Figure 2.16: Typical true stress versus true strain curves obtained from uniaxial compression of 5 μm diameter Zr-2.5%Nb micro-pillars in: (a) the non-irradiated condition and (b) after Zr^+ ion irradiation[79]..... 35
- Figure 2.17: Engineering stress-strain curves of (a) AD and (b) TD samples [65] 36
- Figure 3.1: Schematic diagram of the pressure tube depicting the orientation of the Axial Normal (AN), Radial Normal (RN), and Transverse Normal (TN) planes. The predominant orientation of the hexagonal unit cell of the α -phase is shown in red [1].... 50
- Figure 3.2: Schematic representation of basal misorientation angle, θ 53
- Figure 3.3: Irradiation damage profile of the micropillar 54
- Figure 4.1: Illustration of curved compact tension specimen used for measuring fracture toughness of hydrides. 60
- Figure 4.2: The fracture surface of a curved compact tension specimens machined from an irradiated Zr-2.5Nb pressure tube. These specimens were tested at 150 °C. Transverse cracks formed by the fracture of circumferential hydrides and the corresponding inter-hydride ligament of Zr-2.5Nb are indicated. Crack growth is from left-to-right beginning at the tip of the pre-test fatigue crack..... 60
- Figure 4.3: Diagram of an hcp unit cell depicting the basal0001, prismatic1010, and pyramidal 1011 slip planes along which dislocation glide occurs..... 61
- Figure 4.4: SEM images showing the microstructure of the (a) AN and (b) TN planes of the Zr-2.5%Nb pressure tube material. Large α -Zr grain regions, such as those indicated by the arrows, were selected from which to fabricate the single-crystal α -Zr micro-pillars. 62
- Figure 4.5: Typical 1 μm diameter FIB milled α -Zr micro-pillars made from the AN plane of the pressure tube: (a) before, (b) after uniaxial compression showing dislocation slip along a single plane, and (c) after compression showing slip along multiple crystal planes. 63
- Figure 4.6: True stress versus true strain curves for the non-implanted α_{Zr} micro-pillars fabricated from the (a) AN and (b) TN planes of the Zr-2.5%Nb pressure tube..... 68
- Figure 4.7: True stress versus true strain curves for the Zr^+ -implanted $\psi \approx 6.0 \text{ dpa @ } 250\text{C}$ α_{Zr} micro-pillars fabricated from the (a) AN and (b) TN planes of the Zr-2.5%Nb pressure tube. 70

- Figure 4.8: True stress versus true strain for the Zr^{+} -implanted $\psi \approx 6.0 \text{ dpa @} 300^{\circ}\text{C}$ α_{Zr} micro-pillars fabricated from the (a) AN and (b) TN planes of the Zr-2.5%Nb pressure tube..... 72
- Figure 4.9: Histogram representation of the average flow stress ($\epsilon = 10\%$) of the α_{Zr} micro-pillars..... 75
- Figure 4.10: Histogram representation of the average strain-hardening exponent n of the α_{Zr} micro-pillars..... 76
- Figure 4.11: Strain hardening rate $d\sigma/d\epsilon$ versus true strain for the α_{Zr} micropillars in the: (a) non-implanted, (b) Zr^{+} -implanted (25°C), and (c) Zr^{+} -implanted (300°C) conditions.78
- Figure 4.12: Average flow stress $\sigma_{\epsilon = 10\%}$, plotted versus pillar diameter for AN and TN Zr-2.5%Nb pillars. The data for the 5 μm and 2 mm diameter polycrystalline pillars are from Ref [15] [16], 2 μm pillars are from Ref [18](these values were reported for $\sigma_{\epsilon = 4\%}$)..... 80
- Figure 4.13: Calculated $\tau_{\epsilon = 10\%}$ (Eq. 2) versus basal misorientation angle θ for all the α -Zr micro-pillars tested in this study..... 83
- Figure 4.14 : Normalized resolved shear stress $\tau_{\epsilon = 10\%}$ versus basal misorientation angle θ for α -Zr micro-pillars selected for strong single-slip or twinning. The data from micro-pillars fabricated from the TN and AN planes of the Zr-2.5Nb pressure tube are identified for each of the three Zr^{+} implantation conditions studied. The $\tau_{\epsilon = 10\%} - \theta$ trend predicted by the computational model of Abdolvand et al.[11] for deformation of hcp α -Zr via concurrent mechanisms of dislocation slip and twinning is shown by the solid line..... 84
- Figure 5.1:Microstructure, on the TN plane, of the extruded and cold-drawn Zr-2.5%Nb pressure tube. The red circle in the inset depicts an α/β region typical of that from which α/β micro-pillars were fabricated. 92
- Figure 5.2: Schematic depiction of the typical microstructure found on the top surface of an α_{Zr}/β_{Nb} micro-pillar..... 93
- Figure 5.3: Typical FIB milled α_{Zr}/β_{Nb} micro-pillar made from the TN plane of a non-implanted Zr-2.5%Nb pressure tube 93
- Figure 5.4: True stress versus true strain curves of the non-implanted TN micro-pillars.96

Figure 5.5: True stress versus true strain for the Zr^{+} -implanted $\psi \approx 6.0 dpa @250C$ α/β -Zr micro-pillars fabricated from (a) the AN plane and (b) the TN plane of the Zr-2.5%Nb pressure tube.	98
Figure 5.3: True stress versus true strain for the Zr^{+} -implanted $\psi \approx 6.0 dpa @300oC$ α/β -Zr micro-pillars fabricated from (a) the AN plane and (b) the TN plane of the Zr-2.5%Nb pressure tube.	100
Figure 5.4: TN-oriented α/β micro-pillars compressed at 25°C: (a) non-implanted, (b) Zr^{+} -implanted ($\psi \approx 6dpa$) at 25°C, (c) Zr^{+} -implanted ($\psi \approx 6dpa$) at 300°C.....	100
Figure 5.8: Effect of Zr^{+} implantation on σ ($\varepsilon = 0.10$) of the α/β micro-pillars and α_{Zr} micro-pillars [3] made from the AN and TN planes of a Zr-2.5%Nb pressure tube.	104
Figure 5.9: Plots of rate of change of flow stress with respect to strain, $d\sigma/d\varepsilon$, versus true strain for TN α/β micro-pillars in: a) non-implanted condition, b) Zr^{+} implanted ($\psi \approx 6dpa$) at 25°C, and c) Zr^{+} implanted ($\psi \approx 6dpa$) at 300°C.	106
Figure 5.10: Variation in the normalized critical resolved shear stress $\tau\varepsilon = 0.10$ (Eq. 3) with basal misorientation angle θ for α/β micro-pillars in the: a) non-implanted condition, b) Zr^{+} implanted ($\psi \approx 6dpa$) at 25°C, and c) Zr^{+} implanted ($\psi \approx 6dpa$) at 300°C. The solid line represents the trend predicted by the model of Abdolvand et al. [11]	111
Figure 6.1: SEM image of a typical α_{Zr} -phase micro-pillar.....	119
Figure 6.2: True stress versus true strain response of the TN-oriented non-implanted α_{Zr} micro-pillars compressed at 250°C.....	123
Figure 6.3: True stress versus true strain response for TN-oriented non-implanted α_{Zr} / β_{Nb} micro-pillars compressed at 250°C.....	123
Figure 6.4: True stress versus true strain response for TN-oriented Zr^{+} implanted α_{Zr} micro-pillars compressed at 250°C.....	124
Figure 6.5: True stress versus true strain response for TN-oriented Zr^{+} implanted α_{Zr} / β_{Nb} micro-pillar compressed at 250°C	125
Figure 6.6 : True stress versus true strain response for AN-oriented Zr^{+} implanted α_{Zr} micro-pillars compressed at 250°C.....	125
Figure 6.7: True stress versus true strain response for AN-oriented Zr^{+} implanted α_{Zr} / β_{Nb} micro-pillars compressed at 250°C.....	126

- Figure 6.8: post-deformation SEM images of (a) non-implanted and (b) Zr^{+} -implanted micro-pillars compressed at $250^{\circ}C$ 126
- Figure 6.9: $d\sigma/d\varepsilon$ with true strain (ε) during uniaxial compression of TN-oriented α micro-pillars in the non-implanted and the Zr^{+} implanted ($\psi \approx 6dpa @ 300oC$) condition. The data from the $25^{\circ}C$ test performed on a Zr^{+} implanted micro-pillar are obtained from σ - ε data presented in Reference [10] 120
- Figure 6.10: Measured average $\sigma_{0.2\%}$ from the various types of micro-pillars compressed at $250^{\circ}C$. The scatter bars represent the measured sample-to-sample variability in $\sigma_{0.2\%}$ as indicated by the data in Table 6.2 123
- Figure 6.11: Measured average $\sigma_{0.2\%}$ from the various types of micro-pillars compressed at $25^{\circ}C$. The data in this plot were previously reported [10][11] 124
- Figure 6.12: Variation of strain-hardening capacity $\Delta\sigma$ obtained from micro-pillar compression tests performed on non-implanted and Zr^{+} implanted α_{Zr} - and α_{Zr}/β_{Nb} micro-pillars at $25^{\circ}C$ (RT) $250^{\circ}C$. The data from the $25^{\circ}C$ tests were obtained from σ - ε data reported in [10][11] 125
- Figure 6.13 Calculated Schmid factor for deformation along 00101120 prismatic slip, 00010001 basal slip and $\{1102\} < 1011 >$ twinning systems (solid lines) as a function of basal misorientation angle with respect to the loading direction. Superimposed on the curves are the measured maximum Schmid Factors m for each of the α -micro-pillars of this study (Table 6.2) 126
- Figure 6.14: variation of τ with temperature for hcp α -phase Zr-2.5Nb subjected to 00010001 basal slip deformation [22][23][24]. Included in the plot are τ data from tests performed in this study and in our previous study [10] for α -phase samples subjected to 00010001 basal slip and 10101120 prismatic slip deformation 128

List of Abbreviations

α_{Zr}	α phase of Zr-2.5%Nb alloy
β_{Nb}	β phase of Zr-2.5%Nb alloy
c	Hexagonal lattice parameter normal to basal plane
CANDU	Canada Deuterium Uranium
CT	Calandria tube
DHC	Delayed hydride cracking
dpa	Displacement per atom
EBS	Electron backscatter diffraction
HCP	Hexagonal Close Packed
BCC	Body Centered Cubic
FCC	Face Centered Cubic
ISE	Indentation size effect
K-P	Kinchin and Pease
LAGB	Low angle grain boundary
HAGB	High angle grain boundary
M	Atomic weight
N	Number density
N_A	Avogadro's number
PT	Pressure tube
PWR	Pressurized water reactor
RMTL	Reactor material testing laboratory
SRIM	Stopping and Range of Ions in Matter
STEM	Scanning transmission electron microscopy
T	Temperature
TEM	Transmission electron microscope
UTS	Ultimate tensile strength
YS	Yield strength
Z	Atomic number
P	Material density
Φ	Irradiation fluence
$\omega\text{-Zr}$	ω phase of Zr
CRSS	Critical Resolved Shear Stress

TD	Transverse Direction
AD	Axial Direction
RD	Radial Direction

Chapter 1

1 Introduction

Nuclear reactors currently supply approximately 60% of Ontario's electrical energy output. This electrical output is supplied by 17 CANDU nuclear reactors located at three sites in the province. Many of these reactors are nearing the end of their thirty year design life and the safe continued operation of their internal structural components requires continuous attention and monitoring. Of particular concern are the Zr-2.5%Nb pressure tubes that carry the fissile uranium fuel bundles and transport the primary coolant through the core. The inside surfaces of these tubes sustain periodic scratching during service primarily, as a result of sliding motion of the fuel bundles. The growth of these flaws is continuously monitored however ultimately an assessment must be made about the fitness for service of a pressure tube based upon the severity of the scratches on its inside surface. To make such an assessment one must have very good understanding of the ductile fracture toughness of Zr-2.5%Nb pressure tube material when in a highly radiation hardened condition. Since this is a ductile fracture problem involving extensive localized plastic deformation in the small region, several micrometers in size, around a crack tip, this problem reduces to understanding the effect of neutron irradiation hardening on the mechanical stress-strain response of small α_{Zr} - and α_{Zr}/β_{Nb} - volumes of the Zr-2.5%Nb alloy.

This thesis presents the results of uniaxial compression tests performed on small, micrometer-size, pillars extracted from α_{Zr} - phase and α_{Zr}/β_{Nb} - phase regions of an extruded and cold-drawn Zr-2.5%Nb pressure tube. The micro-pillars were subjected to

Zr+ implantation to invoke significant crystal damage similar to that resulting from neutron irradiation. The objectives of this investigation were to understand:

- i) The effect of crystal orientation on the stress-strain response of the α_{Zr} phase in irradiation-hardened Zr-2.5%Nb pressure tubes.
- ii) The effect of constraint imposed by the presence of the β_{Nb} phase during the deformation of small volumes of $\alpha_{\text{Zr}}/\beta_{\text{Nb}}$ in irradiation-hardened Zr-2.5%Nb pressure tubes.
- iii) The effect of irradiation temperature and testing temperature on the mechanism of deformation of both the α_{Zr} phase and $\alpha_{\text{Zr}}/\beta_{\text{Nb}}$ – phase of irradiation-hardened Zr-2.5%Nb pressure tubes.

1.1 Structure of thesis

This thesis has been written in integrated-article format following the guidelines of the School of Graduate and Postdoctoral Studies at Western University. The thesis consists of seven chapters.

Chapter 2 provides a review of the fabrication process and microstructure of the Zr-2.5%Nb alloy and the operative deformation mechanisms of this alloy. Background information on the effect of high energy particle, ion or neutron, irradiation on the plastic deformation of this alloy is also presented.

Chapter 3 presents a brief description of the sample preparation and analysis techniques for all the experiments.

Chapter 4 presents the results of the investigation of the effect of Zr^+ implantation and crystal orientation on the uniaxial deformation of Zr-2.5%Nb α -phase micro-pillars. A version of this chapter was submitted for publication to the Canadian Metallurgical Quarterly[1].

Chapter 5 presents the results of the investigation of the effect of Zr^+ implantation on the uniaxial deformation of Zr-2.5%Nb two-phase α/β micro-pillars. A version of this chapter was submitted for publication to the Canadian Metallurgical Quarterly [2].

Chapter 6 presents the results of the investigation of the deformation of Zr^+ implanted Zr-2.5%Nb micro-pillars at 250°C. A version of this chapter is to be submitted for publication to the Journal of Nuclear Materials [3].

Finally, Chapter 7 provides the conclusions arrived at from this research project and presents directions for future work.

1.2 Novelties of this research:

Zr-2.5%Nb has been used in the CANDU reactors for a long time and its general “bulk” mechanical properties are quite well understood[4][5][6][7][8] however the mechanical properties of the specific α_{Zr} and β_{Nb} phase constituents of this alloy have not been thoroughly studied especially when it comes to their sensitivity to irradiation – induced hardening. In this project we have conducted combined novel laboratory techniques which include FIB micro-pillar fabrication, high-energy Zr^+ implantation, electron back scattered diffraction, and high-temperature micro-pillar compression testing to characterize, for the first time, the stress – strain response of α_{Zr} –phase and α_{Zr}/β_{Nb} –

phase regions of the Zr-2.5%Nb microstructure at temperature up to 250°C and at irradiation damage levels of 6 dpa.

References

- [1] M. I. Khan and R. J. Klassen, “Effect of Zr⁺ implantation and crystal orientation on the uniaxial deformation of Zr-2.5%Nb micro-pillars: Part 1, Deformation of single-phase α -Zr micro-pillars,” *Can. Metall. Q. Submitted*
- [2] M. I. Khan and R. J. Klassen, “Effect of Zr⁺ implantation and crystal orientation on the uniaxial deformation of Zr-2.5%Nb micro-pillars: Part 2, Deformation of two-phase alpha/beta micro-pillars,” *Can. Metall. Q. Submitted*
- [3] M. I. Khan and R. J. Klassen, “Deformation of Zr⁺ implanted Zr-2.5%Nb alloy at 250°C,” *J. Nucl. Mater.*, p. To be Submitted.
- [4] B. Bose and R. J. Klassen, “Temperature dependence of the anisotropic deformation of Zr–2.5%Nb pressure tube material during micro-indentation,” *J. Nucl. Mater.*, vol. 419, no. 1–3, pp. 235–240, Dec. 2011.
- [5] B. Bose and R. J. Klassen, “Effect of Zr⁺ ion irradiation on the mechanical anisotropy of Zr–2.5%Nb pressure tube material,” *J. Nucl. Mater.*, vol. 405, no. 2, pp. 138–143, Oct. 2010.
- [6] R. O. Oviasuyi and R. J. Klassen, “Anisotropic deformation of Zr ion irradiated Zr–2.5%Nb micro-pillars at 25°C,” *J. Nucl. Mater.*, vol. 421, no. 1–3, pp. 54–57, Feb. 2012.

- [7] R. O. Oviasuyi and R. J. Klassen, "Assessment of the anisotropic flow stress and plastic strain of Zr-2.5%Nb pressure tubes at temperature from 25°C to 300°C," *J. Nucl. Mater.*, vol. 429, no. 1-3, pp. 7-12, Oct. 2012.
- [8] A. Akhtar and A. Teghtsoonian, "Plastic Deformation of Zirconium Single Crystals," *Acta Metall.*, vol. 19, pp. 88-94, 1971.

Chapter 2

2 Literature Review

The objective of this thesis is to assess the micro-mechanical deformation mechanism controlling the length-scale deformation of the Zr-2.5%Nb CANDU pressure tube material in the non-implanted and the Zr⁺ implanted conditions with the view to understand the effects of implantation-induced crystal defects on the ductility of small volumes of the α - and α/β -phase constituents of the alloy. This chapter presents a review of previously published literature that provides important background information related to: 1) the effects of irradiation on the length scale-dependent plastic deformation of metals, 2) methods for assessing this plastic deformation, and 3) role of length scale-dependent plastic deformation on the fracture of Zr-2.5Nb pressure tube material.

2.1 The operation of a CANDU reactor

The CANDU (CANada Deuterium Uranium) nuclear reactor is an iconic pressurized heavy water moderated nuclear reactor (Figure 2.1). In a CANDU reactor, deuterium (heavy water) is used as a neutron moderator and non-enriched uranium is used as the fission fuel. There are several hundred fuel channels inside a typical CANDU reactor, similar to the one shown in Figure 2.2. These fuel channels are contained inside the horizontal cylindrical Calandria vessel. There is a pressure tube inside each fuel channel. These pressure tubes have wall thickness of 4 mm and an inside diameter of 103 mm. The pressure tubes are made of extruded and cold-drawn Zr-2.5%Nb alloy and contain the fuel bundles and the heavy water (D₂O) moderator/coolant. The pressure tube is considered to be one of the most critical components in a CANDU reactor because of the severity of the operational conditions. The internal operating pressure within this tube is

about 10 MPa and the temperature of the coolant passing through the tube ranges from 250°C to 310°C. During the expected 30 year lifetime of these tubes they experience a total neutron exposure (fluence) of approximately 3×10^{26} neutrons/m² [1][2][3].

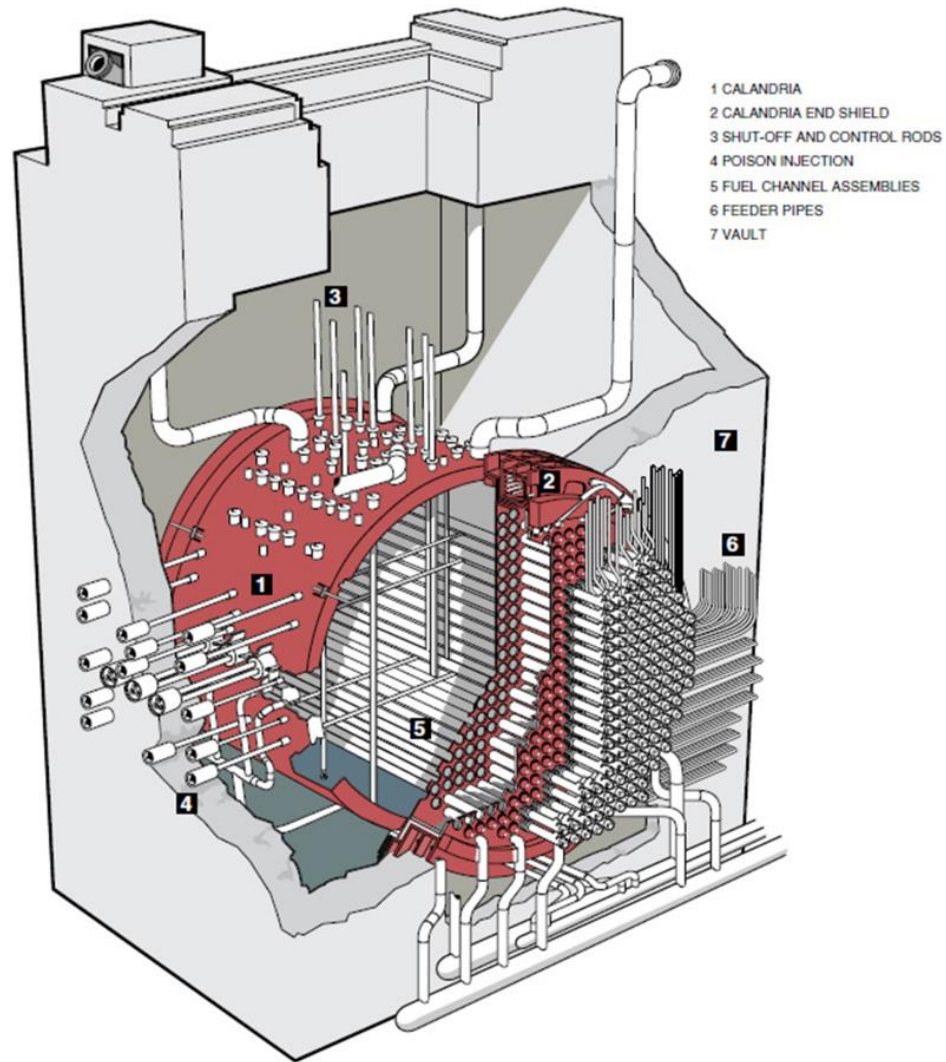


Figure 2.1: Schematic of a CANDU reactor core [4]

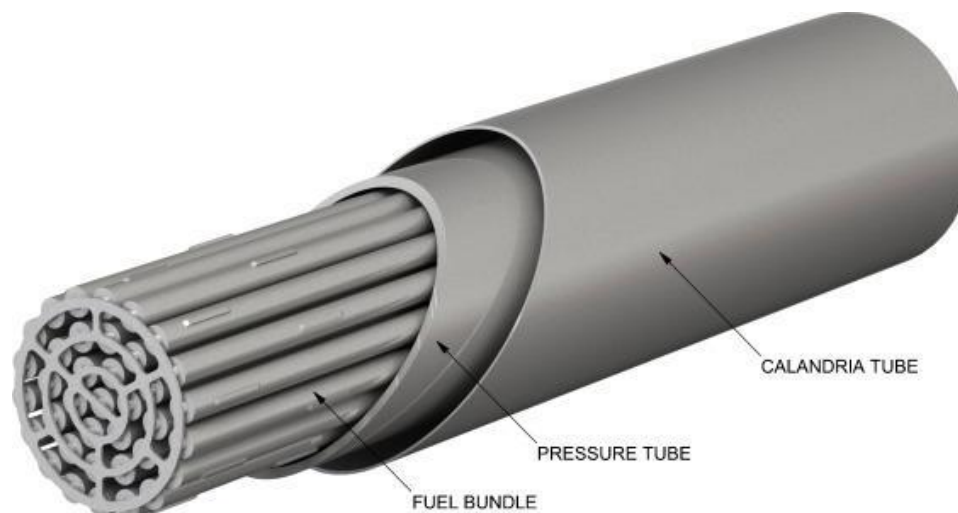


Figure 2.2: Schematic of a CANDU fuel channel [5]

The microstructure and the crystallographic texture of the Zr-2.5%Nb pressure tubes are formed as result of their extrusion and cold-drawing fabrication process. The extrusion is performed at around 850°C followed by cold-drawing to about 25-27%. The extrusion temperature corresponds to just within the β_{Zr} phase region of the Zr-Nb phase diagram (Figure 2.3). At that temperature the microstructure comprises of around 20% α -Zr(proeutectoid α) and 80% β -Zr phase (Figure 2.4). It can be seen from the phase diagram that the $\alpha+\beta$ phase field stretches from approximately 610°C to 862°C. The α -Zr phase at equilibrium (below 600°C) contains approximately 0.6wt% Nb in solid solution. Rest of the niobium (1.9wt%) is present in the bcc β -Zr phase.

Figure 2.5 shows the schematic of different directions of a section of a pressure tube. The extrusion process results in a tube with highly elongated β_{Zr} which transform during cooling to elongated pro-eutectoid α_{Zr} grains surrounded by a α_{Zr}/β_{Nb} eutectoid lamella (Figure 2.6). The hcp α_{Zr} grains are highly elongated in the axial direction (Figure 2.7) of the tube with an average grain size of about 0.2, 1.0 and 5.0 μm in the radial, hoop and

axial directions of the pressure tube respectively. The α_{Zr}/β_{Nb} eutectoid lamella is approximately 20-500 nm thick around the elongated α_{Zr} grains.

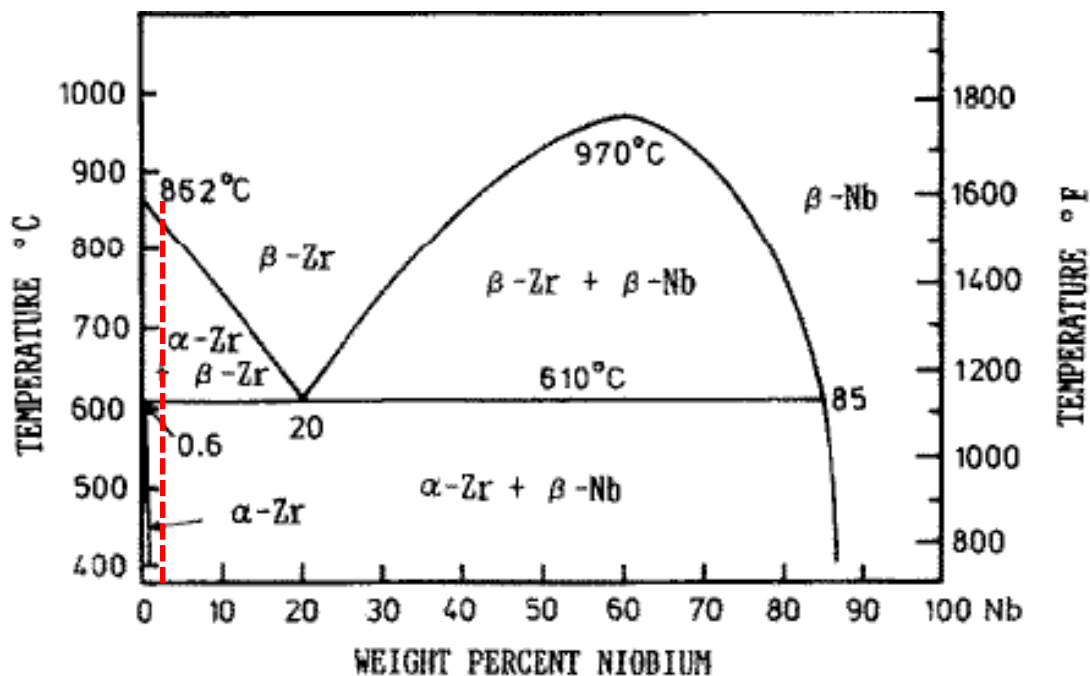


Figure 2.3: Zr-Nb binary phase diagram [6]. The vertical red line represents the position of the Zr-2.5%Nb pressure tube alloy

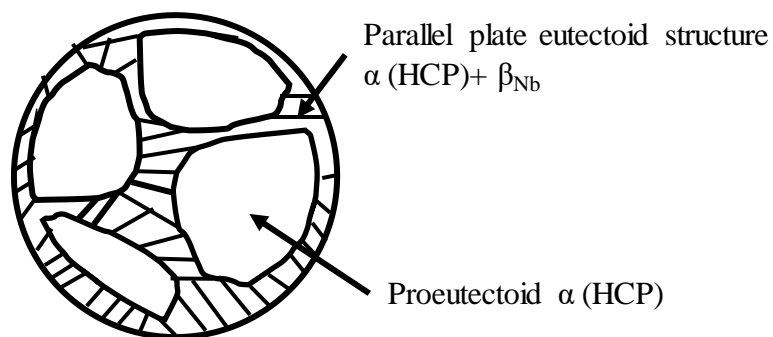


Figure 2.4: Schematic of Zr-2.5%Nb alloy microstructure

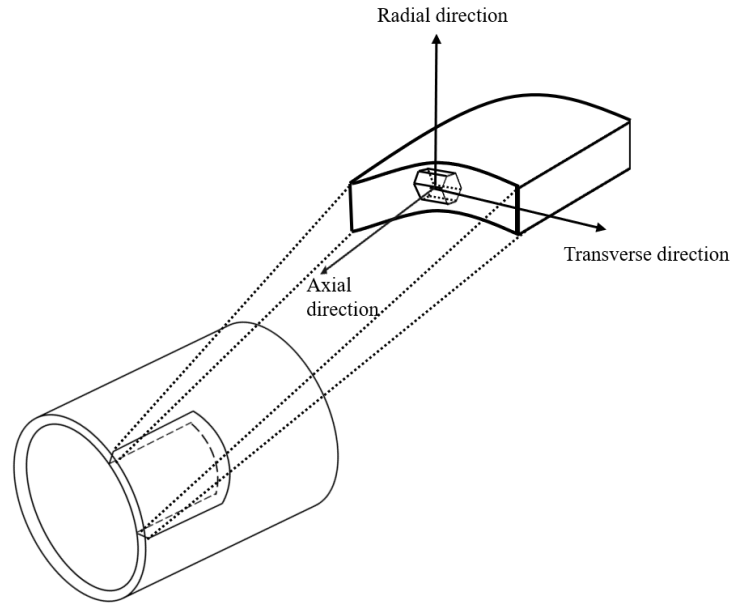


Figure 2.5: Schematic of Zr-2.5%Nb pressure tube section showing different directions of the pressure tube.

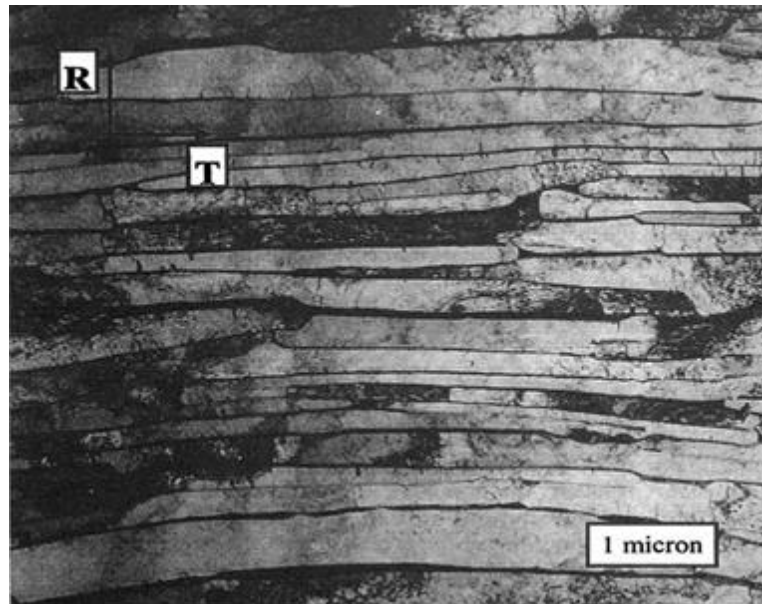


Figure 2.6: Typical grain structure of Zr-2.5%Nb pressure in CAUDU reactors. The light-colored α_{Zr} grains are surrounded by thin layer of dark-colored α_{Zr}/β_{Nb} eutectoid lamella [7]

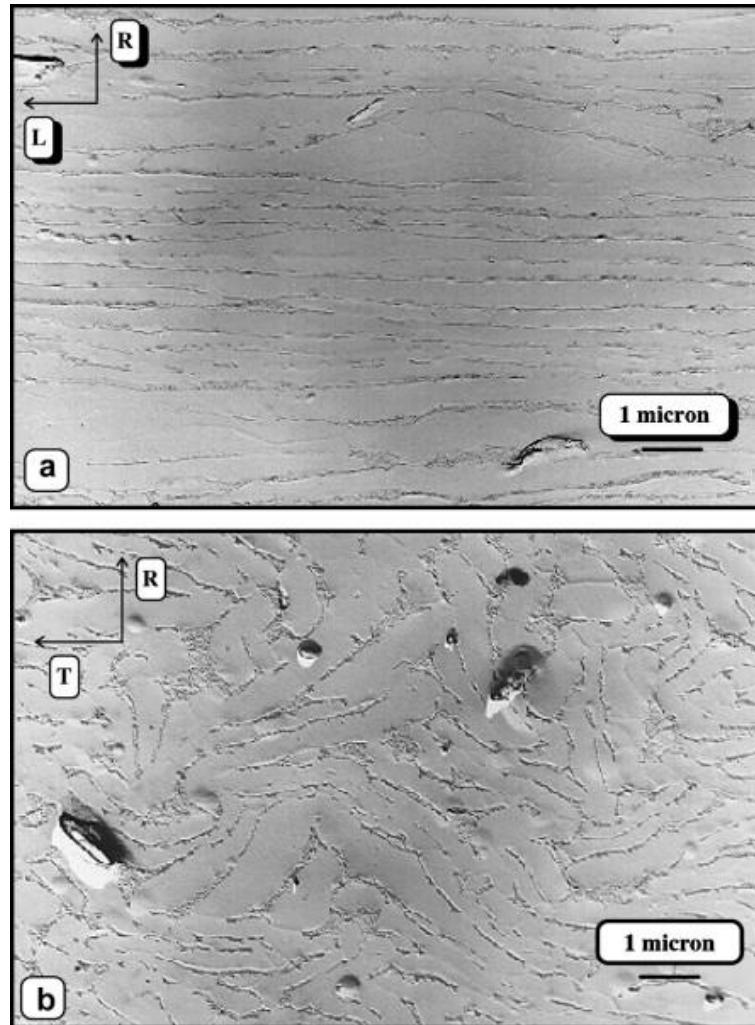


Figure 2.7: Transmission electron micrographs from carbon replicas of a pressure tube showing: (a) elongated α -grains in the axial/radial section and (b) curved flattened α -grains in the radial/transverse section[8]

2.2 Anisotropic deformation of Zr-2.5%Nb pressure tubes:

Extruded and cold-drawn Zr-2.5%Nb pressure tubes have a tensile yield strength of about 850 MPa when loaded in the circumferential (transverse) direction of the tube but only about 625 MPa when loaded along the axial direction [9]. This mechanical anisotropy arises from: 1) the mechanically anisotropic nature of the hcp pro-eutectoid α_{Zr} grains and

2) the strong crystallographic texture of the α_{Zr} grains developed during the fabrication process.

The fabrication process results in the (0001) basal plane normal vector for the majority of the α_{Zr} grains being aligned along, or near to, the circumferential (Transverse) direction of the tube (**Figure 2.8**).

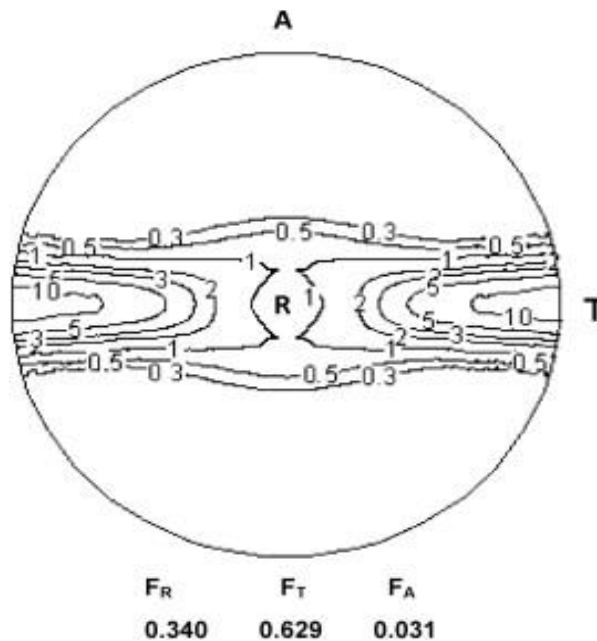


Figure 2.8: (0001) basal pole figure of an extruded and cold drawn Zr-2.5%Nb CANDU pressure tube [10]

The basic dislocation slip and twinning systems operative in hcp metals are shown in **Figure 2.9**. [13]. The potential operative dislocation slip systems comprise of the basal $\{0002\} \langle 1120 \rangle$ slip systems, prismatic $\{10\bar{1}0\} \langle 1120 \rangle$ slip systems, and $\{10\bar{1}2\} \langle 1123 \rangle$ pyramidal slip systems. In addition, plastic deformation by mechanical twinning is also commonly observed in hcp metals [11]. The critical resolved shear stress for

dislocation slip and twinning along the abovementioned systems in α_{Zr} are given in **Table 2.1**.

Table 2.1: CRSS for basal, prismatic, pyramidal slip and twinning of α_{Zr} at room temperature for pure Zr

Slip system	CRSS (MPa)
Basal	322 [11]
Prismatic	182 [12]
Pyramidal	501 [12]
Twinning	200 [13]

Generally for HCP metals, plastic flow takes place along directions parallel to the basal plane by slip on the basal or prismatic plane. Although slip is the common deformation mode in zirconium, during tension or compression along the c-axis, basal and prismatic slip cannot accommodate the deformation. Pyramidal slips are not easily initiated due to their temperature dependence and high critical resolved shear stress. Hence, to complete global plasticity, twinning deformation processes needs to be activated. The most common twinning mode for zirconium is $\{10\bar{1}2\}$.

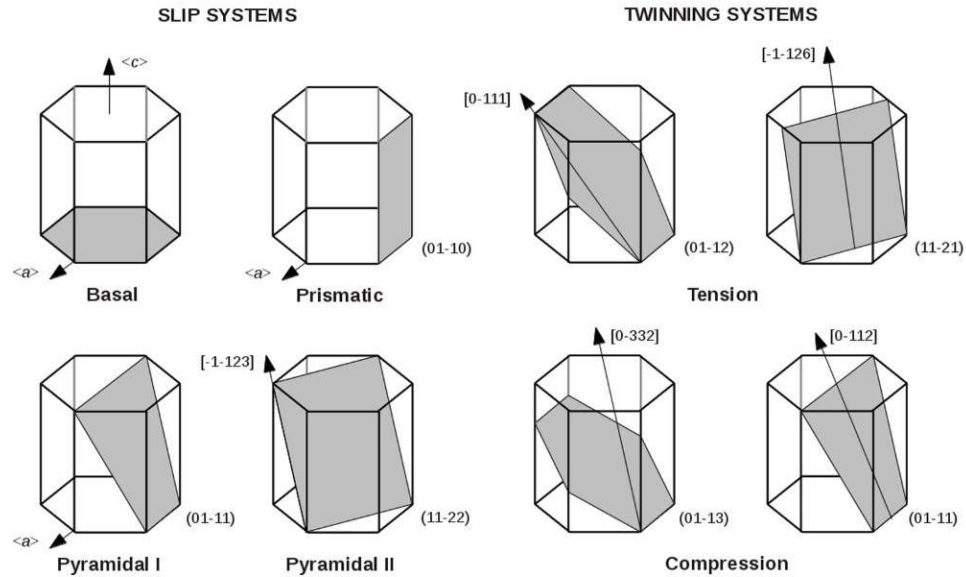


Figure 2.9: Possible dislocation slip systems and twinning systems in hcp crystals

[14]

2.3 Size effects on the strength and ductility of metals

Micrometer sized scratches are created on Zr-2.5%Nb pressure tubes surface due primarily to repeated sliding to the movement of fuel bundles. These scratches could become stress concentrations from which ductile fracture of the pressure tubes initiates. Hence, it is important to understand the ductile fracture process of Zr-2.5Nb pressure tubes in order to carry out accurate fitness for service assessments of in-reactor pressure tubes containing surface flaws. It is known that these pressure tubes fracture by stable crack growth by a process of fracture of brittle phases (such as hydrides), thus leaving small α and α/β filaments to support the load ahead of the crack tip. These filaments can be as small as $1\mu\text{m}$ so their mechanical strength may be affected by length scale plasticity effects. A few examples of small ligament testing will be provided and after that theories needed to explain the deformation mechanism with size effect will be briefly discussed.

Zr-2.5%Nb alloy has microstructural similarity with dual phase titanium alloys. Both of them contain hcp- α phase and thin ligaments of β phase. Although a number of experiments have been carried out to determine the strength of the constituting phases at small length scale for titanium alloys [15][16][17][18][19][20][21], in comparison to that the number of experiments conducted on small zirconium samples is few [22] [23] [24].

Weekes et al. [22] examined the deformation mechanism of hydrided Zircaloy-4 using hydrided micropillars in the scanning electron microscope. They reported that the matrix and hydride can co-deform depending on the orientation of the hydrides in the sample. The yield strength is much higher for the hydrided samples compared to as-received ones. They also reported that size effect was observed for all the samples.

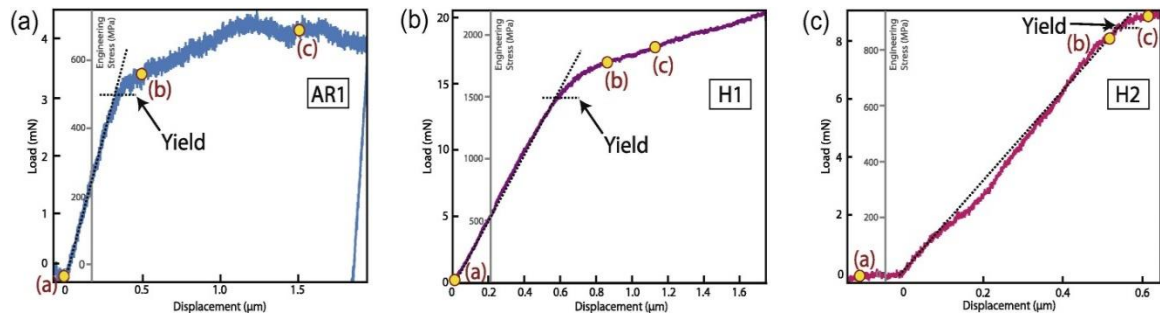


Figure 2.10: Load–displacement curves (with inferred secondary stress axis) obtained from in situ SEM compressive loading of both as-received (AR1) and hydride-containing (H1, H2) micropillars [22]

Wang et al. [23] conducted micro-cantilever bending test on hydrided and hydride free single crystal samples prepared from Zircaloy-4. They observed that the presence of hydride changes the deformation mechanism significantly. For the hydride free cantilever the applied stress was accommodated by plastic slip, whereas the hydride containing cantilever displayed precipitation-induced Geometrically Necessary Dislocation (GND)

pile-up at hydride matrix interface before deformation. They reported that at the time of plastic deformation, due to the high applied tensile stress, GND density increased substantially.

Chan et al. [24] studied the fracture properties of zirconium hydrides and phase boundaries using micro-cantilever testing method. A typical load-displacement curve is shown in **Figure 2.11**. The figure shows that the hydrided cantilever has a brittle fracture whereas the cantilevers prepared from α -Zr and interface, shows ductile fracture. They also observed that the brittle hydride phase shows a fracture toughness of $K_{IC} = 3.3 \pm 0.4 \text{ MPam}^{1/2}$, which is much higher compared to the values obtained from bulk Zr hydride samples having a fracture toughness of $1 \text{ MPam}^{1/2}$. They reported that this higher toughness might be due to the fact that δ -hydride on its own at small scale is not entirely brittle. They also reported that the yield strength of a hydride at this length scale is about 1200 MPa whereas for a typical hydrided zirconium alloy this value is in the range of 600-800 MPa. For α -Zr alloy studied in this experiment, the yield strength was 570-680 MPa, in comparison to that the value reported for bulk α -Zr samples are much lower 205-540 MPa.

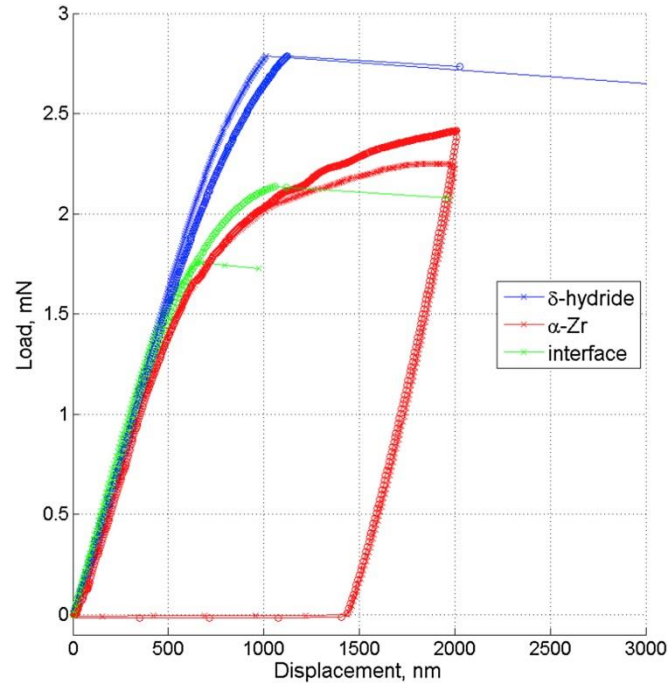


Figure 2.11: Typical load-displacement curves of micro-scale pre-cracked cantilevers tested at room temperature [24]

To summarize, when tested in micron or sub-micron length scale, individual phase constituents show different mechanical properties compared to the bulk mechanical properties. Typically smaller samples are stronger. Several theories have been proposed to explain the size effect of the yield stress of materials. These include dislocation starvation, source truncation hardening, and dislocation source-limited behavior.

Dislocation starvation was proposed by Greer et al. [25]. According to this theory, mobile dislocations are attracted to the surface by image forces, but in a micron length pillar the surface area to volume ratio are very high, as a result the mobile dislocations can leave the crystal before dislocation multiplication or nucleation can take place. This causes dislocation starvation. As an aftermath of this starvation, more stress is needed to activate or nucleate other dislocations so that plasticity can be continued.

Another proposed theory to explain size effect is “exhaustion hardening”. In general, the number of dislocation sources available in a bulk sample should be far greater compared to micron sized samples. The scarcity of dislocation sources in micron sized samples is responsible for exhaustion hardening. As there are limited numbers of dislocation sources available, hence it takes more stress to activate or nucleate dislocation sources compared to large samples.

Source truncation hardening is another mechanism proposed to explain the size effect. According to this theory, dislocation sources are present in the sample in the form of double-pinned Frank-Read sources and this source has to be bowed for dislocation multiplication. The stress required to bow a Frank-Read source is given by,

$$\tau = \frac{\mu b}{L}$$

Here, μ is the shear modulus, b is the magnitude of the Burger’s vector and L is the length of the distance between two obstacles. As a Frank-Read source leaves the free surface of a micro pillar the bow shape breaks into two smaller parts or truncated dislocations, which results in shorter length for L . This short length of L is mainly due to decrease in pillar diameter, which increases the required stress to continue plasticity.

2.4 Micro-mechanical testing

Micro-mechanical testing became extremely popular after the publication of the journal paper titled ‘Sample dimensions influence strength and crystal plasticity’ by Uchic et al.[26]. Although it was shown almost 50 years ago by Brenner [27][28][29] that single crystal metallic whiskers having micrometer diameters exhibit large increase in yield

strength, the changes in mechanical response of material due to changes in physical geometry of a sample had been overlooked for decades.

Uchic et al. [26][30] developed an unique test methodology which allowed the scientists to examine size-scale effects in almost any inorganic material. Using focused ion beam milling; cylindrical samples were fabricated from bulk crystals and then compressed with conventional nano-indentation device equipped with a flat punch indenter.

Over the past few years, various micromechanical testing methods have been developed to observe the mechanical response of materials at micron and nano length scale. The micromechanical testing method is not only limited to compression testing, materials with various geometries are also being tested in bending and tension. These experiments allow the researchers to address the fundamental issues in crystal plasticity and to integrate the material properties at micron scale in the simulations models.

Micro-pillar compression experiments have been conducted on a variety of materials. Three very informative review papers discuss in detail regarding the plasticity at micro and nano level and the micromechanical experiments associated with them [31][32][33]. These micromechanical experiments allow the researchers to study the size dependent and site-specific properties of different materials. Size dependent experiments usually deal with extrinsic and intrinsic size effect of the materials. Whereas, site specific experiments are becoming popular as they deal with local properties of materials (grain boundary, crystal orientation, different phases).

Experimental studies have been conducted to study the micromechanical properties and deformation mechanism of face-centered cubic (fcc) [34][35][36], body-centered cubic

(bcc) [37][38], metallic glass [39], intermetallic compound[40] and amorphous metals. The more recent trend is in situ micromechanical experimentation of materials using SEM equipped with EBSD [41] and TEM.

The most commonly observed phenomenon during micro-compression testing is the very strong size effects on the yield stress which initiated the slogan “smaller is stronger”. Another very interesting phenomenon is the shape of the stress-strain curves obtained during compressions. These curves show strain bursts and have a step-like structure. The higher strength of the material at small scale has been attributed to the defect free nature of smaller crystals. As the smaller crystals have very small surface area they suffer from dislocation starvation [42][42][43] which means dislocation move out of the free surface very rapidly hence the sample has fewer dislocations. Another possible explanation is these small samples have a limited number of dislocation sources which is the cause of their high yield strength.

A lot of micro-mechanical testing has been done on FCC and BCC metals but in comparison the amount of work done related to HCP material is less. As our research objective is to obtain information regarding plasticity of Zr based alloy at the micron length scale in this report we would particularly focus on different aspects of micro-mechanical testing of HCP (titanium, magnesium, zirconium, cadmium, zinc) metals such as- different sample geometry, different testing techniques and the effects of irradiation.

Shin et al. [43] performed micropillar compression experiments on circular and square pillars and compared the effect of pillar geometry on the evaluated stresses. They observed that the stresses are size independent for both circular and square pillars. The

interesting observation was that due to taper, in case of the circular pillars the average stress at the top surface was approximately 60% larger than the mid portion of the pillar. Whereas, for the square pillars the calculated stress was almost same in top, mid and bottom position due to the reduced taper.

Sun et al. [44] conducted uniaxial compression experiments on rectangular prismatic titanium micropillars loaded along $[11\bar{2}0]$. They reported that the flow stress increases significantly up to 1040 MPa with decreasing pillar size down to 300 nm. They also observed that the critical resolved shear stress is inversely proportional to the sample size which is consistent with dislocation source nucleation-controlled plasticity.

Byer et al. [45] conducted micropillar compression experiments on Mg single crystals. They fabricated single-crystal magnesium micropillars in the range of (2.5-10 μm) diameter using FIB and the pillars were compressed along $[0\ 0\ 0\ 1]$ c -axis. They did not observe any significant size effect on strength for these pillars. They reported that there were significant hardening due to multiple active slip systems on the pyramidal planes and they did not observe any deformation twinning.

Byer and Ramesh [46] also studied the effects of the initial dislocation density on size effects in single-crystal magnesium. The FIB fabricated pillars were 600 nm to 10 μm in diameter. The pillars were compressed along two different directions $[0\ 0\ 0\ 1]$ and $[2\bar{3}1\ 4]$. They observed that decreasing the initial dislocation density resulted in stronger size effect. Based on their experimental investigation they concluded that the mechanical properties of magnesium micropillars depend on specimen diameter, the initial dislocation density and the orientation of the basal planes with respect to the loading axis.

Lilleodden [47] investigated the stress–strain response, slip mechanisms and size effect in Mg (0 0 0 1) single crystal by micro-compression testing. She observed that the yield stress increases with decreasing diameter by comparing the flow stress obtained for columns of 2.1 μm diameter with 6 μm diameter columns. She also reported that twinning is not the predominant deformation mechanism.

Prasad et al. [48] performed compression test on both micropillar and macro-pillar fabricated from magnesium single crystals. They noticed that the micropillars exhibit higher flow stress than bulk samples. They also observed that the obtained flow curves were smooth for bulk samples but the micropillar flow curves consisted intermittent and precipitous stress drops.

Sumin et al. [49][50] studied the mechanical properties of two HCP metals, zinc and cadmium. They performed uniaxial micro-compression test for both the metals and observed different trend. They reported that for cadmium micropillars, pillars with diameters near 0.5 and 1.1 μm are slightly stronger than bulk but with the reduction of pillar diameter to near 0.1 μm the mechanical strengths exceed 1 GPa. Whereas, that zinc micropillars at micro scale are insensitive to both strain rate and size.

2.5 Effect of particle irradiation on the mechanical response of Zirconium alloys:

Impacting a crystalline metal with high energy, atomic- and subatomic-size, particles, such as ions or neutrons, causes the generation of crystal defects, such as point defects and small dislocation loops, in the metal. These crystal defects result in the metal becoming hardened and more brittle. The extent of irradiation damage imparted to the

crystal is usually expressed in units of displacements pre atom (dpa). **Figure 2.12** depicts the yield strength of Zr-2.5Nb pressure tube material as a function of dpa induced by direct exposure to neutron flux during service in a CANDU reactor core. As can be seen from this image, the yield strength rapidly increases at comparatively lower fluence. After that the strength seems to stabilize and does not increase with the increase in fluence due to saturation of irradiation induced hardening.

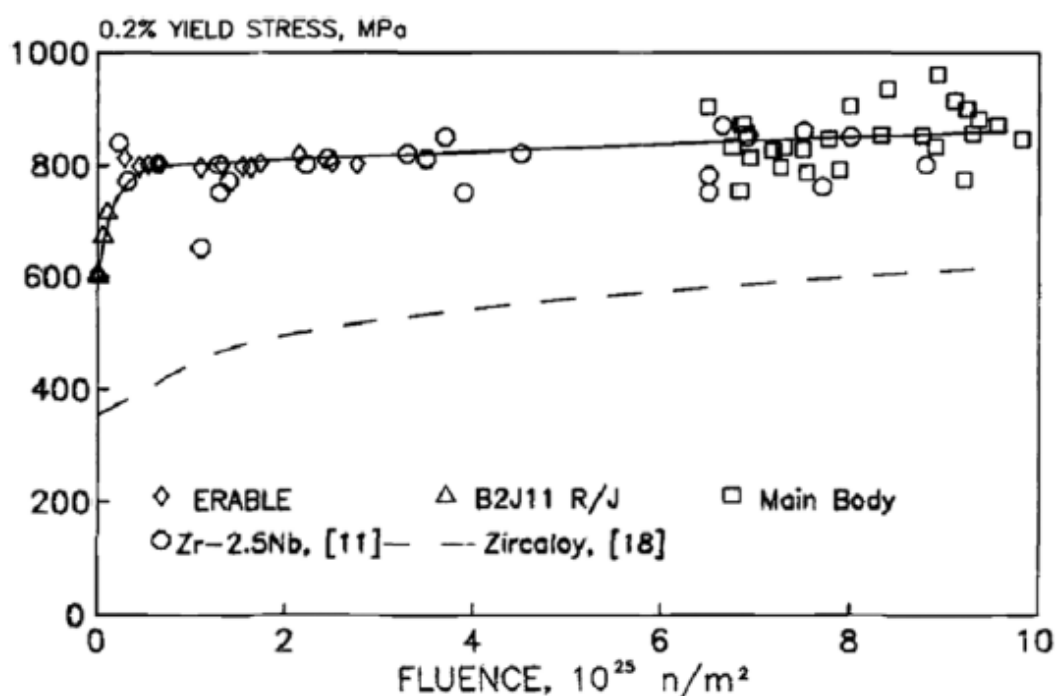


Figure 2.12: Dependence of yield stress on fluence [51]

It is difficult to work directly with radioactive materials, due to the required radiation shielding; hence, ion-implantation is widely used as a feasible alternative to simulate neutron damage without inducing radioactivity in the samples. Depending on ion species and the energy used the amount of damage due to ion-implantation can be controlled according to the research need. Landau et al. [52] conducted compression experiments on

helium implanted and non-implanted single crystalline Fe samples and observed that implanted material has higher load bearing ability (**Figure 2.13**).

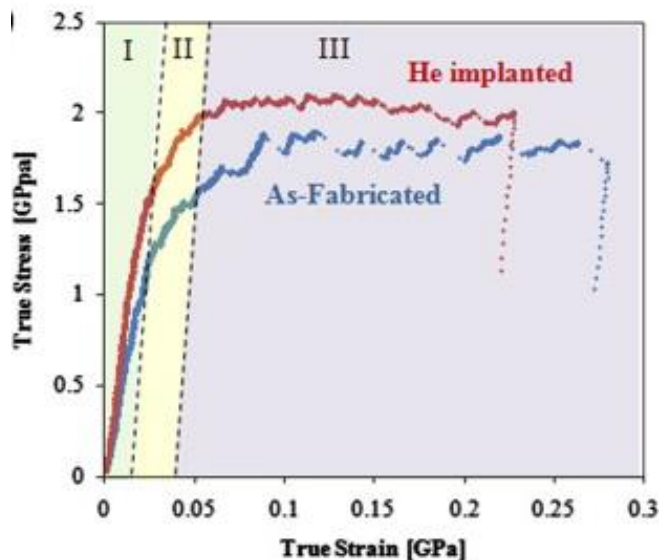


Figure 2.13: Comparison of ion implanted and un-implanted sample [52]

There have been some recent micro-mechanical experiments on ion implanted materials [53][54][55] and a review has been published emphasizing microstructure and property changes of zirconium alloy due to ion irradiation [56].

2.6 Effect of grain boundaries

To understand the ductile fracture of Zr-2.5%Nb pressure tube material at the micron-length scale it is important to understand how small α - and α/β -filaments deform at different temperatures and different implantation conditions. To offer a general idea about the difference in deformation mechanism between single crystal and bicrystal samples, a brief review is provided here. Using the focused ion beam technology, it is possible to fabricate micron or nano-sized specimens containing a single grain boundary.

In addition, applying the EBSD technique, the orientation of the individual grains present in a bicrystal can be known.

Comparison of the mechanical properties between a single crystal and bicrystal micropillar of similar dimension provides insight into the effect of the grain boundary. The mechanical yield strength of a bicrystal pillar varies depending on many things, such as the Schmid factor of the participating grains, ease of slip transferability between the two grains, and volume of the pillar occupied by each grain.

As reported in the literature [57][58][59][60][61] that the type of grain boundary will strongly affect the strength of the bicrystal pillars. It has been demonstrated that greater applied stress is necessary to force dislocation motion across a highly misoriented (i.e. high angle) grain boundary compared to a low angle grain boundary or coherent twin boundary. Therefore, based upon this logic, we expect that local angular misorientation across grain boundary and interfaces in Zr-2.5%Nb pressure tubes will affect the mechanical properties of the pressure tube material.

Cai et al. [62] reported that the β -Zr phase shows higher compressive and tensile strength than α -Zr. Hence it can be assumed that the deformation in a α/β bicrystal pillar would be activated in the α -Zr part. Ashton et al. [20] reported that for dual phase titanium alloys the orientation of beta phase relative to the alpha phase plays important role in the micromechanical response of the alloy. The flow stress would be higher if the β phase acts as barrier to mobile dislocations. As Zr-2.5%Nb has microstructural similarity with the dual phase titanium alloy, the β -Zr could also have similar impact in micromechanical response. Comparing with the literature, the higher strength of bicrystal

pillars compared to single crystal pillars could be attributed to the presence of high angle grain boundary and relatively lower strength could be attributed to low angle grain boundary.

2.7 Effect of particle irradiation on the microstructure of Zr alloys

Several researchers have worked on effect of particle irradiation on the microstructure of Zr alloys [63][64][65][66][67][68][69]. Various types of defects can form in Zr alloys as a result of particle irradiation. There could be formation of point defects (vacancies and interstitials), planar defects (dislocation loops), or volumetric defects (voids, bubbles, cavities).

If the point defects form in vacant lattice sites, they are called vacancies and an equal number of interstitials will form due to displaced atoms lying on interstices. The combination of vacancy and interstitials is known as Frenkel pairs. These point defects agglomerate to form line, planar, and volumetric defects.

Three type of dislocation loops are generally formed in Zr crystals due to irradiation, $\langle a \rangle$, $\langle c \rangle$, and $\langle a+c \rangle$. Among them $\langle a \rangle$ type loops are the most common ones. They form at low damage levels and have a Burgers vector of $\frac{1}{3} \langle 11\bar{2}0 \rangle$ and a prismatic habit plane $\{10\bar{1}0\}$. They have been reported by many researchers[65][66]. The growth and nucleation of $\langle a \rangle$ type loops are affected by temperature, impurities, stress, and pre-existing microstructural features. It has been reported that the morphology of these loops could change due to increase in temperature. Jostsons et al.[70] reported that with the increase of temperature loop diameters of $\langle a \rangle$ type loop increases whereas the loop

density decreases. Alloying elements also plays important role in nucleation, stability and growth of $\langle a \rangle$ -loops. It has been reported that addition of Sn and Nb, result in increase in loop size and decrease in the number density of these loops [70].

$\langle c \rangle$ component loops form in irradiated Zr alloys at higher doses compared to $\langle a \rangle$ type loops. They have a Burgers vector of $\frac{1}{6} \langle 20\bar{2}3 \rangle$ and align parallel to the basal plane. It has been reported that fluence higher than $5 \times 10^{25} \text{ nm}^{-2}$ in the temperature range of 287-500°C [68] is needed for the formation of $\langle c \rangle$ loops. $\langle c \rangle$ type loops are larger in size compared to $\langle a \rangle$ type loops. Tournadre et al. [71] reported that $\langle c \rangle$ component loops formed in Zircaloy-4 at 350°C as a result of 2 MeV proton irradiation to a damage level of 11.5 dpa. They also reported that $\langle c \rangle$ component loops did not nucleate in Zircaloy-4 when the irradiation temperature was 300°C and the damage was 2.9 dpa.

Zr alloys go through secondary phase evolution and microchemical changes due to irradiation. These changes will have significant impact on the microstructure which will eventually impact the properties and corrosion resistance of the alloy. The dual phase microstructure of Zr-2.5%Nb alloys is not stable under irradiation. As a result, needle like Nb-rich precipitates could nucleate in the α_{Zr} phase from the secondary β phases as they are supersaturated in Nb. Along with Nb precipitation in α_{Zr} phase, β phases could also be decomposed due to irradiation as chemical changes take place in Nb- rich phases due to irradiation. It has also been reported that the ω -phase could also transform into β_{Nb} after irradiation[67].

2.8 Mechanical testing of Zr alloys at different length scales

The deformation and mechanical behavior of alpha-zirconium single crystal is dependent upon crystal orientation. Crystals tested parallel to the c axis $\langle 0001 \rangle$ is harder compared to crystals tested perpendicular to this direction.

Akhtar et al. [72] and Akhtar [73][74] performed tensile and compression tests on samples prepared from zirconium single crystals. Akhtar et al. [72] used the angle X_B between the tensile axis and basal plane as a parameter to describe the deformation behavior. For tensile samples tested at 78 K, they observed that if $X_B < 35^\circ$ then the onset of plastic flow takes place by first order prismatic slip. However, in case of X_B being greater than 35° , the crystal deformation is initiated by twinning which is followed by prismatic slip. With the increase of test temperature to 295 K twinning initiated when X_B was greater than 45° . Another important observation is that the stress-strain curves generated via tensile testing for zirconium has similarity with those of the FCC crystals in terms of work hardening. The work hardening of zirconium single crystals depends on test temperature. Stage I hardening is absent if the test temperature is greater or equal of room temperature, whereas stage II hardening is visible in this range. Samples tested above 423 K consist entirely of stage III hardening.

In another study, Akhtar [73] compressed single crystals of zirconium along the c-axis for a temperature range in between 78 K and 1100 K. He observed that plastic deformation takes place by $\{11\bar{2}2\}$ twinning up to a temperature of 800K, above 800K plastic deformation is initiated by a combination of $\{10\bar{1}1\}$ twin and (c+a) slip. He concluded that the increase of flow stress with temperature and high work hardening rate below

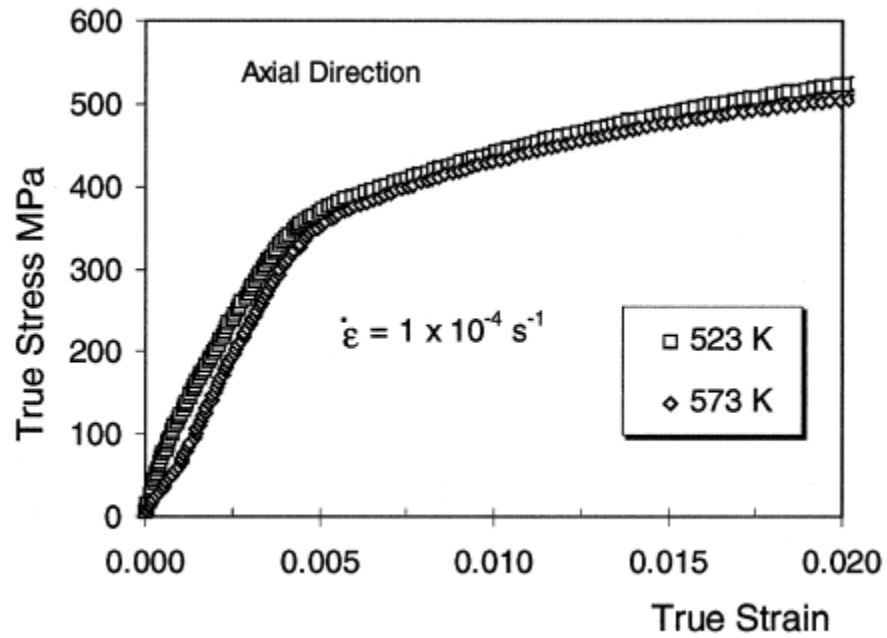
800K is related to $\{11\bar{2}2\}$ twinning, whereas the decrease in yield stress and low work hardening rate above 800 K is associated with $\{10\bar{1}1\}$ slip and twinning.

Akhtar [74] performed tensile tests on single crystals of Zr prepared in prismatic slip favoring orientation at different temperatures between 473 K and 1113 K. In this temperature range only prismatic slip lines were observed by him. He also observed that with the increase in temperature the spacing between primary slip lines increases and the slip lines gets finer and wavy. The CRSS decreased with increasing temperature up to around 600K, in the range of 600 to 800K there was not much change in CRSS values but a quick decrease was observed after that.

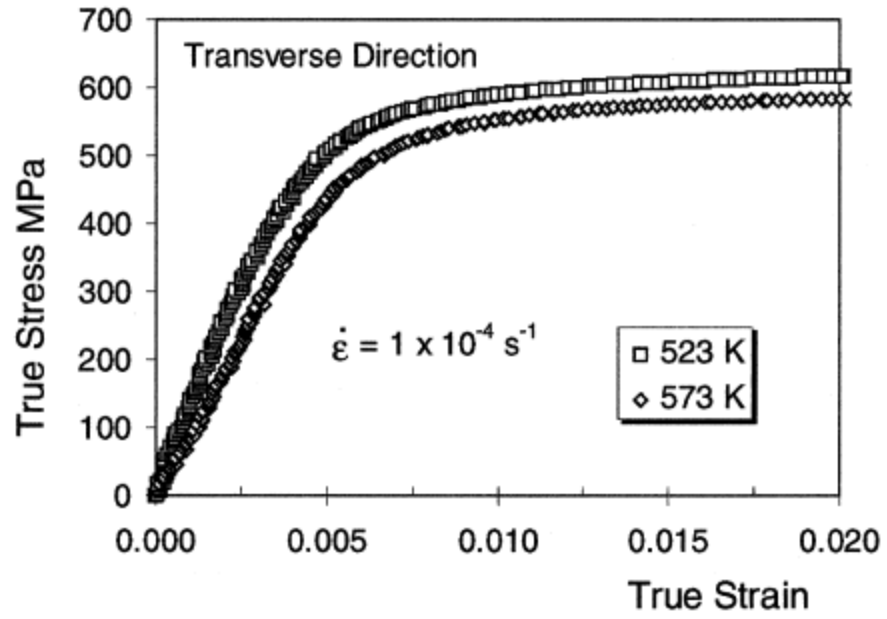
Christodoulou et al. [75] conducted tensile test on non-irradiated Zr-2.5%Nb samples at different temperatures using different strain rates to observe the temperature and strain rate dependence of the yield stress in axial, transverse, and radial directions of a pressure tube. They observed that the yield anisotropy remained constant up to 800 K and strain rate sensitivity was also constant up to 700 K. Yield strength was comparatively higher in transverse direction but strain hardening rate was lower compared to axial direction samples (**Figure 2.14**).

Himbeault et al. [1] studied the deformation behavior of irradiated Zr-2.5%Nb pressure tube material in the temperature range of 30°C to 300°C. They reported that strain localization was the reason behind local softening of the material at irradiated condition. As can be seen from **Figure 2.15**, in spite of the irradiation and increase in deformation temperature, samples tested in transverse direction display higher yield strength compared to axial direction samples. Irradiation hardening resulted in higher yield

strength regardless of the elevated deformation temperature if we compare between **Figure 2.14** and **Figure 2.15**.



(a)



(b)

Figure 2.14: (a) Tensile flow curves of pressure tube material tested in the axial direction (b) Tensile flow curves of pressure tube material tested in the transverse direction [75]

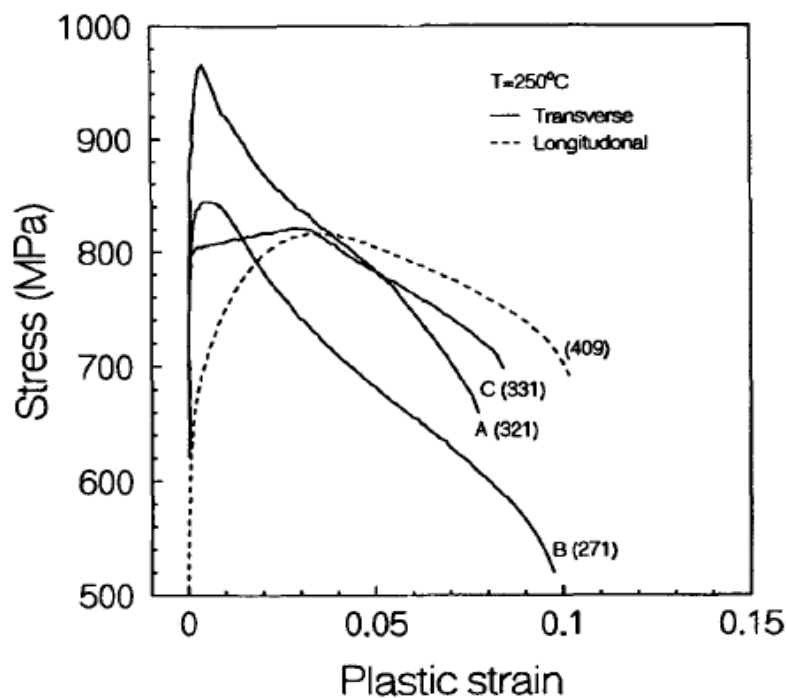


Figure 2.15: Typical flow curves for irradiated specimens for transverse and longitudinal directions at 250°C [1]

Long et al. [76] conducted in-situ neutron diffraction experiments at different temperatures on non-irradiated and neutron irradiated samples of Zr-2.5Nb pressure tubes during tensile testing. They observed that prismatic, basal and pyramidal slip was activated in both irradiated and non-irradiated samples. They applied line profile analysis to measure the change in dislocation density during the deformation process. They concluded that as a result of neutron irradiation, the prismatic and basal slip is hardened, whereas the pyramidal slip system is not that much affected by irradiation. Another important observation was that with the increase in test temperature the anisotropic ratio decreased but the initiation sequence of the three slip modes did not change.

Gong et al. [12] determined the slip strengths of basal, prism and pyramidal systems in commercially pure zirconium applying micro-cantilever testing. They observed 'size effect' as the critical resolved shear stress (CRSS) increased in all slip directions with decrease in cantilever size. For a 1 μ m cantilever, they found that the CRSS values for prismatic, basal and pyramidal slip systems are 507 MPa, 618 MPa, and 1050 MPa respectively.

A brief review is given in the following section regarding micropillar compression [77][22][78][79][65] of zirconium alloys.

Weekes et al. [22] studied the deformation of hydrides in Zircaloy-4 applying in situ micropillar compression technique. Comparing the deformation mechanism between as received and hydrided samples they observed that the hydrides harden the material. They reported that during the compression of the un-hydrided sample the macroscopic yield occurred at approximately 530 MPa, which is significantly higher than the strength of the bulk alloy which has a strength of 370-460 MPa. They concluded that the matrix and hydride can co-deform, and the hydrides acted as storage for deformation defects.

Oviasuyi and Klassen conducted compression tests on cylindrical samples [78] and micropillars [79] prepared from Zr-2.5%Nb pressure tubes. The cylindrical samples were 2 mm in diameter and 3 mm in height. These samples were prepared from axial (AD), transverse (TD) and radial (RD) direction of the pressure tube. Compression tests were conducted in a range of 25°C to 300°C. They reported that the yield stress was gradually declining in all directions with increasing temperature. The micropillars were 5 μ m in diameter and 5 μ m in height. Similar to the cylindrical samples, micropillars were also

fabricated from three different orientations of the pressure tubes. These samples were irradiated with 8.5 MeV Zr^+ and compressed at room temperature. The effect of irradiation was more prominent in the direction with low (0001) basal pole fraction, which indicates that irradiation hardens the prismatic dislocation slip more compared to pyramidal slip. They observed that the yield stress, strain hardening exponent, and degree of strain localization of the micro-pillars increased with ion irradiation (**Figure 2.16**). One of the key observations from this study was that the amount of mechanical anisotropy is significantly reduced when the alloy is in irradiation hardened state.

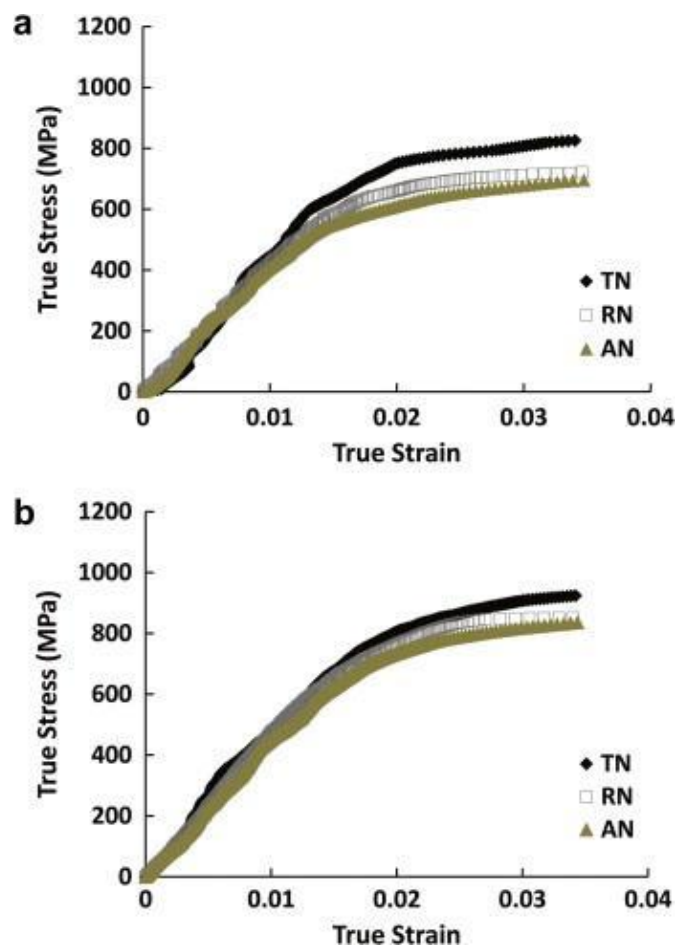


Figure 2.16: Typical true stress versus true strain curves obtained from uniaxial compression of 5 μm diameter Zr-2.5%Nb micro-pillars in: (a) the non-irradiated condition and (b) after Zr^+ ion irradiation[79]

Wang et al. [65] studied the deformation mechanism of heavy ion irradiated Zr-2.5Nb pressure tube material by micropillar compression at room temperature. The micropillars used in the experiment had top diameters in the range of 1.75 μm to 1.85 μm and the average size of alpha zirconium phase was approximately 200nm. Hence, there were around nine grains on average across the diameter of each pillar. They did not observe any size effect because of the presence of grain boundaries which acted as dislocation sinks. Using 40MeV Zr ion they could create 6.5 μm damage layer in the sample and a

damage of 0.6 dpa. They observed that irradiation increased the yield strength more in the pillars created in the axial direction of the pressure tube compared to pillars prepared in the transverse direction of the pipe (**Figure 2.17**).

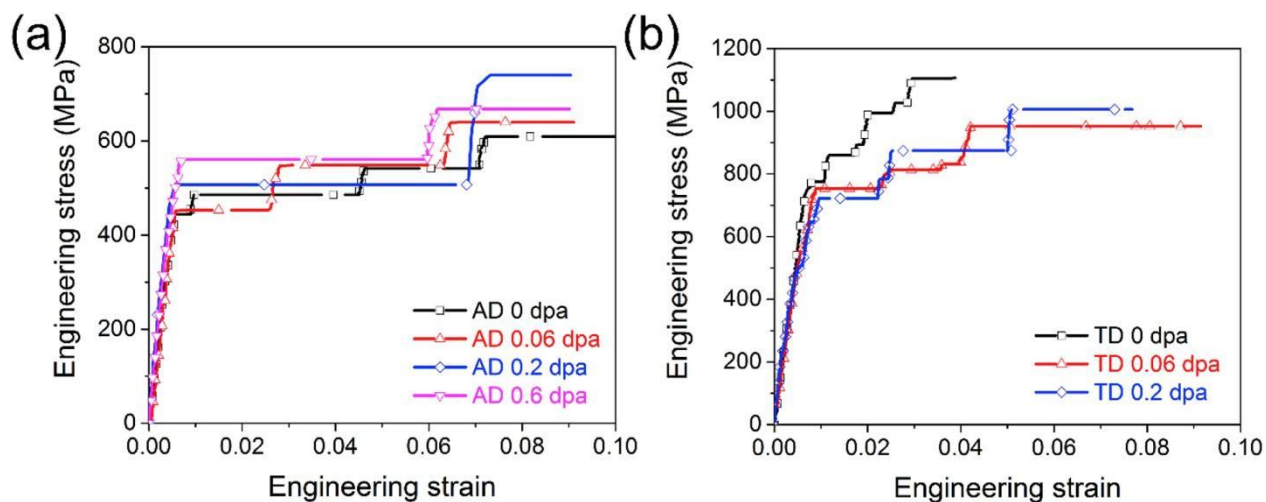


Figure 2.17: Engineering stress-strain curves of (a) AD and (b) TD samples [65]

It is clear from this literature review, to the best of our knowledge that there has not been any work which dealt with micromechanics of plasticity of Zr-2.5 Nb alloy phases at irradiated and non-irradiated condition at micron and sub-micron length scale.

2.9 Summary

The data presented in this chapter indicate that the ductile fracture behavior of bulk Zr-2.5Nb pressure tube material is in fact determined by the deformation of micro-meter size α -phase and α/β -phase filaments in the vicinity of the crack-tip. The operative plastic deformation mechanisms of within these filaments may well be quite different than for bulk samples. Typically sub-micron samples display significantly high yield stress, intermittent strain jumps, and operative deformation mechanism is confined within a specific activation volume. These observations are reported by a good number of

independent researchers, but questions remain unanswered about the role of grain boundary/interface, crystallographic orientations, and irradiation on the operative deformation mechanism for sub-micron scale irradiated Zr-2.5Nb samples at different temperatures. The experimental work described in the following chapters will address these issues.

References

- [1] D. D. Himbeault, C. K. Chow, and M. P. Puls, “Deformation behavior of irradiated Zr-2.5Nb pressure tube material,” *Metall. Mater. Trans. A*, vol. 25, no. 1, pp. 135–145, 1994.
- [2] R. a. Holt, “In-reactor deformation of cold-worked Zr–2.5Nb pressure tubes,” *J. Nucl. Mater.*, vol. 372, no. 2–3, pp. 182–214, Jan. 2008.
- [3] M. Griffiths, J. E. Winegar, and a. Buyers, “The transformation behaviour of the β -phase in Zr–2.5Nb pressure tubes,” *J. Nucl. Mater.*, vol. 383, no. 1–2, pp. 28–33, Dec. 2008.
- [4] 2012 Candu Energy, “EC6: Enhanced CANDU 6 Technical Summary,” Candu Energy, Mississauga, ON, Canada.
- [5] M. H. A. Piro, F. Wassermann, S. Grundmann, B. W. Leitch, and C. Tropea, “Progress in on-going experimental and computational fluid dynamic investigations within a CANDU fuel channel,” *Nucl. Eng. Des.*, vol. 299, pp. 184–200, 2016.
- [6] C. E. Lundin, “The determination of the equilibrium phase phase diagram,

zirconium-niobium,” United States, 1959.

- [7] V. F. Urbanic and M. Griffiths, “Microstructural Aspects of Corrosion and Hydrogen Ingress in Zr-2.5Nb,” in *Zirconium in the Nuclear Industry: Twelfth International Symposium*, G. P. Sabol and G. D. Moan, Eds. West Conshohocken, PA: ASTM International, 2000, pp. 641–657.
- [8] M. Griffiths, R. A. Holt, J. Li, and S. Saimoto, “Microstructural Science,” *ASM Int. Met. Park. OH*, vol. 26, pp. 293–302, 1999.
- [9] Y. S. Kim, “Role of Twinning and Slip in Deformation of a Zr-2.5Nb Tube,” in *Zirconium in the Nuclear Industry: 15th International Symposium*, B. Kammenzind and M. Limbäck, Eds. West Conshohocken, PA: ASTM International, 2009, pp. 227–243.
- [10] B. Bose and R. J. Klassen, “Effect of Zr⁺ion irradiation on the mechanical anisotropy of Zr-2.5%Nb pressure tube material,” *J. Nucl. Mater.*, vol. 405, no. 2, pp. 138–143, 2010.
- [11] H. Abdolvand and M. R. Daymond, “Multi-scale modeling and experimental study of twin inception and propagation in hexagonal close-packed materials using a crystal plasticity finite element approach - Part I: Average behavior,” *J. Mech. Phys. Solids*, vol. 61, no. 3, pp. 783–802, 2013.
- [12] J. Gong, T. Benjamin Britton, M. A. Cuddihy, F. P. E. Dunne, and A. J. Wilkinson, “(a) Prismatic, (a) basal, and (c+a) slip strengths of commercially pure Zr by micro-cantilever tests,” *Acta Mater.*, vol. 96, pp. 249–257, 2015.

- [13] I. J. Beyerlein and C. N. Tomé, “A dislocation-based constitutive law for pure Zr including temperature effects,” *Int. J. Plast.*, vol. 24, no. 5, pp. 867–895, 2008.
- [14] A. Luque, M. Ghazisaeidi, and W. a Curtin, “Deformation modes in magnesium (0 0 1) and (011-1) single crystals: Simulations versus experiments,” *Model. Simul. Mater. Sci. Eng.*, vol. 21, no. 4, p. 045010, Jun. 2013.
- [15] R. Ding, J. Gong, A. J. Wilkinson, and I. P. Jones, “ $\langle c+a \rangle$ Dislocations in deformed Ti–6Al–4V micro-cantilevers,” *Acta Mater.*, vol. 76, pp. 127–134, Sep. 2014.
- [16] R. Ding, J. Gong, A. J. Wilkinson, and I. P. Jones, “A study of dislocation transmission through a grain boundary in hcp Ti-6Al using micro-cantilevers,” *Acta Mater.*, vol. 103, pp. 416–423, 2016.
- [17] J. Gong and A. J. Wilkinson, “Micro-cantilever testing of $\langle a \rangle$ prismatic slip in commercially pure Ti,” *Philos. Mag.*, vol. 91, no. 7–9, pp. 1137–1149, Mar. 2011.
- [18] T. S. Jun, G. Sernicola, F. P. E. Dunne, and T. B. Britton, “Local deformation mechanisms of two-phase Ti alloy,” *Mater. Sci. Eng. A*, vol. 649, pp. 39–47, 2016.
- [19] Z. Zhang, T. S. Jun, T. B. Britton, and F. P. E. Dunne, “Intrinsic anisotropy of strain rate sensitivity in single crystal alpha titanium,” *Acta Mater.*, vol. 118, pp. 317–330, 2016.
- [20] P. J. Ashton *et al.*, “The effect of the beta phase on the micromechanical response of dual-phase titanium alloys,” *Int. J. Fatigue*, vol. 100, pp. 377–387, 2017.

- [21] T.-S. Jun *et al.*, “The role of β -titanium ligaments in the deformation of dual phase titanium alloys,” *Mater. Sci. Eng. A*, vol. 746, pp. 394–405, 2019.
- [22] H. E. Weekes *et al.*, “In situ micropillar deformation of hydrides in Zircaloy-4,” *Acta Mater.*, vol. 92, pp. 81–96, 2015.
- [23] S. Wang, S. Kalácska, X. Maeder, J. Michler, F. Giuliani, and T. Ben Britton, “The effect of δ -hydride on the micromechanical deformation of a Zr alloy studied by in situ high angular resolution electron backscatter diffraction,” *Scr. Mater.*, vol. 173, pp. 101–105, 2019.
- [24] H. Chan, S. G. Roberts, and J. Gong, “Micro-scale fracture experiments on zirconium hydrides and phase boundaries,” *J. Nucl. Mater.*, vol. 475, pp. 105–112, 2016.
- [25] J. R. Greer, W. C. Oliver, and W. D. Nix, “Size dependence of mechanical properties of gold at the micron scale in the absence of strain gradients,” *Acta Mater.*, vol. 53, no. 6, pp. 1821–1830, 2005.
- [26] M. D. Uchic, D. M. Dimiduk, J. N. Florando, and W. D. Nix, “Sample dimensions influence strength and crystal plasticity,” *Science*, vol. 305, no. 5686, pp. 986–9, Aug. 2004.
- [27] S. S. Brenner, “Tensile Strength of Whiskers,” *J. Appl. Phys.*, vol. 27, no. 12, p. 1484, 1956.
- [28] S. S. Brenner, “Strength of Gold Whiskers,” *J. Appl. Phys.*, vol. 30, no. 2, p. 266,

1959.

- [29] S. S. Brenner, “Plastic Deformation of Copper and Silver Whiskers,” *J. Appl. Phys.*, vol. 28, no. 9, p. 1023, 1957.
- [30] M. D. Uchic and D. M. Dimiduk, “A methodology to investigate size scale effects in crystalline plasticity using uniaxial compression testing,” *Mater. Sci. Eng. A*, vol. 400–401, no. 1-2 SUPPL., pp. 268–278, 2005.
- [31] M. D. Uchic, P. A. Shade, and D. M. Dimiduk, “Plasticity of Micrometer-Scale Single Crystals in Compression,” *Annu. Rev. Mater. Res.*, vol. 39, no. 1, pp. 361–386, 2009.
- [32] J. R. Greer and J. T. M. De Hosson, “Plasticity in small-sized metallic systems: Intrinsic versus extrinsic size effect,” *Prog. Mater. Sci.*, vol. 56, no. 6, pp. 654–724, Aug. 2011.
- [33] O. Kraft, P. a. Gruber, R. Mönig, and D. Weygand, “Plasticity in Confined Dimensions,” *Annu. Rev. Mater. Res.*, vol. 40, no. 1, pp. 293–317, Jun. 2010.
- [34] S. Chen, J. Duan, Y. Tang, and S. Zhang Qiao, “Hybrid hydrogels of porous graphene and nickel hydroxide as advanced supercapacitor materials.,” *Chemistry*, vol. 19, no. 22, pp. 7118–24, May 2013.
- [35] A. Kunz, S. Pathak, and J. R. Greer, “Size effects in Al nanopillars: Single crystalline vs. bicrystalline,” *Acta Mater.*, vol. 59, no. 11, pp. 4416–4424, 2011.
- [36] A. T. Jennings, J. Li, and J. R. Greer, “Emergence of strain-rate sensitivity in Cu

- nanopillars: Transition from dislocation multiplication to dislocation nucleation,” *Acta Mater.*, vol. 59, no. 14, pp. 5627–5637, Aug. 2011.
- [37] M. B. Lowry *et al.*, “Achieving the ideal strength in annealed molybdenum nanopillars,” *Acta Mater.*, vol. 58, no. 15, pp. 5160–5167, Sep. 2010.
- [38] M. Zaiser *et al.*, “Strain bursts in plastically deforming molybdenum micro- and nanopillars,” *Philos. Mag.*, vol. 88, no. 30–32, pp. 3861–3874, Oct. 2008.
- [39] D. Jang, C. T. Gross, and J. R. Greer, “Effects of size on the strength and deformation mechanism in Zr-based metallic glasses,” *Int. J. Plast.*, vol. 27, no. 6, pp. 858–867, Jun. 2011.
- [40] N. L. Okamoto, M. Inomoto, H. Adachi, H. Takebayashi, and H. Inui, “Micropillar compression deformation of single crystals of the intermetallic compound ζ -FeZn₁₃,” *Acta Mater.*, vol. 65, pp. 229–239, Feb. 2014.
- [41] D. Kiener, P. J. Guruprasad, S. M. Keralavarma, G. Dehm, and a. a. Benzerga, “Work hardening in micropillar compression: In situ experiments and modeling,” *Acta Mater.*, vol. 59, no. 10, pp. 3825–3840, Jun. 2011.
- [42] W. D. Nix, J. R. Greer, G. Feng, and E. T. Lilleodden, “Deformation at the nanometer and micrometer length scales: Effects of strain gradients and dislocation starvation,” *Thin Solid Films*, vol. 515, no. 6, pp. 3152–3157, Feb. 2007.
- [43] C. Shin, S. Lim, H. Jin, P. Hosemann, and J. Kwon, “Development and testing of microcompression for post irradiation characterization of ODS steels,” *J. Nucl.*

Mater., vol. 444, no. 1–3, pp. 43–48, Jan. 2014.

- [44] Q. Sun, Q. Guo, X. Yao, L. Xiao, J. R. Greer, and J. Sun, “Size effects in strength and plasticity of single-crystalline titanium micropillars with prismatic slip orientation,” *Scr. Mater.*, vol. 65, no. 6, pp. 473–476, Sep. 2011.
- [45] C. M. Byer, B. Li, B. Cao, and K. T. Ramesh, “Microcompression of single-crystal magnesium,” *Scr. Mater.*, vol. 62, no. 8, pp. 536–539, 2010.
- [46] C. M. Byer and K. T. Ramesh, “Effects of the initial dislocation density on size effects in single-crystal magnesium,” *Acta Mater.*, vol. 61, no. 10, pp. 3808–3818, 2013.
- [47] E. Lilleodden, “Microcompression study of Mg (0001) single crystal,” *Scr. Mater.*, vol. 62, no. 8, pp. 532–535, Apr. 2010.
- [48] K. E. Prasad, K. Rajesh, and U. Ramamurty, “Micropillar and macropillar compression responses of magnesium single crystals oriented for single slip or extension twinning,” *Acta Mater.*, vol. 65, pp. 316–325, Feb. 2014.
- [49] S. Jin, S. Xie, M. J. Burek, Z. Jahed, and T. Y. Tsui, “Microstructure and mechanical properties of sub-micron zinc structures,” *J. Mater. Res.*, vol. 27, no. 16, pp. 2140–2147, May 2012.
- [50] S. Jin, M. J. Burek, N. D. Evans, Z. Jahed, and T. Y. Tsui, “Fabrication and plastic deformation of sub-micron cadmium structures,” *Scr. Mater.*, vol. 66, no. 9, pp. 619–622, May 2012.

- [51] S. Sagat, C. E. Coleman, M. Griffiths, and B. J. S. Wilkins, “The Effect of Fluence and Irradiation Temperature on Delayed Hydride Cracking in Zr-2.5Nb,” in *Zirconium in the Nuclear Industry: Tenth International Symposium*, A. M. Garde and E. R. Bradley, Eds. West Conshohocken, PA: ASTM International, 1994, pp. 35–61.
- [52] P. Landau, Q. Guo, P. Hosemann, Y. Wang, and J. R. Greer, “Deformation of as-fabricated and helium implanted 100nm-diameter iron nano-pillars,” *Mater. Sci. Eng. A*, vol. 612, pp. 316–325, Aug. 2014.
- [53] D. E. J. Armstrong, C. D. Hardie, J. S. K. L. Gibson, a. J. Bushby, P. D. Edmondson, and S. G. Roberts, “Small-scale characterisation of irradiated nuclear materials: Part II nanoindentation and micro-cantilever testing of ion irradiated nuclear materials,” *J. Nucl. Mater.*, pp. 1–8, Jan. 2015.
- [54] P. D. Edmondson, a. London, a. Xu, D. E. J. Armstrong, and S. G. Roberts, “Small-scale characterisation of irradiated nuclear materials: Part I – Microstructure,” *J. Nucl. Mater.*, Nov. 2014.
- [55] M. A. Pouchon, J. Chen, R. Ghisleni, J. Michler, and W. Hoffelner, “Characterization of irradiation damage of ferritic ODS alloys with advanced micro-sample methods,” *Exp. Mech.*, vol. 50, no. 1, pp. 79–84, 2010.
- [56] C. Yan, R. Wang, Y. Wang, X. Wang, and G. Bai, “Effects of ion irradiation on microstructure and properties of zirconium alloys-A review,” *Nucl. Eng. Technol.*, vol. 47, no. 3, pp. 323–331, 2015.

- [57] N. Kheradmand, H. Vehoff, and A. Barnoush, “An insight into the role of the grain boundary in plastic deformation by means of a bicrystalline pillar compression test and atomistic simulation,” *Acta Mater.*, vol. 61, no. 19, pp. 7454–7465, 2013.
- [58] K. S. Ng and A. H. W. Ngan, “Deformation of micron-sized aluminium bi-crystal pillars,” *Philos. Mag.*, vol. 89, no. 33, pp. 3013–3026, 2009.
- [59] P. J. Imrich, C. Kirchlechner, C. Motz, and G. Dehm, “Differences in deformation behavior of bicrystalline Cu micropillars containing a twin boundary or a large-angle grain boundary,” *Acta Mater.*, vol. 73, pp. 240–250, 2014.
- [60] I. Tiba, T. Richeton, C. Motz, H. Vehoff, and S. Berbenni, “Incompatibility stresses at grain boundaries in Ni bicrystalline micropillars analyzed by an anisotropic model and slip activity,” *Acta Mater.*, vol. 83, pp. 227–238, 2015.
- [61] C. S. Kaira, S. S. Singh, A. Kirubanandham, and N. Chawla, “Microscale deformation behavior of bicrystal boundaries in pure tin (Sn) using micropillar compression,” *Acta Mater.*, vol. 120, pp. 56–67, 2016.
- [62] S. Cai, M. R. Daymond, and R. A. Holt, “Modeling the room temperature deformation of a two-phase zirconium alloy,” *Acta Mater.*, vol. 57, no. 2, pp. 407–419, 2009.
- [63] C. R. Cupp, “The effect of neutron irradiation on the mechanical properties of zirconium-2.5 % niobium alloy,” *J. Nucl. Mater.*, vol. 6, no. 3, pp. 241–255, 1962.
- [64] Q. Wang, F. Long, Z. Wang, N. Guo, and M. R. Daymond, “Orientation dependent

- evolution of plasticity of irradiated Zr-2.5Nb pressure tube alloy studied by nanoindentation and finite element modeling,” *J. Nucl. Mater.*, vol. 512, pp. 371–384, 2018.
- [65] Q. Wang, C. Cochrane, F. Long, H. Yu, and M. R. Daymond, “Micropillar compression study on heavy ion irradiated Zr-2.5Nb pressure tube alloy,” *J. Nucl. Mater.*, vol. 511, pp. 487–495, 2018.
- [66] Q. Dong, H. Qin, Z. Yao, Q. Wang, and M. R. Daymond, “Effect of the addition of Cu on irradiation induced defects and hardening in Zr-Nb alloys,” *J. Nucl. Mater.*, vol. 519, pp. 10–21, 2019.
- [67] H. Yu, Z. Yao, Y. Idrees, H. K. Zhang, M. A. Kirk, and M. R. Daymond, “Accumulation of dislocation loops in the α phase of Zr Excel alloy under heavy ion irradiation,” *J. Nucl. Mater.*, vol. 491, pp. 232–241, 2017.
- [68] Q. Dong, H. Qin, Z. Yao, and M. R. Daymond, “Irradiation damage and hardening in pure Zr and Zr-Nb alloys at 573 K from self-ion irradiation,” *Mater. Des.*, vol. 161, pp. 147–159, 2019.
- [69] M. Griffiths, N. Wang, A. Buyers, and S. A. Donohue, “Effect of irradiation damage on the deformation properties of Zr-2.5Nb pressure tubes,” *J. ASTM Int.*, vol. 5, no. 1, pp. 1–9, 2008.
- [70] A. Jostsons, P. M. Kelly, and R. G. Blake, “The nature of dislocation loops in neutron irradiated zirconium,” *J. Nucl. Mater.*, vol. 66, no. 3, pp. 236–256, 1977.

- [71] L. Tournadre *et al.*, “Experimental study of the nucleation and growth of c-component loops under charged particle irradiations of recrystallized Zircaloy-4,” *J. Nucl. Mater.*, vol. 425, no. 1, pp. 76–82, 2012.
- [72] A. Akhtar and A. Teghtsoonian, “Plastic Deformation of Zirconium Single Crystals,” *Acta Metall.*, vol. 19, pp. 88–94, 1971.
- [73] A. Akhtar, “Prismatic slip in zirconium single crystals at elevated temperatures,” *Metall. Trans. A*, vol. 6, no. 6, pp. 1217–1222, 1975.
- [74] A. Akhtar, “Compression of zirconium single crystals parallel to the c-axis,” *J. Nucl. Mater.*, vol. 47, no. 1, pp. 79–86, 1973.
- [75] N. Christodoulou, P. A. Turner, E. T. C. Ho, C. K. Chow, and M. R. Levi, “Anisotropy of Yielding in a Zr-2.5Nb Pressure Tube Material,” *Met. Mat Trans A*, vol. 31, no. February, pp. 409–420, 2000.
- [76] F. Long *et al.*, “Effect of neutron irradiation on deformation mechanisms operating during tensile testing of Zr-2.5Nb,” *Acta Mater.*, vol. 102, pp. 352–363, 2016.
- [77] A. W. Colldewei, A. Baris, P. Spätig, and S. Abolhassani, “Evaluation of mechanical properties of irradiated zirconium alloys in the vicinity of the metal-oxide interface,” *Mater. Sci. Eng. A*, 2018.
- [78] R. O. Oviasuyi and R. J. Klassen, “Assessment of the anisotropic flow stress and plastic strain of Zr–2.5%Nb pressure tubes at temperature from 25°C to 300°C,” *J. Nucl. Mater.*, vol. 429, no. 1–3, pp. 7–12, Oct. 2012.

- [79] R. O. Oviasuyi and R. J. Klassen, “Anisotropic deformation of Zr ion irradiated Zr – 2 . 5 % Nb micro-pillars at 25 ° C,” *J. Nucl. Mater.*, vol. 421, no. 1–3, pp. 54–57, 2012.

Chapter 3

3 Experimental Design and Techniques

The prime objective of this thesis was to investigate the mechanical properties of Zr-2.5%Nb pressure tube at different implantation and test temperatures for micron-sized samples so that the impact of micron-sized scratches inside the pressure tube could be assessed properly. In this chapter, a brief description will be provided about sample preparation, design of the experiments, and data collection techniques used in this thesis.

3.1 Material

All the experiments carried out in this thesis, were performed on small rectangular samples, about 1 cm x 1 cm x 0.4 cm, cut from a ring of Zr-2.5%Nb¹ CANDU pressure tube off-cut supplied by Canadian Nuclear Laboratories (CNL). The side faces of the rectangular samples were labeled as AN, RN, and TN in reference to the Axial, Radial, and Transverse directions of the tube (Figure 3.1). The sides of the rectangular samples were polished and chemically etched. Scanning Electron Microscopy (SEM) was used to obtain images of the microstructure on the AN and TN faces. The microstructure mainly comprises of hcp α_{Zr} grains that are highly elongated in the axial direction of the tube. Surrounding the α -grains is a thin film of bcc β_{Nb} phase. The average α -grain size is about 0.2, 1.0 and 5.0 μ m in the radial, transverse and axial directions of the pressure tube while the β phase is between 20-500 nm thickness.

¹ Chemical composition of Zr-2.5% Nb--- Nb- (2.4-2.8 wt%), O- (900-1300 ppm), N-($<$ 65 ppm), H-($<$ 5 ppm), Fe-($<$ 1300 ppm)

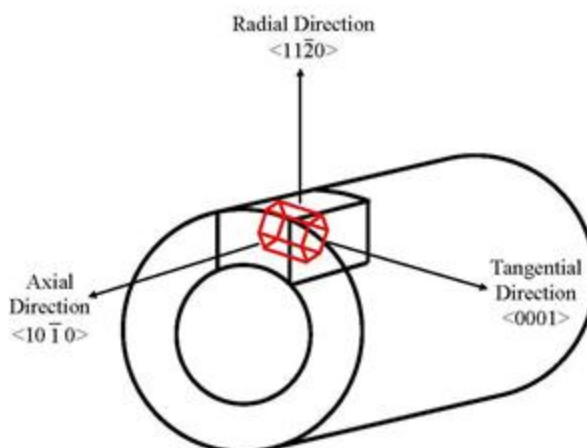


Figure 3.1: Schematic diagram of the pressure tube depicting the orientation of the Axial Normal (AN), Radial Normal (RN), and Transverse Normal (TN) planes. The predominant orientation of the hexagonal unit cell of the α -phase is shown in red [1]

3.2 Micropillar fabrication

As we needed to investigate localized deformation mechanism of this pressure tube, regions of the microstructure that contained large α -grains were identified on the AN and TN planes. It was from these regions that small cylindrical single α crystal micropillars were fabricated. To fabricate the α/β micropillars, suitable locations were chosen so that the α_{Zr} phase occupies half of the pillar top surface. The micropillars were fabricated using a Focused Ion Beam (FIB) microscope (LEO Zeiss 1540XB *FIB/SEM*) operating with a 30 keV 10 nA Ga^+ ion beam. The pillars were about 1 μm in diameter and 3 μm in height. The pillar tops were flattened by ion milling with a low energy 30 keV 50 pA Ga^+ ion beam. The experimental matrix is given below. Data obtained from first three sets of experiments are discussed in Chapters 4 and 5. Chapter 4 presents the results for α_{Zr} micropillars compressed at different conditions, whereas chapter 5 presents the results for α_{Zr}/β_{Nb} micropillars. The final two sets of experiments were conducted at 250°C, to

observe the effect of test temperature on the deformation behavior of implanted and non-implanted samples. Experiment number 1 and 2 were conducted at University of Western Ontario, experiment number 3 was conducted at RMTL (Reactor Materials Testing Laboratory) at Queen's University, and experiment number 4 and 5 were conducted at Chalk River Nuclear Laboratories.

Table 3.1: Experimental matrix

Exp. No	Pillar direction	Top surface of pillar	Implantation temp	Compression temp
1	AN and TN	α_{Zr} and α_{Zr}/β_{Nb}	Non-implanted	Room Temperature
2	AN and TN	α_{Zr} and α_{Zr}/β_{Nb}	Room Temperature	Room Temperature
3	AN and TN	α_{Zr} and α_{Zr}/β_{Nb}	300° C	Room Temperature
4	AN and TN	α_{Zr} and α_{Zr}/β_{Nb}	300°C	250°C
5	AN and TN	α_{Zr} and α_{Zr}/β_{Nb}	Non-implanted	250°C

3.3 Electron Backscattered Diffraction (EBSD)

Applying EBSD technique, diffraction patterns can be measured from a sample located inside an electron microscope. Electron beam is used to hit the surface of a tilted sample. As a result of elastic interaction between the incident beam and planes of atoms, Kikuchi patterns form on a phosphor screen. By analyzing the Kikuchi bands, the grain orientation could be determined.

The flat top region of each micropillar was analyzed with Electron Backscattered Diffraction (EBSD) to determine the orientation of the (0001) basal plane normal relative to the axial loading direction of the micro-pillar. The deviation from basal plane normal has been mentioned as Basal Misorientation Angle, θ (Figure 3.2). Each grain has a specific orientation which can be expressed by Euler angles. Later these angles were used to convert global coordinates to crystal local coordinates by using a rotation matrix. Because of the relatively strong transverse texture of the basal plane normal in Zr-2.5%Nb pressure tubes, the α -phase of the micro-pillars fabricated from the TN plane had small misorientation angles, although the precise angle varied from one pillar to another, while those fabricated from the AN plane had comparatively larger misorientation angles. All the EBSD analyses were performed with a JEOL 6600 FEG-SEM and an Oxford Instruments EBSD camera at the Zircon and Accessory Phase (ZAP) lab at the University of Western Ontario.

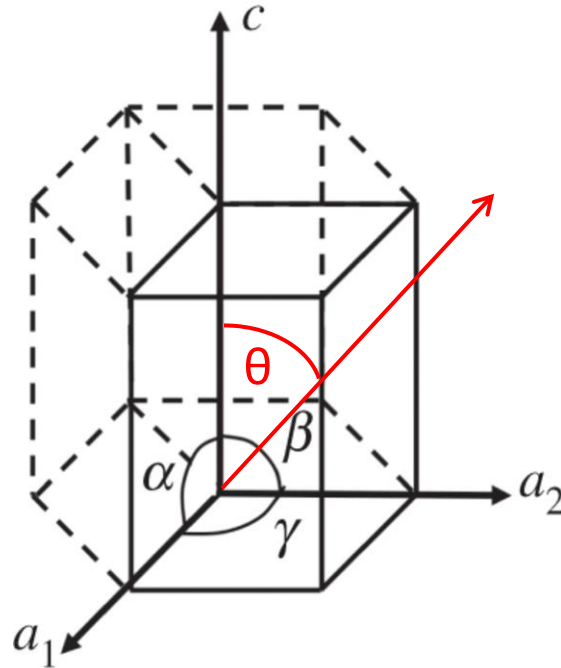


Figure 3.2: Schematic representation of basal misorientation angle, θ

3.4 Ion implantation

Selected micro-pillars were Zr^+ implanted at 25°C and 300°C with the tandem ion accelerator located at the University of Western Ontario. The implantations were performed with $8.5\text{ MeV } Zr^+$ ions to a fluence of 7.07×10^{19} ions/ m^2 to generate a peak irradiation depth of about $3\ \mu\text{m}$ and an average ion-induced displacement damage of approximately 6 displacements per atom (dpa) (as determined using the SRIM software). The damage rate in terms of Number/(Angstrom-Ion) was determined by using the Kinchin-Pease option in SRIM [2]. The damage profile was calculated using the equation [3] written below,

$$\text{Damage (dpa)} = \frac{\phi \times 10^8 \times \nu}{N}$$

Here, ϕ is the fluence in ions/cm², ν is the damage rate and N is the atomic number density in atoms/cm³. **Figure 3.3** shows the damage profile of the micropillars. As can be seen from the figure that on top of the pillar the damage level is low and it gradually increases to 25 dpa. The average damage level throughout the pillar can be considered as is about 6 dpa. It should be noted that the average neutron-induced radiation damage in a Zr-2.5%Nb pressure tube operating for thirty years in a CANDU reactor is about 40 dpa [4].

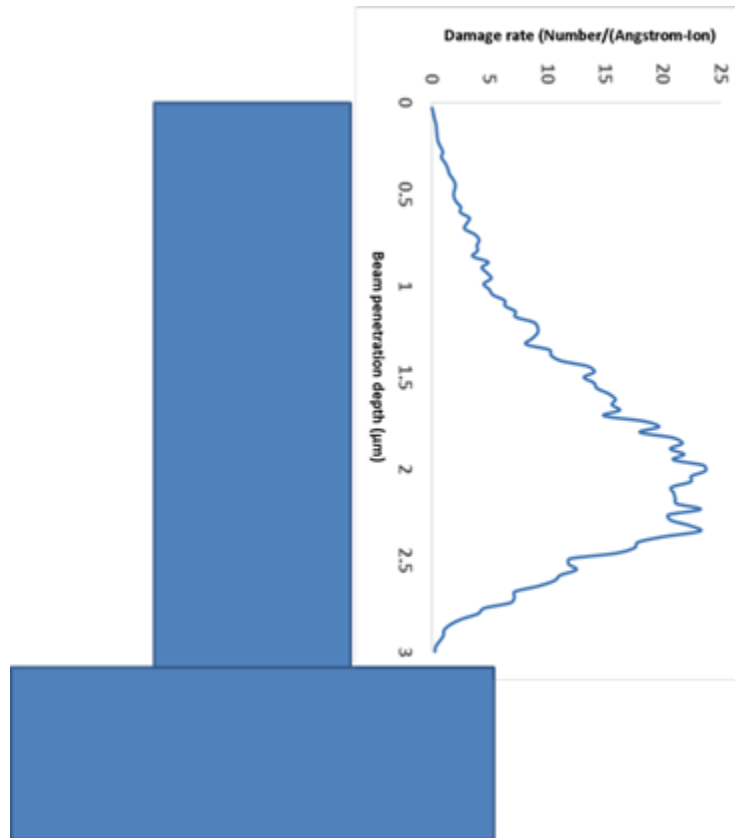


Figure 3.3: Irradiation damage profile of the micropillar

3.5 Micro-compression

The micropillars were then compressed using a nano-indentation hardness tester (Micro Materials, Wrexham UK) equipped with a 10 μm diameter flat punch diamond indenter. The compression tests were performed under load control to about 15% true strain at a loading rate of 0.10mN/sec at the University of Western Ontario (non-implanted and samples implanted at 25°C) and at the Queen's University (samples implanted at 300°C). Similar setup was maintained for all the experiments in both places to maintain continuity. Only the high temperature (250°C) experiments were conducted in-situ within an SEM at the Canadian Nuclear Laboratories, Chalk River.

References

- [1] B. Bose and R. J. Klassen, "Temperature dependence of the anisotropic deformation of Zr-2.5%Nb pressure tube material during micro-indentation," *J. Nucl. Mater.*, vol. 419, no. 1-3, pp. 235-240, Dec. 2011.
- [2] R. E. Stoller, M. B. Toloczko, G. S. Was, A. G. Certain, S. Dwaraknath, and F. A. Garner, "On the use of SRIM for computing radiation damage exposure," *Nucl. Instruments Methods Phys. Res.*, vol. 310, no. September, pp. 75-80, 2013.
- [3] M. Li, M. A. Kirk, P. M. Baldo, D. Xu, and B. D. Wirth, "Study of defect evolution by TEM with in situ ion irradiation and coordinated modeling," *Philos. Mag.*, vol. 92, no. 16, pp. 2048-2078, 2012.
- [4] D. H. Lister and W. G. Cook, "Nuclear Plant Materials and Corrosion," in *The Essential CANDU - a textbook on the CANDU nuclear power plant technology*, W. J.

Garland, Ed., Chapter 14, University Network of Excellence in Nuclear Engineering (UNENE).

Chapter 4

4 Effect of Zr⁺ irradiation damage and crystal orientation on the uniaxial deformation of Zr-2.5%Nb micro-pillars: Part 1, Deformation of single-phase α_{Zr} micro-pillars

The uniaxial flow stress of 1 μm diameter micro-pillars made from single α_{Zr} grains cut from Zr-2.5%Nb CANDU pressure tube material was assessed in the non-implanted condition and after 6.0 dpa Zr⁺ implantation performed at 25°C and 300°C to simulate neutron irradiation. The normal flow stress, at 10% strain, of the non-implanted micro-pillars was about 70% higher than that for larger diameter polycrystalline pillars and followed the trend expected for the length-scale dependence of flow stress of most ductile metals. The flow stress anisotropy also displays a significant length-scale dependence with a stronger length-scale dependence for micro-pillars that were loaded along the $\langle 0001 \rangle$ basal pole direction than along other directions. Zr⁺ implantation performed at 300°C resulted in increased tendency for irregular σ - ε flow response consistent with increased tendency for strain localization. The normalized shear stress of α_{Zr} micro-pillars aligned for single-slip deformation displayed a dependence upon crystal orientation that is consistent with deformation occurring by concurrent mechanisms of dislocation slip and twinning. These findings provide new information on the mechanisms by which small volume α_{Zr} phase ligaments, located in crack-tip regions, deform plastically and thus contribute to the ductile fracture toughness of neutron-irradiated Zr-2.5Nb CANDU pressure tubes.

4.1 Introduction

Zirconium alloys are used for structural components in heavy water moderated nuclear reactors. In Canadian CANDU reactors, extruded and cold-drawn Zr-2.5%Nb pressure tubes contain the uranium fuel bundles and transport heavy water primary coolant within the core. These tubes are mechanically anisotropic due to their microstructure consisting of elongated and crystallographically textured hcp α -Zr matrix grains surrounded by thin regions of the Nb-rich bcc β -phase [1][2]. Analysis of the ductile fracture of Zr-2.5%Nb pressure tubes (Figure 1) indicates that zirconium hydride fracture ahead of the crack tip, which results in the formation of unconstrained α_{Zr} or α_{Zr}/β_{Nb} ligaments extending between the fractured hydrides (Figure 4.1-4.2). In such a case, the crack growth is largely determined by the strength and ductility of these unconstrained ligaments. These ligaments are small, typically several micrometers in size, and thus their strength and deformation behaviour may be affected by their size through the well-known length-scale dependence of the flow stress of common ductile metal [3][4]. The hcp crystal structure of α -Zr means also that the flow stress will be anisotropic and the dependence of the degree of anisotropy on specimen size and irradiation-induced crystal damage are important topics that have been studied only by nano-indentation testing [5][6], with its associated complex multi-axial stress-strain state, and not with more direct uniaxial stress testing.

Although direct measurement of the mechanical response of unconstrained single phase α -Zr ligaments has, as yet, not been reported due primarily to their small micron-scale size, analysis of large hcp α -Zr single crystals, of pure Zr or Zircaloy alloys, has been studied[7][8][9]. Plastic deformation in these systems occurs by several possible

deformation mechanisms; namely, $\{0001\}\langle 0001 \rangle$ basal dislocation glide, $\{10\bar{1}0\}\langle 11\bar{2}0 \rangle$ prismatic dislocation glide, and $\{10\bar{1}1\}\langle 11\bar{2}3 \rangle$ pyramidal dislocation glide, and $\{1\bar{1}02\} \langle 10\bar{1}1 \rangle$ twinning (Figure 4.3)[10]. Of these mechanisms, prismatic and pyramidal slip are the most frequently reported however, recent experimental and theoretical analyses have demonstrated the significant contribution of concurrent twinning deformation, initiated from grain boundaries or grain boundary triple-points, during deformation [11]. The operation of concurrent deformation mechanisms will result in a non-constant measured critical resolved shear flow stress over a range of loading orientations.

In this work, we perform uniaxial compression tests on small micro-pillars made from FIB-fabricated, EBSD-indexed, single α -Zr grains of extruded and cold-drawn Zr-2.5%Nb pressure tube material. We analyse the measured stress-strain response and compare it to previously published data from larger polycrystalline Zr-2.5%Nb pillars to obtain information on the length-scale dependence and the anisotropic nature of the flow stress, critical resolved shear stress, and strain hardening coefficient. We also perform compression tests on α -Zr micro-pillars that were implanted with self-similar Zr^+ ions to induce atomic displacement, and generation of crystal defects, similar to those induced by neutron irradiation during in-reactor. This will enable us to deduce the effect of irradiation damage on the length-scale dependent stress-strain flow response of unconstrained α -Zr ligaments arising in the crack tip region of a CANDU pressure tube.

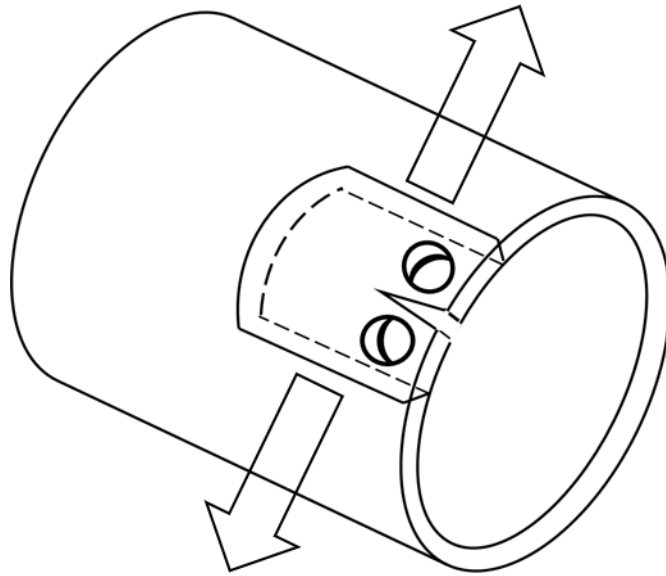


Figure 4.1: Illustration of curved compact tension specimen used for measuring fracture toughness of hydrides.

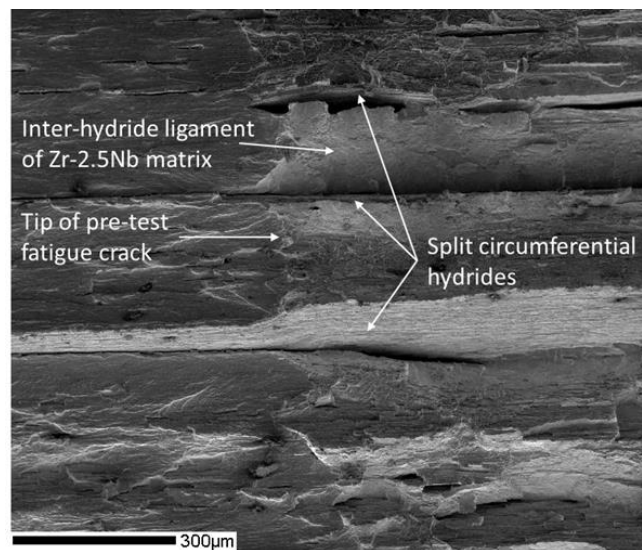


Figure 4.2: The fracture surface of a curved compact tension specimens machined from an irradiated Zr-2.5Nb pressure tube. These specimens were tested at 150 °C. Transverse cracks formed by the fracture of circumferential hydrides and the corresponding inter-hydride ligament of Zr-2.5Nb are indicated. Crack growth is from left-to-right beginning at the tip of the pre-test fatigue crack.

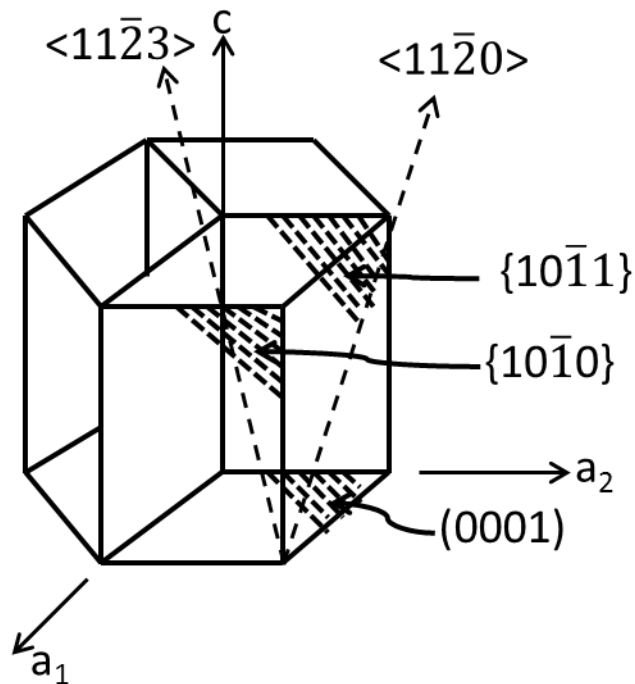


Figure 4.3: Diagram of an hcp unit cell depicting the basal (0001) , prismatic $\{10\bar{1}0\}$, and pyramidal $\{10\bar{1}1\}$ slip planes along which dislocation glide occurs.

4.2 Procedure

Small rectangular samples, about 1 cm x 1 cm x 0.4 cm, were cut from a ring of as-fabricated, non-irradiated, Zr-2.5%Nb CANDU pressure tube. The orthogonal faces of the samples were labeled as Axial Normal (AN), Radial Normal (RN), and Transverse Normal (TN) with respect to the Axial, Radial, and Transverse (circumferential) directions of the tube. The sides of the samples were polished and chemically etched. The microstructure is comprised of elongated hcp α -Zr grains surrounded by a thin film of bcc Nb-rich β -phase (**Figure 4.4**). The average α -Zr grain size is about 0.2, 1.0, and

5.0 μm in the radial, transverse and axial directions of the tube respectively. The β -phase was between 20-500 nm thickness. Scanning electron microscopy was used to identify particularly large α -Zr grains on the AN and TN faces of the samples. Small cylindrical single α -Zr crystal micropillars were then fabricated from these grains using Focused Ion Beam (FIB) milling.

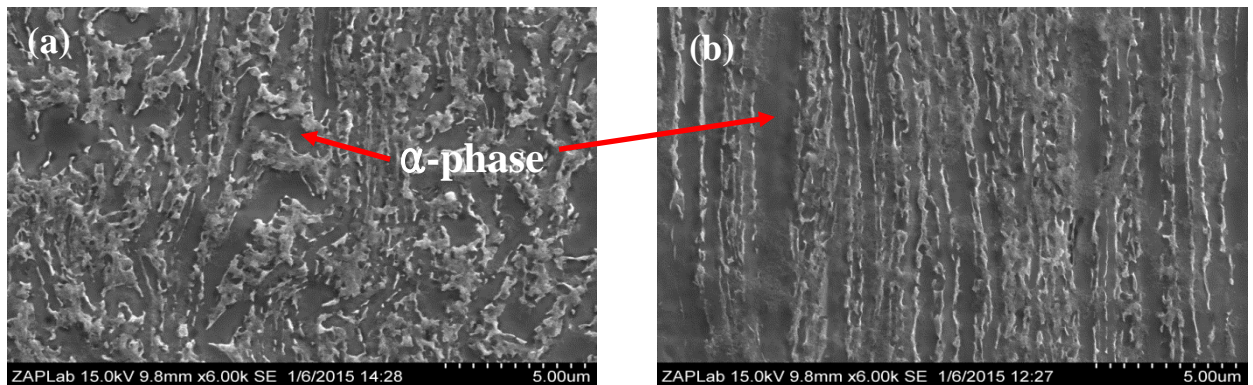


Figure 4.4: SEM images showing the microstructure of the (a) AN and (b) TN planes of the Zr-2.5%Nb pressure tube material. Large α_{Zr} grain regions, such as those indicated by the arrows, were selected from which to fabricate the single-crystal α_{Zr} micro-pillars.

The FIB milling was performed with a LEO Zeiss 1540 XB FIB SEM using a 30 keV 10 nA Ga^+ beam to create the coarse 1 μm diameter and 3 μm height micro-pillar geometry (Figure 4.5). The tops of the pillars were then flattened and polished with a low current, 50 pA, Ga^+ ion beam.

The polished flat top region of each micro-pillar was analyzed with Electron Backscattered Diffraction (EBSD) using a Hitachi SU6600 FEG-SEM equipped with an HKL EBSD detector/analysis system. The $\langle hklm \rangle$ crystal orientation corresponding to the axial direction of each micro-pillar was therefore determined.

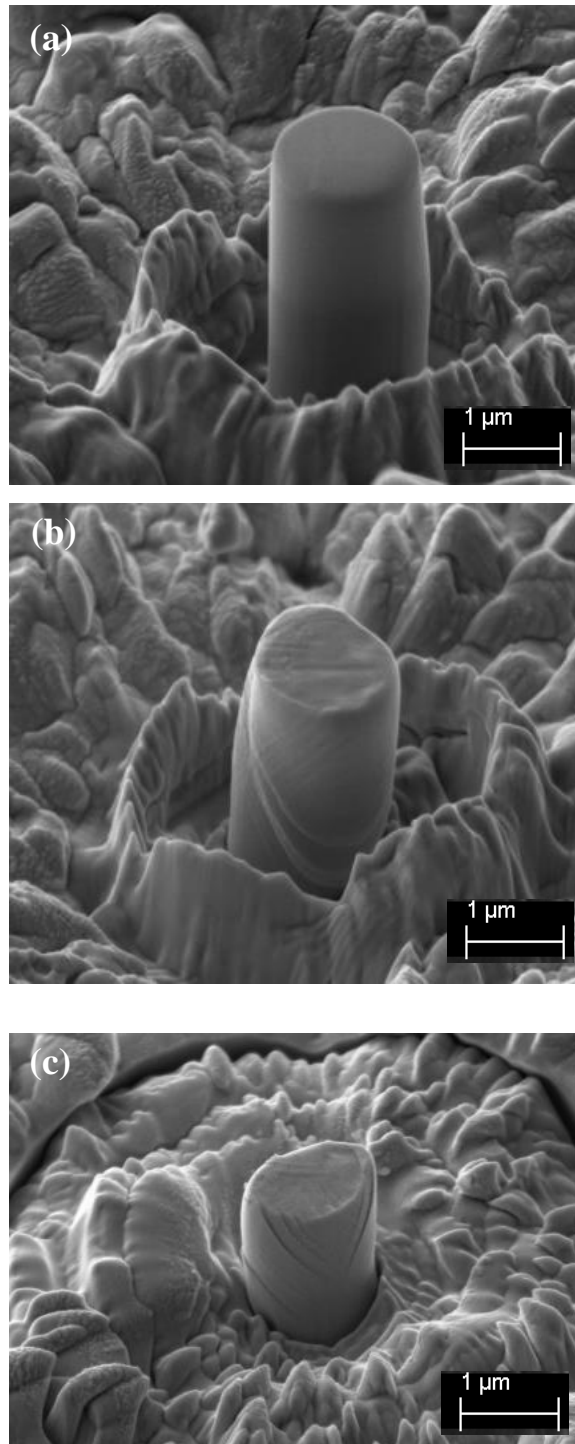


Figure 4.5: Typical 1 μm diameter FIB milled α -Zr micro-pillars made from the AN plane of the pressure tube: (a) before, (b) after uniaxial compression showing dislocation slip along a single plane, and (c) after compression showing slip along multiple crystal planes.

The micro-pillars were divided into two sets; non-implanted and Zr^+ implanted. The implanted pillars were exposed to 8.5 MeV Zr^+ ($\phi = 7.07 \times 10^{19}$ ions/m²) at either 25°C or 300°C using the Tandetron ion accelerator located at the University of Western Ontario (www.isw.physics.uwo.ca). This resulted in peak Zr^+ implantation depth of about 3 μ m as calculated by SRIM software [12]. The average ion-induced atomic displacement, ψ , expressed in units of displacement per atom (dpa), was determined using SRIM software and the Kinchin-Pease technique as [13]

$$\psi(dpa) = \frac{\phi \times 10^8 \times v}{N} \quad (1)$$

Here, v is the damage rate (atom displacements/ion, as calculated by SRIM) and N is the atomic number density (atoms/cm³). The average damage level throughout the micropillar was $\bar{\psi} \approx 6 dpa$.

The micro-pillars were then compressed at 25°C using a nano-indentation hardness tester equipped with a 10 μ m diameter diamond flat punch. The compression tests were performed under constant loading rate of 0.10 mN/sec to an axial true strain of about 15%. Fifty α_{Zr} micro-pillars were tested in this study (**Table 4 1**).

Table 4.1: Listing of micro-pillar compression tests performed in this study.

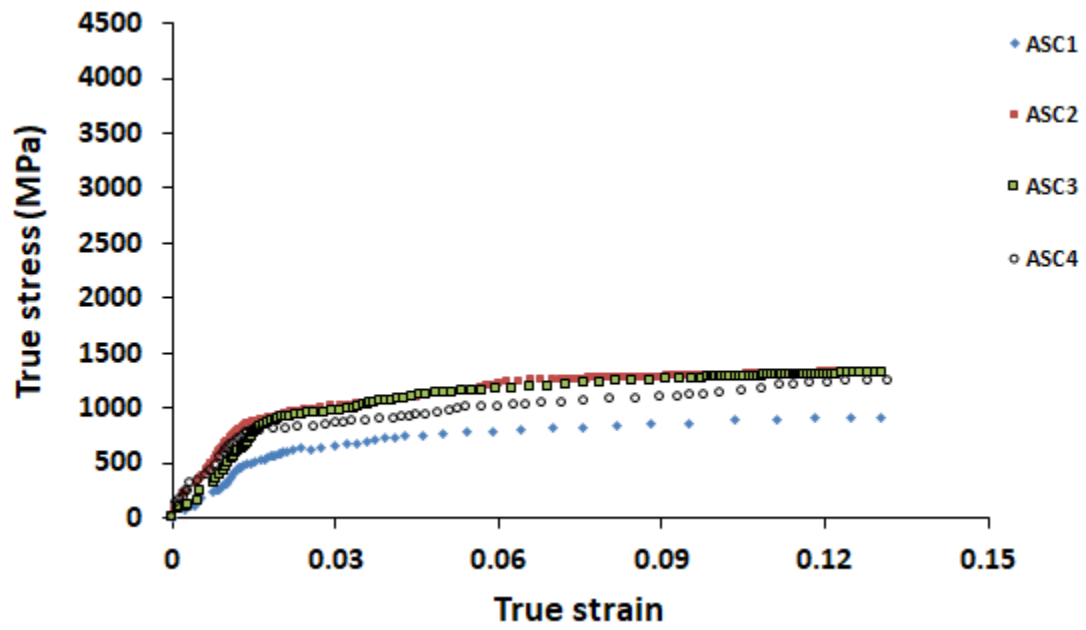
Ion implantation condition	Pressure tube plane from which the micro-pillar was fabricated	Number of micro-pillars tested.
Non-implanted ($\bar{\psi} = 0$)	AN	4
	TN	8
Zr ⁺ Implanted ($\bar{\psi} \approx 6dpa @ 25^\circ C$)	AN	9
	TN	9
Zr ⁺ Implanted ($\bar{\psi} \approx 6dpa @ 300^\circ C$)	AN	9
	TN	11
	Total number of micro-pillars tested	50

4.3 Results

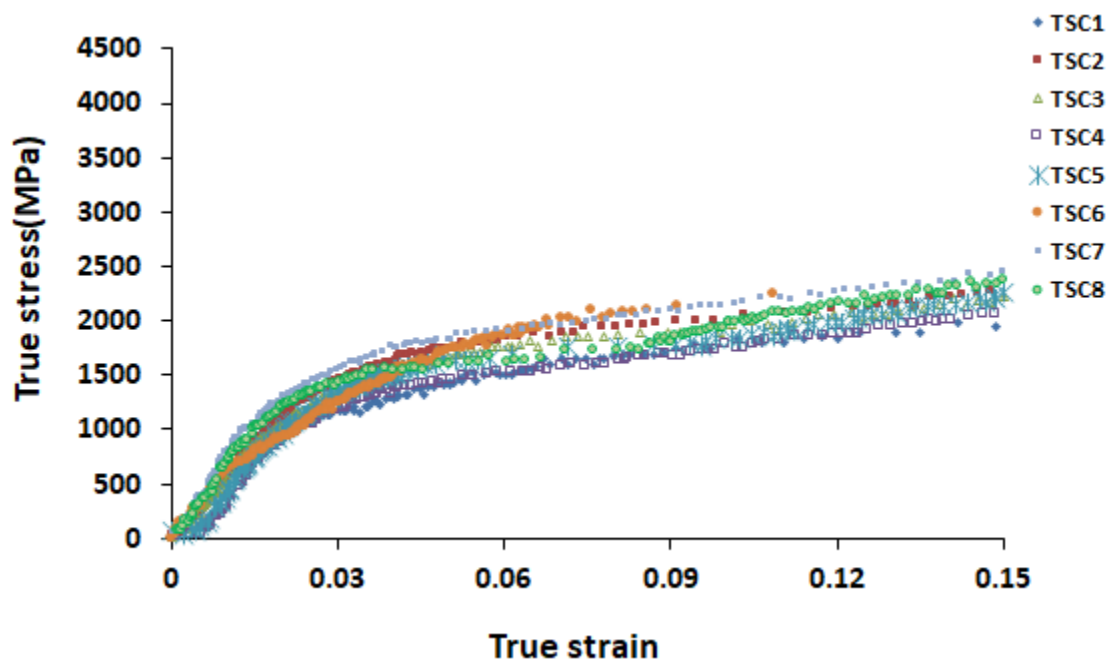
Results of EBSD analyses of the orientation of the α_{Zr} phase of each micro-pillar are shown in **Table 4.2-Table 4.4**. Although it is expected that pillars fabricated from the AN surface of the pressure tube would display axial direction significantly misoriented relative to the $\langle 0001 \rangle$ c-axis crystal direction while those fabricated from the TN surface would display axial directions more closely aligned with the $\langle 0001 \rangle$ direction, significant deviation was observed in pillars fabricated from each surface.

The uniaxial compression true stress – true strain curves of the α -Zr micro-pillars are shown in Figure 4.6-Figure 4.8. The stress-strain response shows considerable variability for all test conditions studied. In the following section we will demonstrate that this

variability is primarily the result of differences in the crystal orientations of the micro-pillars.

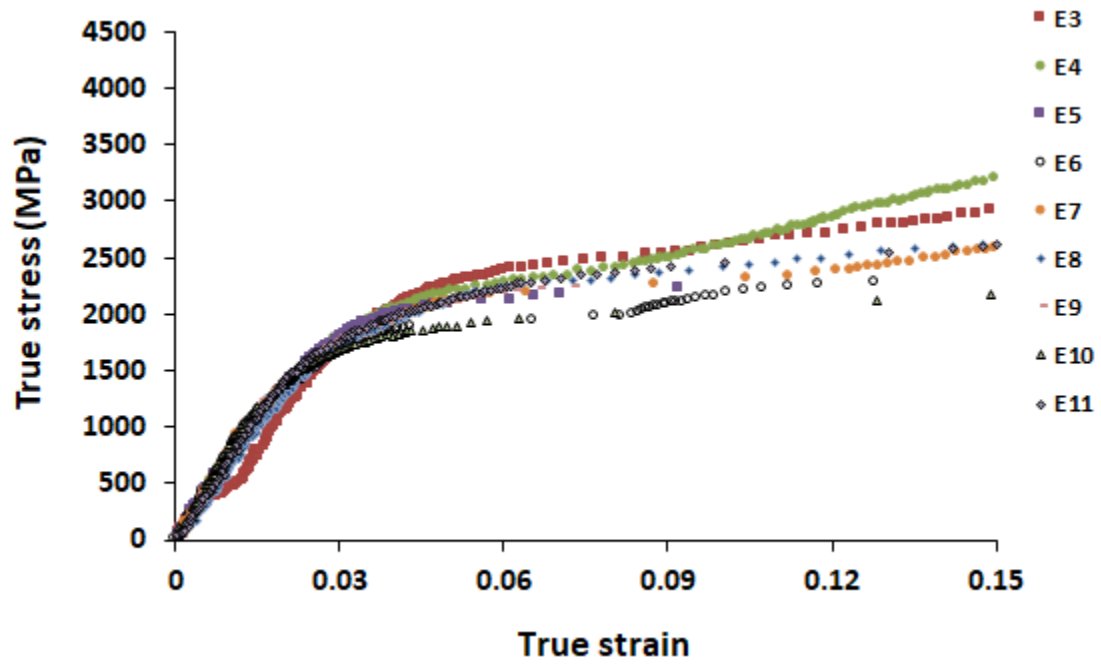


(a)

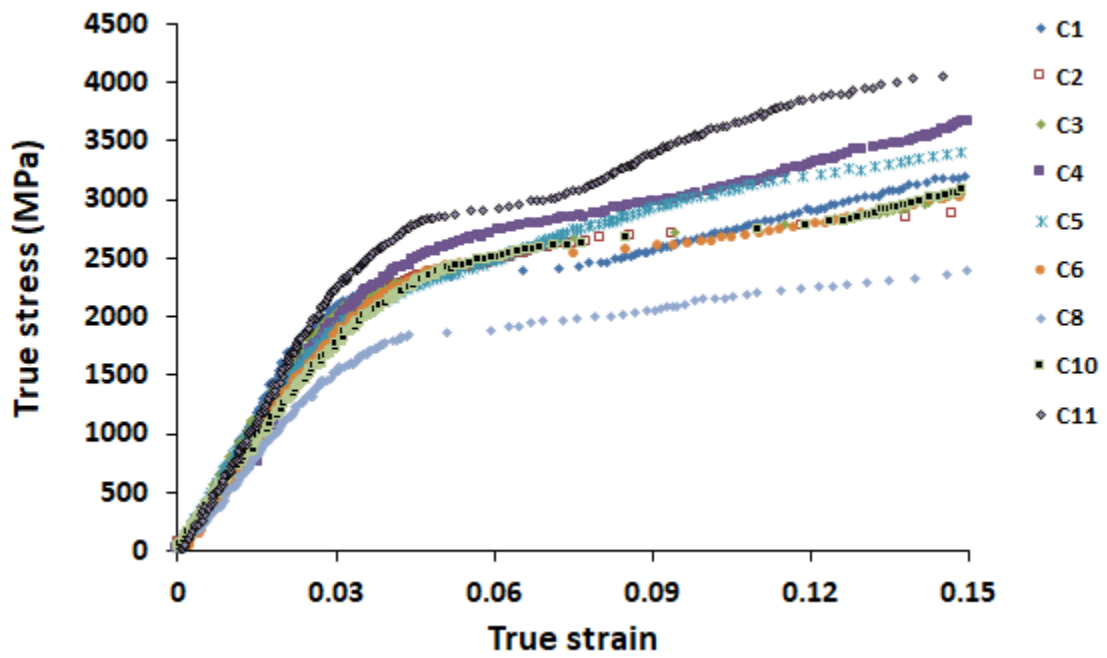


(b)

Figure 4.6: True stress versus true strain curves for the non-implanted α_{Zr} micro-pillars fabricated from the (a) AN and (b) TN planes of the Zr-2.5%Nb pressure tube.

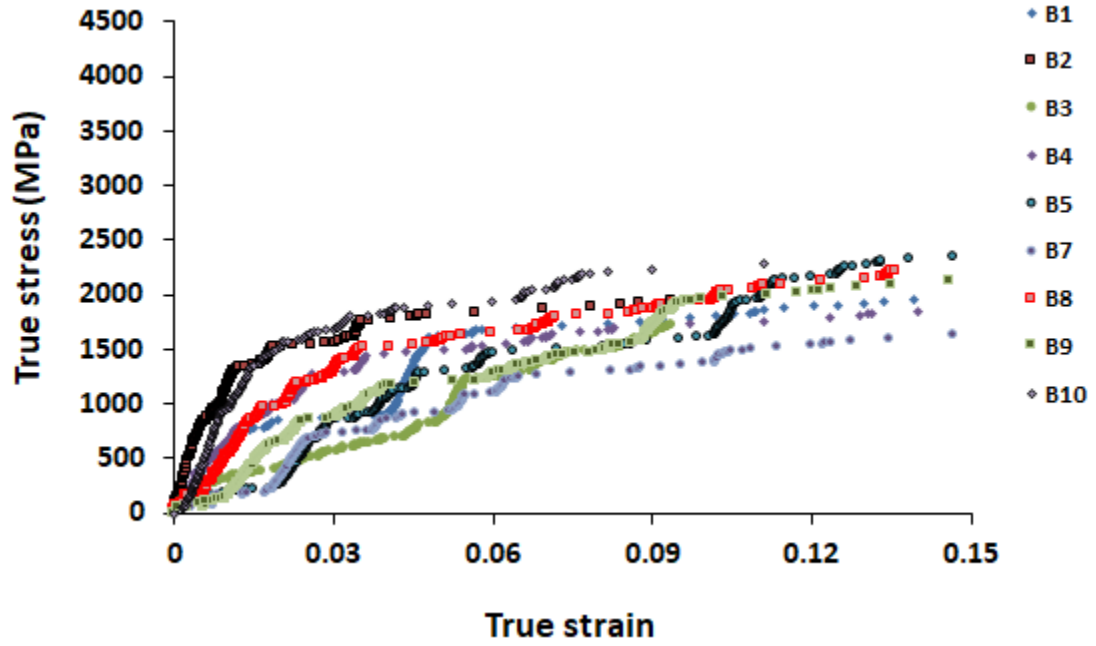


(a)

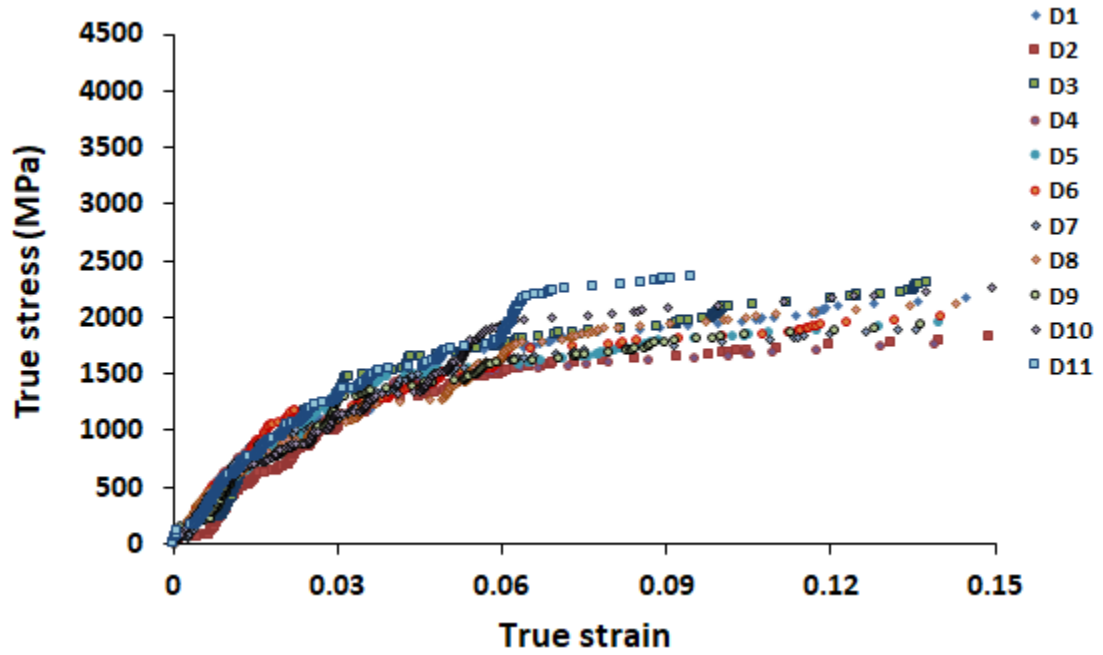


(b)

Figure 4.7: True stress versus true strain curves for the Zr^{+} -implanted ($\bar{\psi} \approx 6.0 \text{ dpa @ } 25^{\circ}C$) α_{Zr} micro-pillars fabricated from the (a) AN and (b) TN planes of the Zr-2.5%Nb pressure tube.



(a)



(b)

Figure 4.8: True stress versus true strain for the Zr⁺-implanted ($\bar{\psi} \approx 6.0 \text{ dpa @ } 300^\circ\text{C}$) α_{Zr} micro-pillars fabricated from the (a) AN and (b) TN planes of the Zr-2.5%Nb pressure tube

Table 4.2: Listing of orientation angle θ between the axial loading direction and the $\langle 0001 \rangle$ crystal direction for the various α_{Zr} micro-pillars tested in compression at 25°C . Also shown are the calculated Schmid factors, m , associated with deformation by dislocation slip along the basal, prismatic, pyramidal slip systems, and compressive twinning. Also shown is the calculated critical resolved shear stress $\tau_{\varepsilon=0.10}$ determined as the product of the maximum calculated Schmid factor and the measured normal flow stress $\sigma_{\varepsilon=0.10}$.

Micro-Pillar Orient ⁿ	Pillar Name	θ (°)	$\sigma_{\varepsilon=0.10}$ (MPa)	Schmid Factor, m (Eq. 2.4) $\left(\sigma_i = \tau_i^* / m \text{ (MPa)} \right)$				$\tau_{\varepsilon=0.10} = m_{max} \sigma_{\varepsilon=0.10}$ (MPa)
				Basal	Prismatic	Pyramidal	Twinning	
AN	ASC1	89.5	905276247.1	0.005	0.45	0.01	0.001	406.1
	ASC2	85.2	1296666084	0.04	0.45	0.03	0.003	584.4
	ASC3	66.3	1274553097	0.22	0.32	0.15	0.079	398.3
	ASC4	79.3	1170875204	0.10	0.45	0.06	0.016	525.6
TN	TSC1	79.4	2016993839	0.16	0.44	0.09	0.076	890.1
	TSC2	82.4	1902617674	0.13	0.49	0.07	0.025	934.4
	TSC3	69.1	1691930032	0.26	0.43	0.18	0.016	720.6
	TSC4	69.3	1764319310	0.31	0.43	0.17	0.024	763.6
	TSC5	58.6	2149004552	0.39	0.33	0.27	0.075	709.4
	TSC6	89.8	2119310078	0.003	0.48	0.02	0.072	1024.5
	TSC7	63.7	1636156242	0.35	0.37	0.23	0.030	600.6
	TSC8	69.6	1890693165	0.28	0.40	0.17	0.022	750.2

Table 4.3: Listing of orientation angle θ between the axial loading direction and the $\langle 0001 \rangle$ crystal direction for the various α_{Zr} micro-pillars implanted at 25°C and tested in compression at 25°C . Also shown are the calculated Schmid factors, m , associated with deformation by dislocation slip along the basal, prismatic, pyramidal slip systems, and compressive twinning. Also shown is the calculated

critical resolved shear stress $\tau_{\varepsilon=0.10}$ determined as the product of the maximum calculated Schmid factor and the measured normal flow stress $\sigma_{\varepsilon=0.10}$.

Micro-Pillar Orient ⁿ	Pillar Name	θ (°)	$\sigma_{\varepsilon=0.10}$ (MPa)	Schmid Factor, m (Eq. 2.4) $\left(\sigma_i = \tau_i^*/m \text{ (MPa)}\right)$				$\tau_{\varepsilon=0.10} = m_{max}\sigma_{\varepsilon=0.10}$ (MPa)	
				Basal	Prismatic	Pyramidal	Twinning		
AN	E3	84.7	2621103791	0.09	0.41	0.03	0.004	1061.8	
	E4	81.5	2618914520	0.15	0.41	0.03	0.011	1084.0	
	E5	74.9	2226283703	0.21	0.41	0.12	0.063	921.2	
	E6	74.5	2196689303	0.15	0.44	0.09	0.034	956.0	
	E7	76.2	2312185961	0.16	0.27	0.11	0.009	613.0	
	E8	82.3	2421606676	0.07	0.44	0.03	0.009	1068.7	
	E9	74	2562482927	0.13	0.40	0.07	0.038	1029.3	
	E10	78	2124524249	0.20	0.44	0.06	0.021	925.7	
	E11	78.8	2452034441	0.19	0.42	0.04	0.019	1029.9	
	TN	C1	1.8	2697041811	0.03	0.004	0.42	0.50	1348.3
		C2	33.4	2565927590	0.41	0.13	0.46	0.33	1266.8
C3		56.1	2274074348	0.37	0.25	0.30	0.12	1037.9	
C4		39.5	3063749668	0.41	0.18	0.43	0.27	1308.8	
C5		85.5	3985697278	0.05	0.49	0.04	0.008	1481.5	
C6		83	3440783617	0.10	0.43	0.05	0.11	1124.4	
C8		71.2	2150475949	0.28	0.32	0.16	0.005	683.6	
C9		63.1	3073531434	0.33	0.30	0.23	0.05	969.1	
C10		73	2026627969	0.26	0.32	0.14	0.01	862.7	

Table 4.4: Listing of orientation angle θ between the axial loading direction and the $\langle 0001 \rangle$ crystal direction for the various α_{Zr} micro-pillars implanted at 250°C and tested in compression at 25°C. Also shown are the calculated Schmid factors, m, associated with deformation by dislocation slip along the basal, prismatic, pyramidal slip systems, and compressive twinning. Also shown is the calculated critical resolved shear stress $\tau_{\varepsilon=0.10}$ determined as the product of the maximum calculated Schmid factor and the measured normal flow stress $\sigma_{\varepsilon=0.10}$.

Micro-Pillar Orient ⁿ	Pillar Name	θ (°)	$\sigma_{\varepsilon=0.10}$ (MPa)	Schmid Factor, m (Eq. 2.4) $\left(\sigma_i = \tau_i^*/m \text{ (MPa)}\right)$				$\tau_{\varepsilon=0.10} = m_{max}\sigma_{\varepsilon=0.10}$ (MPa)
				Basal	Prismatic	Pyramidal	Twinning	
AN	B1	48.9	1806801268	0.46	0.20	0.36	0.188	823.9
	B2	82.9	1936353365	0.11	0.48	0.07	0.060	920.9
	B3	9.7	1709104570	0.13	0.01	0.47	0.487	832.7
	B4	48	1760764199	0.50	0.24	0.33	0.224	875.5
	B5	30.9	1607648939	0.30	0.08	0.48	0.369	769.6
	B7	28.5	1559823181	0.36	0.10	0.47	0.374	644.0
	B8	68.5	1943452141	0.32	0.28	0.18	0.024	621.1
	B9	69.5	1969126199	0.29	0.36	0.17	0.018	702.4
	B10	20	2290256901	0.22	0.06	0.50	0.443	1135.1
	TN	D1	84.2	1961019976	0.10	0.47	0.04	0.001
D2		84.3	1675580034	0.10	0.49	0.05	0.094	818.4
D3		84.7	2054021134	0.09	0.44	0.02	0.004	908.9
D4		68.8	1641459143	0.33	0.42	0.14	0.062	685.8
D5		80.3	1817811896	0.17	0.47	0.06	0.009	845.5
D6		82.9	1819592528	0.12	0.43	0.02	0.008	783.5
D7		85.5	1777387743	0.08	0.36	0.04	0.004	635.4
D8		71.2	1981001254	0.30	0.41	0.10	0.052	820.7
D9		88.4	1818071104	0.03	0.47	0.02	0.003	854.7
D10		84.1	2141536760	0.10	0.42	0.02	0.005	906.3
D11		88.5	2358374312	0.016	0.49	0.03	0.009	1144.3

4.4 Discussion

The stress-strain response of the α_{Zr} micro-pillars indicate that the average normal flow stress of the TN oriented pillars is consistently greater than that of the AN oriented pillars. Zr^+ implantation ($\bar{\psi} = 6.0dpa$) increased the flow stress of pillars of both orientations and the effect was most pronounced when the implantation was performed at low temperature (Figure 4.9). Our data also indicate that the measured strain-hardening rate n was not significantly affected by Zr^+ implantation (Figure 4.10). It was also observed that increased Zr^+ implantation temperature, 300°C compared to 25°C,

increased the tendency for irregular flow response. This is indicated when $d\sigma/d\varepsilon$ is plotted versus ε (Figure 4.11). In this figure, the micropillars in the non-implanted and Zr^+ implanted ($T = 25^\circ\text{C}$) conditions displayed relatively smooth profiles, indicating smooth $\sigma - \varepsilon$ response, while those that were Zr^+ implanted at 300°C displayed considerable amounts of sudden strain jumps. Irregular flow response such as this is consistent with increased thermally-activated defect accumulation during Zr^+ implantation at 300°C . This mechanism has been observed to be operative in neutron-irradiated polycrystalline Zr-2.5Nb and has been associated to the tendency for strain localization in this material [14].

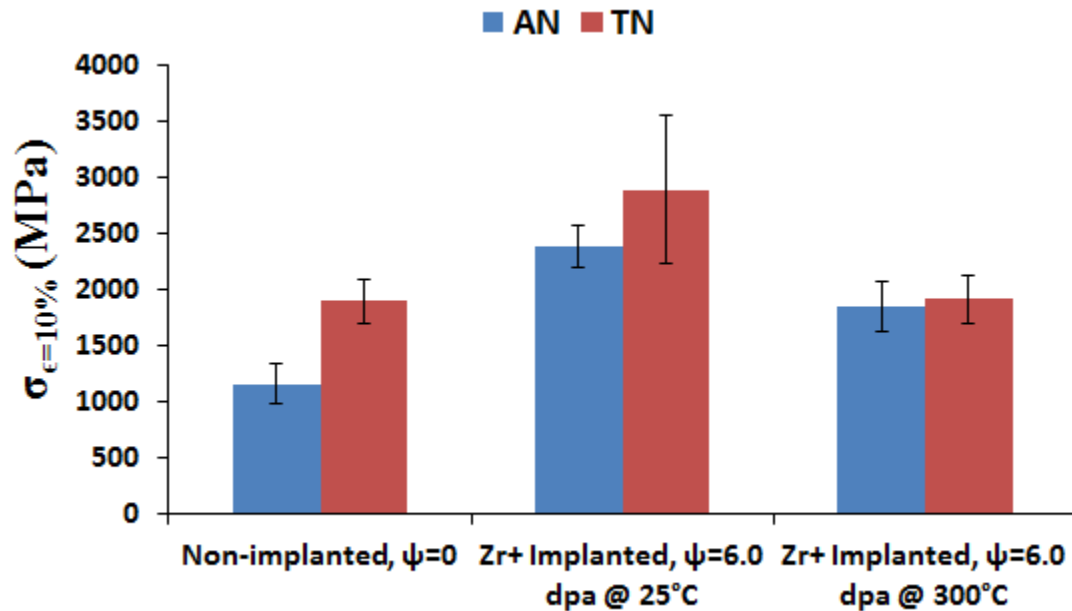


Figure 4.9: Histogram representation of the average flow stress ($\varepsilon = 10\%$) of the α_{Zr} micro-pillars.

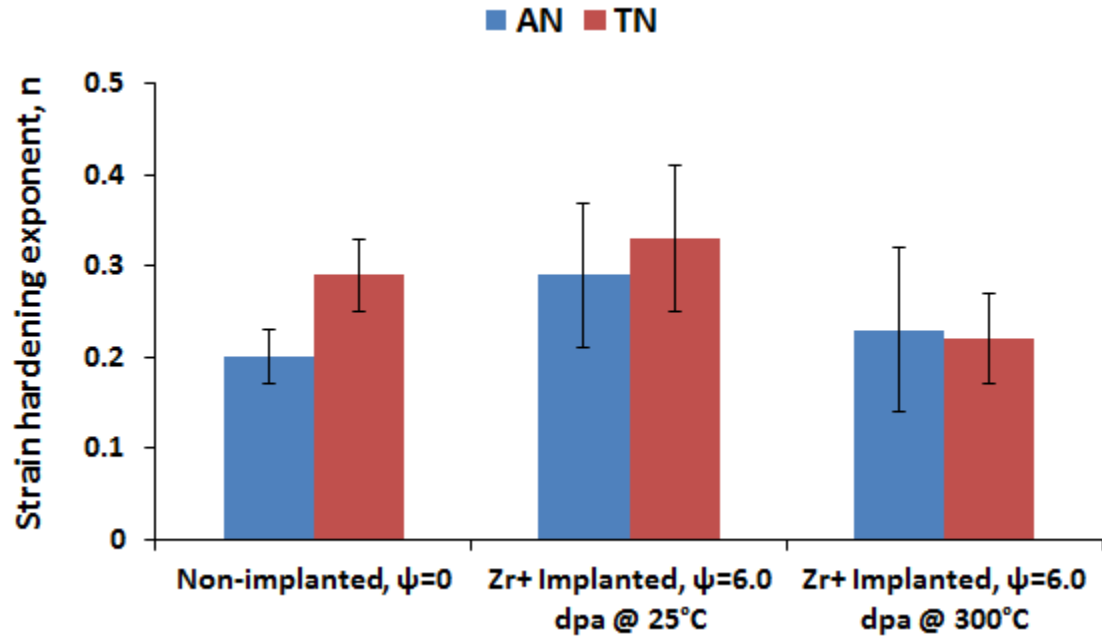
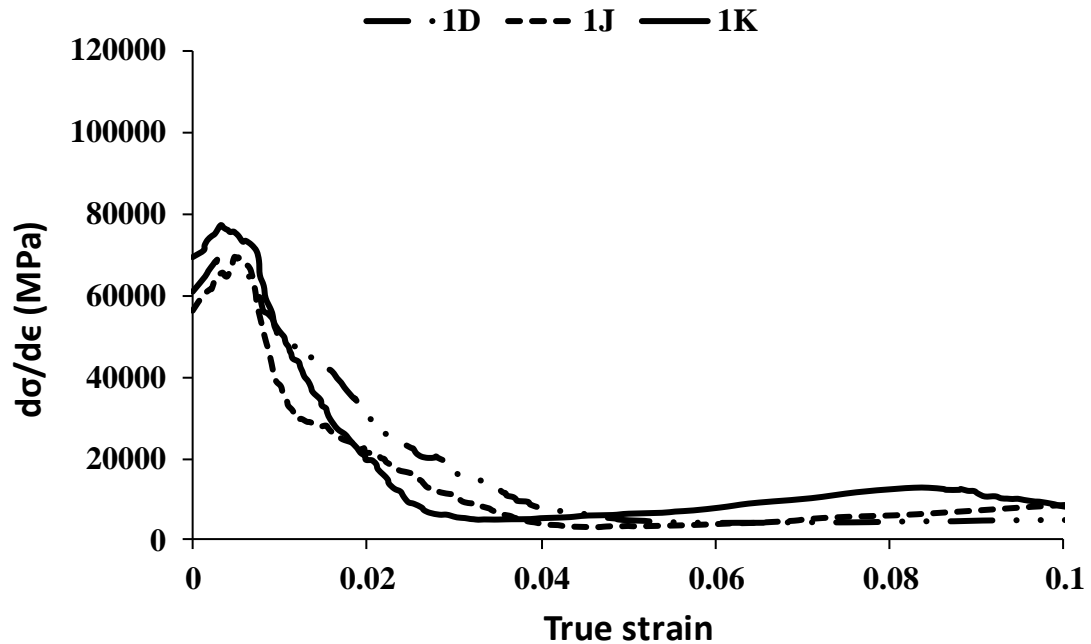


Figure 4.10: Histogram representation of the average strain-hardening exponent n of the α_{Zr} micro-pillars.



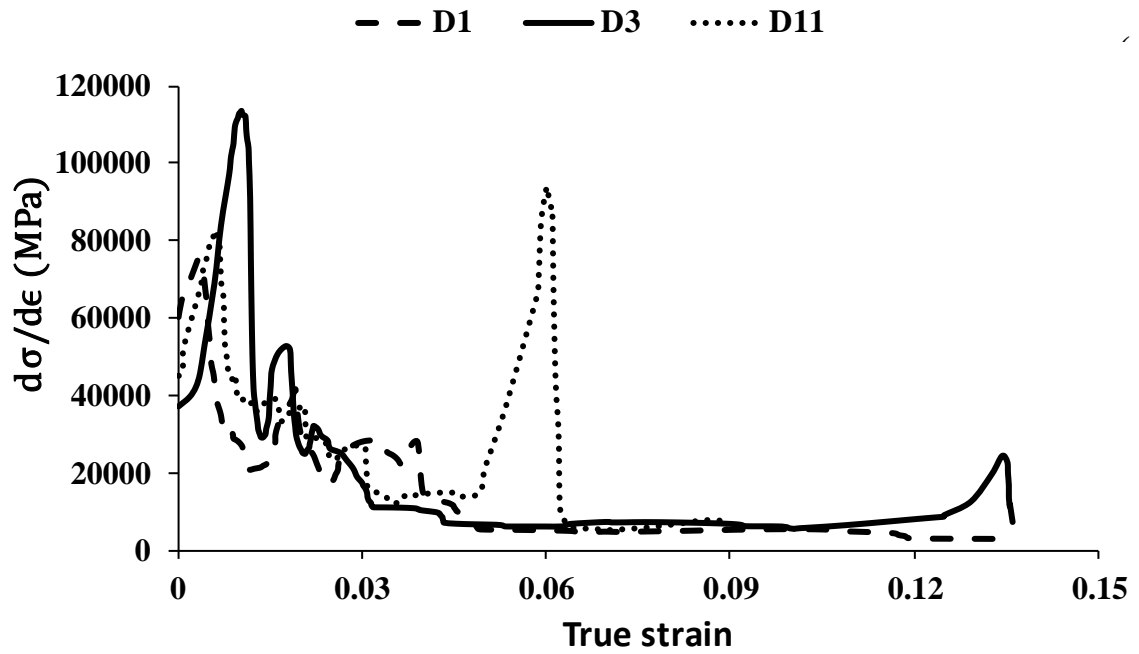
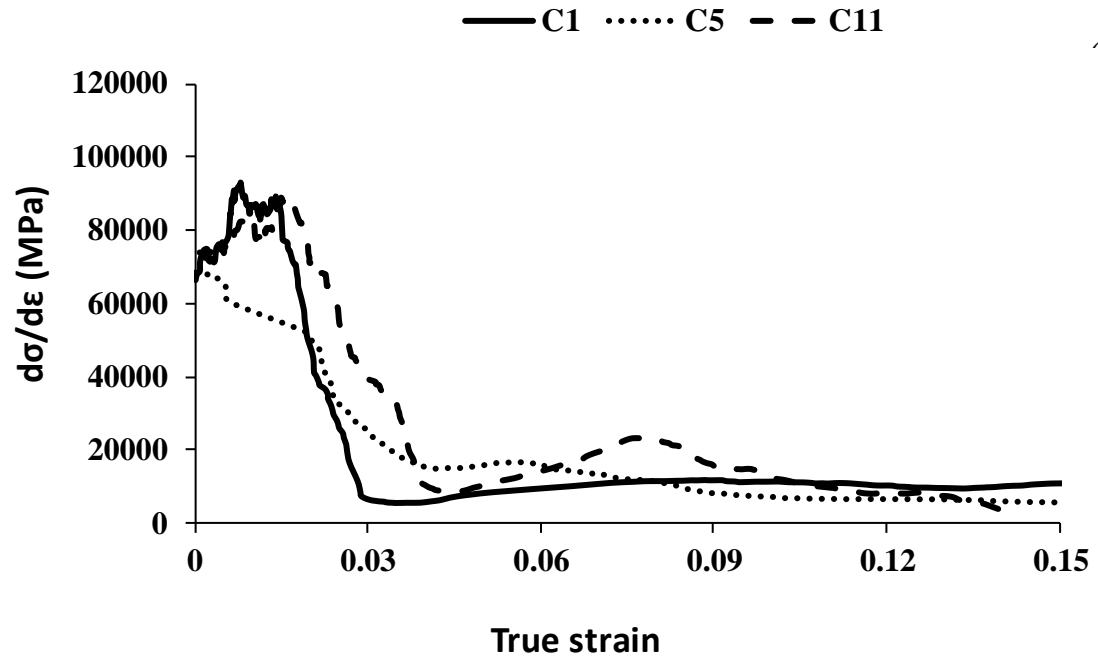


Figure 4.11: Strain hardening rate $d\sigma/d\varepsilon$ versus true strain for the α_{Zr} micropillars in the: (a) non-implanted, (b) Zr^+ -implanted (25°C), and (c) Zr^+ -implanted (300°C) conditions.

4.4.1 Length-scale dependence of the average flow stress

Figure 4.12 depicts $\sigma_{\varepsilon=10\%}$ as a function of pillar diameter for non-implanted Zr-2.5Nb micro-pillars. In this figure the data from the 5 μm and 2mm diameter pillars are from the publications of Oviasuyi et al. [15][16]. The plot indicates nonlinear decreasing flow stress with increasing pillar diameter and is typical to the size-dependence of the flow stress of most ductile metals [3][4]. The flow stress of the largest, 2 mm, diameter polycrystalline pillars is similar to that of bulk Zr-2.5%Nb pressure tube material.

Figure 4.12 also indicates that the flow stress anisotropy, $\sigma_{\text{TN}}/\sigma_{\text{AN}}$, also increases with decreasing pillar diameter. The large 2mm diameter polycrystalline micro-pillars displayed $\sigma_{\text{TN}}/\sigma_{\text{AN}} \approx 1.30$, while the 1 μm diameter single crystal α pillars display $\sigma_{\text{TN}}/\sigma_{\text{AN}} \approx 1.50$. The length-scale dependence of yield stress for uniaxially stressed specimens, free of local strain gradients, such as the micro-pillars tested in this study is usually attributed to a change in the deformation mechanism from one governed by obstacle-limited dislocation glide of pre-existing dislocations, for the large specimens, to one governed by the nucleation of new dislocation in otherwise defect-free material for small specimens [17]. In the following section we will assess the orientation dependence of the critical resolved shear flow stress of the 1 μm diameter pillars and its dependence upon Zr^+ ion implantation.

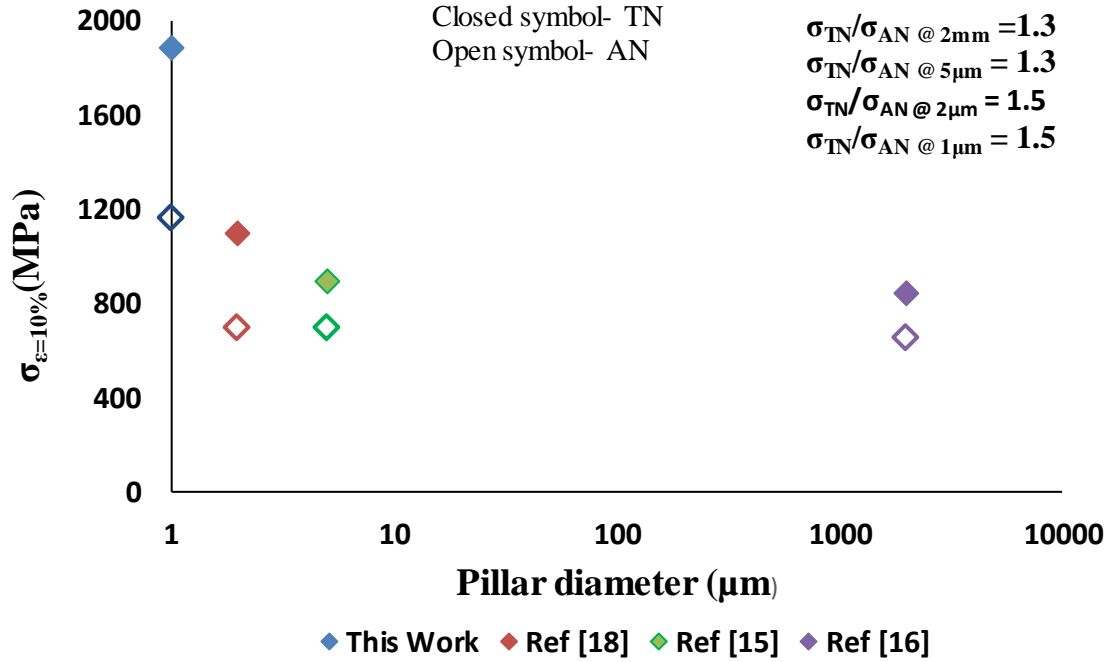


Figure 4.12: Average flow stress $\sigma_{\epsilon=10\%}$, plotted versus pillar diameter for AN and TN Zr-2.5%Nb pillars. The data for the 5 μm and 2 mm diameter polycrystalline pillars are from Ref [15] [16], 2 μm pillars are from Ref [18](these values were reported for $\sigma_{\epsilon=4\%}$).

4.4.2 Orientation dependence of the critical resolved shear stress

In this study we measured both the mechanical flow stress, $\sigma_{\epsilon=10\%}$, and the crystal orientation of the α -Zr micro-pillars. This allows us to determine the resolved shear stress corresponding to 10% axial strain $\tau_{\epsilon=10\%}$. The Schmid law formulation expresses $\tau_{\epsilon=10\%}$ as

$$\tau_{\epsilon=10\%} = m\sigma_{\epsilon=10\%} \quad (2)$$

Where the Schmid factor m is

$$m = \cos\phi\cos\lambda \quad (3)$$

and ϕ is the angle between the loading direction and the slip plane normal while λ is the angle between the loading direction and the slip direction. The maximum Schmid factor corresponding to deformation by each of the following mechanisms common to hcp crystals: $\{0001\}\langle 0001\rangle$ basal dislocation glide, $\{10\bar{1}0\}\langle 11\bar{2}0\rangle$ prismatic dislocation glide, $\{10\bar{1}1\}\langle 11\bar{2}3\rangle$ pyramidal dislocation glide, and $\{1\bar{1}02\}\langle 10\bar{1}1\rangle$ twinning deformation was calculated for each α -Zr micro-pillar (**Tables 2-4**). During single-slip, Stage II, deformation operating by a single deformation mechanism one would expect a constant $\tau_{\varepsilon=10\%}$, of magnitude characteristic of the operative mechanism, to be insensitive to loading direction. **Figure 4.13** shows the calculated $\tau_{\varepsilon=10\%}$ versus basal misorientation angle θ , defined as the angle between the loading direction and the $\langle 0001\rangle$, for each micro-pillars tested. While the magnitude of $\tau_{\varepsilon=10\%}$ is generally greater for the Zr^+ -implanted micro-pillars, the scatter in the data is large and thus shows no clear dependence upon θ . Examination of the data in **Tables 2-4** indicates that, in many cases, the Schmid factor is quite similar in magnitude for more than one deformation mechanism. It should also be noted that the values for critical resolved shear stress is also very close for basal and prismatic slip. The concurrent operation of multiple deformation mechanisms may give rise to the significant scatter in $\tau_{\varepsilon=10\%}$ shown in **Figure 4.13**. The occurrence of multiple slip during the compression of many of the α -Zr micro-pillars was also confirmed by post-test SEM imaging which indicated the occurrence of plastic deformation on multiple slip plane orientations (**Fig.4.5c**).

To remove the effect of concurrent operation of multiple slipsystems, only $\tau_{\varepsilon=10\%}$ data from micro-pillars that were strongly oriented for single slip or twinning were selected. The selected micro-pillars are highlighted in **Tables 2-4**. To remove the effect of Zr^+

implantation on $\tau_{\varepsilon=10\%}$, the selected data were normalized with respect to the resolved shear stress when $\theta = 0$ for each of the three ion-implantation conditions as

$$\hat{\tau}_{\varepsilon=10\%} = \frac{\tau_{\varepsilon=10\%}}{\tau_{\varepsilon=10\%}\theta=0} \quad (3)$$

Figure 4.14 shows $\hat{\tau}_{\varepsilon=10\%}$ versus θ . We observed that $\hat{\tau}_{\varepsilon=10\%}$ of these α_{Zr} micro-pillars is not constant but depends upon θ . While this is contrary to what one would expect for simple single-slip deformation, it is consistent with that predicted for deformation occurring by concurrent dislocation slip and twinning. This situation has been analyzed by Abdolvand et al [11] who demonstrate that twinning deformation can nucleate during dislocation glide plasticity of α_{Zr} and result in a dependence of $\hat{\tau}_{\varepsilon=10\%}$ upon θ , with a maximum $\hat{\tau}_{\varepsilon=10\%}$ at $\theta \approx 20^\circ$. This is quite close to what we observe in our study. The dependence of $\hat{\tau}_{\varepsilon=10\%}$ upon θ predicted by the model of Abdolvand et al is shown by the solid line in **Figure 4.14**.

4.4.3 Other sources contributing to variability in the $\hat{\tau}_{\varepsilon=10\%}$ - θ trend

The data points in Figure 4.14 are from favorably oriented α_{Zr} micro-pillars fabricated from either the TN or the AN planes of the Zr-2.5Nb pressure tube. Since the dimensions of the α_{Zr} grain in these tubes is highly elongated, and its average length in the axial direction is about 5 μm while its average length in the transvers direction is only about 1 μm , and despite the fact that the micro-pillars in this study were made only from very large α -Zr grains, the probability of making a 3 μm long truly single-crystal micro-pillar from the TN plane is lower than from the AN plane. Hence, the TN micro-pillars may contain a grain boundary, not apparent on the top, EBSD characterized, surface of the

pillar. The crystal misorientation resulting from such a grain boundary will of course result in scatter when $\hat{\tau}_{\varepsilon=10\%}$ is plotted versus θ . This is supported by the fact that, in **Figure 4.14**, the micro-pillars made from the TN plane of the pressure tube display the most scatter.

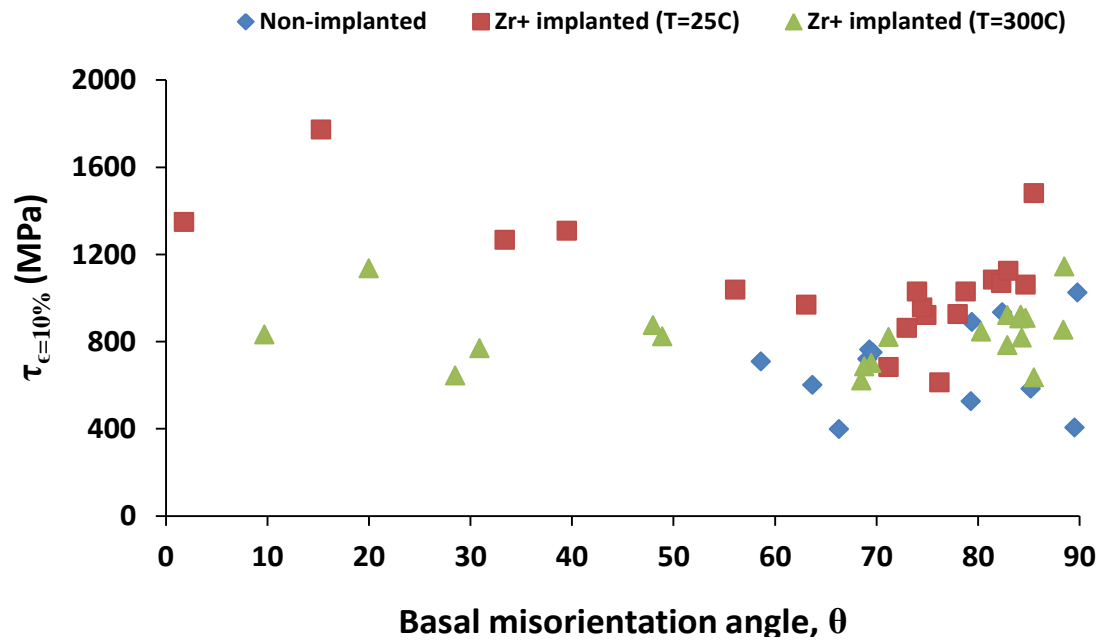


Figure 4.13: Calculated $\tau_{\varepsilon=10\%}$ (Eq. 2) versus basal misorientation angle θ for all the α -Zr micro-pillars tested in this study

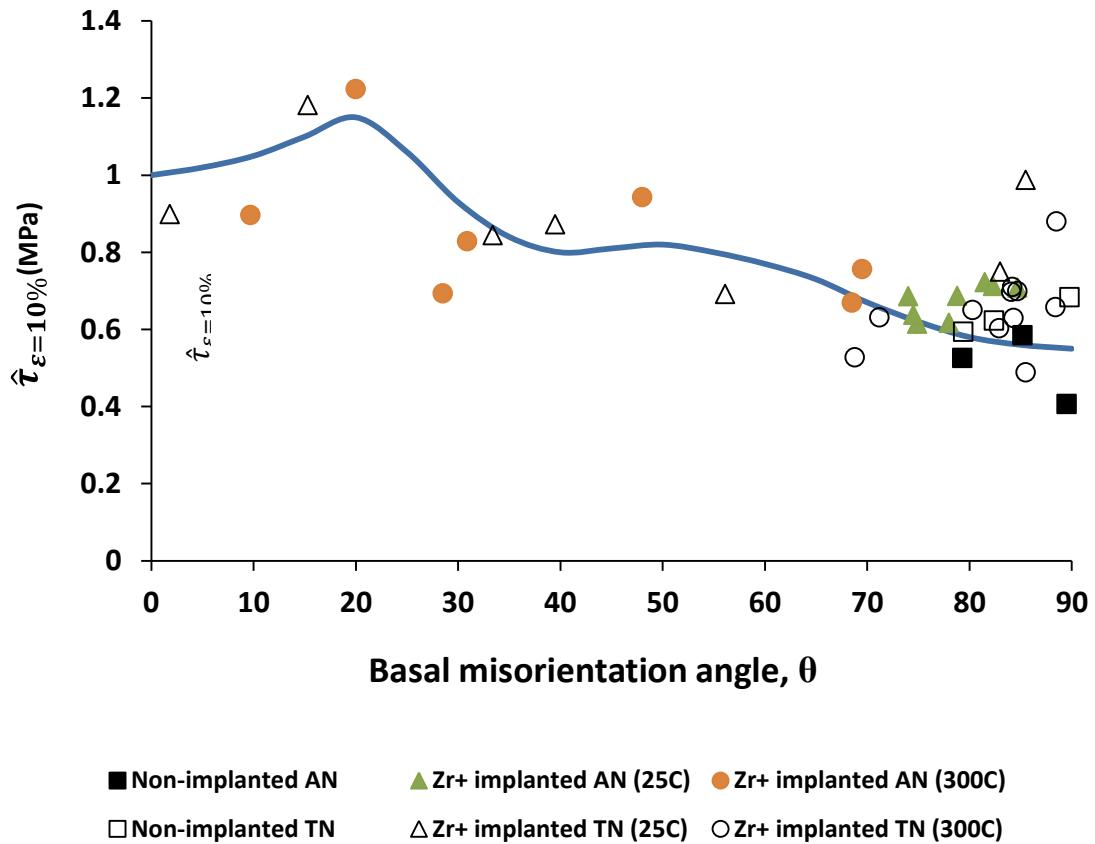


Figure 4.14 : Normalized resolved shear stress $\hat{\tau}_{\varepsilon=10\%}$ versus basal misorientation angle θ for α -Zr micro-pillars selected for strong single-slip or twinning. The data from micro-pillars fabricated from the TN and AN planes of the Zr-2.5Nb pressure tube are identified for each of the three Zr⁺ implantation conditions studied. The $\hat{\tau}_{\varepsilon=10\%}$ - θ trend predicted by the computational model of Abdolvand et al.[11] for deformation of hcp α -Zr via concurrent mechanisms of dislocation slip and twinning is shown by the solid line.

4.5 Conclusions

In this study we investigated the uniaxial flow stress of small, 1 μm diameter, single-crystal α -Zr micro-pillars made from the matrix phase of Zr-2.5%Nb pressure tube

material. The dependence of the normal flow stress $\sigma_{\varepsilon=10\%}$, resolved shear stress $\tau_{\varepsilon=10\%}$, and strain hardening exponent n upon Zr^+ implantation, specimen size, and crystal orientation were assessed.

In the non-implanted (as-received) condition, $\sigma_{\varepsilon=10\%}$ was significantly higher, about 70%, than that reported for larger diameter polycrystalline Zr-2.5%Nb pillars and followed a typical trend to that expected for the length-scale dependence of indentation hardness and flow stress of most ductile metals. We observed that the flow stress anisotropy ratio, σ_{TN}/σ_{AN} , displays a significant length-scale dependence suggesting that, for this strongly textured alloy, a stronger length-scale dependence occurs when the α_{Zr} pillars are loaded along the $\langle 0001 \rangle$ basal pole direction than along other directions.

The measured true stress-strain response of the α_{Zr} micro-pillars indicate that, while $\sigma_{\varepsilon=10\%}$ of the TN oriented pillars is consistently greater than that of the AN oriented pillars, Zr^+ implantation ($\bar{\psi} = 6.0dpa$) increased the flow stress of pillars of both orientations by about 60-80% when the implantation was performed at 25°C and 10-30% when implanted at 300°C. The measured strain-hardening rate n was not significantly affected by Zr^+ implantation however increasing the Zr^+ implantation temperature to 300°C resulted in increased tendency for irregular σ - ε flow response. This is consistent with the occurrence of increased thermally-activated implantation defect accumulation during Zr^+ implantation at 300°C compared to 25°C and is similar to what is observed in neutron-irradiated polycrystalline Zr-2.5%Nb.

The normalized shear stress $\hat{\tau}_{\varepsilon=10\%}$ of the α_{Zr} micro-pillars aligned for predominantly single-slip or twinning deformation, displayed a dependence upon crystal basal plane

orientation θ relative to the loading direction such that a maximum occurred when, $\theta \approx 20^\circ$. This is consistent with that predicted for deformation occurring by concurrent dislocation slip and twinning in α_{Zr} .

The experimental data presented in this paper contribute significantly not only to our understanding of the operative deformation mechanisms of small, micrometer-scale volumes of irradiation-hardened hcp metal, but also to our ability to predict the degree of local plasticity, contributed by the uniaxial elongation of unconstrained α -phase ligaments ahead of crack tips in commercial Zr-2.5%Nb pressure tubes.

4.6 Acknowledgements

The authors acknowledge the support of Dr. T. Simpson of the University of Western Ontario (UWO) Nanofabrication Laboratory for his assistance in preparing the micropillars and Mr. J. Hendriks of the UWO Tandetron Laboratory for his support in performing the Zr^+ implantations. The help of Mr. Ivan Barker and Prof. D. Moser of the UWO ZAP lab in the performance of the EBSD experiments is also acknowledged. The help of Prof. H. Abdolvand in calculating the Schmid factors and providing useful input discussions related to interpretation of the results is also gratefully acknowledged. Finally, we acknowledge the generous financial support of this research by the Candu Owners Group of Canada (<http://www.candu.org>).

References

- [1] N. Christodoulou, P. A. Turner, E. T. C. Ho, C. K. Chow, and M. R. Levi, "Anisotropy of Yielding in a Zr-2.5Nb Pressure Tube Material," *Met. Mat Trans*

- A, vol. 31, no. February, pp. 409–420, 2000.
- [2] D. D. Himbeault, C. K. Chow, and M. P. Puls, “Deformation behavior of irradiated Zr-25Nb pressure tube material,” *Metall. Trans. A, Phys. Metall. Mater. Sci.*, vol. 25, no. 1, pp. 135–145, 1994.
 - [3] J. R. Greer and J. T. M. De Hosson, “Plasticity in small-sized metallic systems: Intrinsic versus extrinsic size effect,” *Prog. Mater. Sci.*, vol. 56, no. 6, pp. 654–724, Aug. 2011.
 - [4] M. D. Uchic, D. M. Dimiduk, J. N. Florando, and W. D. Nix, “Sample dimensions influence strength and crystal plasticity,” *Science*, vol. 305, no. 5686, pp. 986–9, Aug. 2004.
 - [5] Q. Wang, F. Long, Z. Wang, N. Guo, and M. R. Daymond, “Orientation dependent evolution of plasticity of irradiated Zr-2.5Nb pressure tube alloy studied by nanoindentation and finite element modeling,” *J. Nucl. Mater.*, vol. 512, pp. 371–384, 2018.
 - [6] Q. Dong, H. Qin, Z. Yao, and M. R. Daymond, “Irradiation damage and hardening in pure Zr and Zr-Nb alloys at 573 K from self-ion irradiation,” *Mater. Des.*, vol. 161, pp. 147–159, 2019.
 - [7] A. Akhtar, “Compression of zirconium single crystals parallel to the c-axis,” *J. Nucl. Mater.*, vol. 47, no. 1, pp. 79–86, 1973.
 - [8] A. Akhtar and A. Teghtsoonian, “Plastic deformation of zirconium single crystals,” *Acta Metall.*, vol. 19, no. 7, pp. 655–663, 1971.
 - [9] A. Akhtar, “Prismatic slip in zirconium single crystals at elevated temperatures,” *Metall. Trans. A*, vol. 6, no. 6, pp. 1217–1222, 1975.
 - [10] M. Griffiths, “Microstructure evolution in h.c.p. metals during irradiation,” *Philos. Mag. A*, vol. 63, no. 5, pp. 835–847, May 1991.
 - [11] H. Abdolvand and M. R. Daymond, “Multi-scale modeling and experimental study of twin inception and propagation in hexagonal close-packed materials using a crystal plasticity finite element approach - Part I: Average behavior,” *J. Mech. Phys. Solids*, vol. 61, no. 3, pp. 783–802, 2013.
 - [12] R. E. Stoller, M. B. Toloczko, G. S. Was, A. G. Certain, S. Dwaraknath, and F. A. Garner, “On the use of SRIM for computing radiation damage exposure,” *Nucl. Instruments Methods Phys. Res. Sect. B Beam Interact. with Mater. Atoms*, vol. 310, pp. 75–80, Sep. 2013.
 - [13] M. Li, M. A. Kirk, P. M. Baldo, D. Xu, and B. D. Wirth, “Study of defect evolution by TEM with in situ ion irradiation and coordinated modeling,” *Philos. Mag.*, vol. 92, no. 16, pp. 2048–2078, 2012.

- [14] F. Onimus, I. Monnet, J. L. Béchade, C. Prioul, and P. Pilvin, “A statistical TEM investigation of dislocation channeling mechanism in neutron irradiated zirconium alloys,” *J. Nucl. Mater.*, vol. 328, no. 2–3, pp. 165–179, 2004.
- [15] R. O. Oviasuyi and R. J. Klassen, “Anisotropic deformation of Zr ion irradiated Zr–2.5%Nb micro-pillars at 25°C,” *J. Nucl. Mater.*, vol. 421, no. 1–3, pp. 54–57, Feb. 2012.
- [16] R. O. Oviasuyi and R. J. Klassen, “Assessment of the anisotropic flow stress and plastic strain of Zr–2.5%Nb pressure tubes at temperature from 25°C to 300°C,” *J. Nucl. Mater.*, vol. 429, no. 1–3, pp. 7–12, Oct. 2012.
- [17] J. R. Greer, W. C. Oliver, and W. D. Nix, “Size dependence of mechanical properties of gold at the micron scale in the absence of strain gradients,” *Acta Mater.*, vol. 53, no. 6, pp. 1821–1830, 2005.
- [18] Q. Wang, C. Cochrane, F. Long, H. Yu, and M. R. Daymond, “Micropillar compression study on heavy ion irradiated Zr-2.5Nb pressure tube alloy,” *J. Nucl. Mater.*, vol. 511, pp. 487–495, 2018.

Chapter 5

5 Effect of Zr⁺ implantation and crystal orientation on the uniaxial deformation of Zr-2.5%Nb micro-pillars: Part 2, Deformation of two-phase α_{Zr}/β_{Nb} micro-pillars

The uniaxial flow stress of 1 μm diameter Zr-2.5%Nb micro-pillars containing a microstructure of mixed α_{Zr} and β_{Nb} phases was assessed in the non-implanted condition and after Zr⁺ implantation to simulate neutron irradiation. Zr⁺ implantation ($\bar{\psi} \approx 6\text{dpa}$) performed at 300°C resulted in about 20% reduction in the flow stress $\bar{\sigma}_{(\varepsilon=0.10)}$ and displayed increased serrations in the σ - ε response. This suggests increased thermally activated recovery of the ion-induced crystallographic defect population when irradiation damage is invoked on the α/β microstructure at 300°C compared to at 25°C. The α_{Zr}/β_{Nb} micro-pillars that were Zr⁺-implanted at 300°C also display axial cracking during compression. This cracking was not observed during compression of non-implanted α_{Zr}/β_{Nb} micro-pillars nor was it observed on α_{Zr}/β_{Nb} micro-pillars that were Zr⁺ implanted at 25°C, which illustrates the role of thermal activation during Zr⁺ ion implantation in weakening α_{Zr}/β_{Nb} interfaces.

5.1 Introduction

Analysis of the ductile fracture of extruded and cold-drawn Zr-2.5%Nb pressure tubes, in CANDU nuclear reactors, indicates that hydride fracture in the crack tip region can result in formation of unconstrained ligaments extending between the fractured hydrides. These ligaments can be very small and have a microstructure consisting of monocrystalline α -Zr or simple α/β phase conjugates. Understanding the uniaxial stress-strain response of these ligaments both in the as-fabricated and the neutron-irradiated conditions is

imperative for making accurate prediction of the ductile fracture of in-service Zr-2.5%Nb pressure tube material. To accomplish this we need experimental data obtained by performing uniaxial deformation tests on small single crystal α -Zr or simple α/β phase samples, of size similar to the actual ligaments, cut from the actual Zr-2.5%Nb pressure tube material. In our adjoining paper we have reported the results of uniaxial compression tests performed on monocrystalline α -Zr micropillars (1 μm length scale) made from as-fabricated and Zr^+ -implanted Zr-2.5%Nb pressure tube material [3]. We characterized the dependence of the critical resolved shear stress and strain-hardening rate upon crystal orientation and Zr^+ implantation at two implantation temperatures, 25°C and 300°C, and observed that the magnitude and the anisotropy of the flow stress displays a significant length-scale dependence with a stronger length-scale dependence occurring when the micro-pillars are loaded along the $\langle 0001 \rangle$ basal pole direction. Zr^+ implantation at 300°C tends to result in an irregular σ - ε flow response consistent with increased tendency for strain localization. The normalized critical resolved shear stress of the α_{Zr} micro-pillars displayed a dependence upon crystal orientation that is consistent with deformation occurring by concurrent dislocation slip and twinning.

In this study we investigate the mechanical properties, under similar uniaxial compression conditions, of two-phase $\alpha_{\text{Zr}}/\beta_{\text{Nb}}$ micro-pillars to assess, by comparison with the previously reported data from α -phase micro-pillars, the influence of mixed $\alpha_{\text{Zr}}/\beta_{\text{Nb}}$ -phase microstructure on the local plastic deformation in both the as-fabricated condition and after Zr^+ implantation-induced crystal damage similar to that resulting from neutron

irradiation. The data we present here contributes significantly to our understanding of the operative deformation mechanisms of small, micrometer-scale volumes of irradiation-hardened material and thus to our ability to predict the local plasticity contributed by the co-deformation of α/β -phases in thin ligaments formed ahead of crack tips in Zr-2.5%Nb pressure tubes.

5.2 Procedure

Small rectangular samples, about 1 cm x 1 cm x 0.4 cm, were cut from a ring of as-fabricated, non-irradiated, Zr-2.5%Nb CANDU pressure tube. The orthogonal faces of the samples were labeled as Axial Normal (AN), Radial Normal (RN), and Transverse Normal (TN) with respect to the Axial, Radial, and Transverse directions of the tube. The sides of the samples were polished and chemically etched (Figure 5.1).

Areas of the microstructure containing clearly demarked α/β phase boundaries were selected for fabrication of micro-pillars by Focused Ion Beam (FIB) milling (Figure 5.1 **inset**). The micro-pillars were about 1 μm diameter and 3 μm height and were milled with a LEO Zeiss 1540 XB FIB SEM using with a 30 keV 10 nA Ga^+ beam. The tops of the pillars were further polished with low, 50 pA, Ga^+ beam current to minimize the depth of ion-induced crystal damage to facilitate subsequent EBSD analyses.

Figure 5.2 provides a schematic representation of the microstructure structure found in the $\alpha_{\text{Zr}}/\beta_{\text{Nb}}$ micro-pillars. The β_{Nb} phase consisted of thin, discontinuous filaments. One half of the micro-pillar was a continuous α -grain while the other half was a mixture of β_{Nb} regions within an α_{Zr} matrix (see red circle in the inset of Figure 5.1).

Electron Backscattered Diffraction (EBSD) analyses was performed, using a Hitachi SU6600 FEG-SEM equipped with an Oxford Instruments HKL EBSD detector/analysis system, on the top surface of each micro-pillar to determine the $\langle hklm \rangle$ orientation of the α -Zr phase corresponding to the axial pillar direction. It should be noted that the crystal orientation of the β -Nb filaments could not be measured due to their small size (thickness less than about $0.1 \mu\text{m}$).

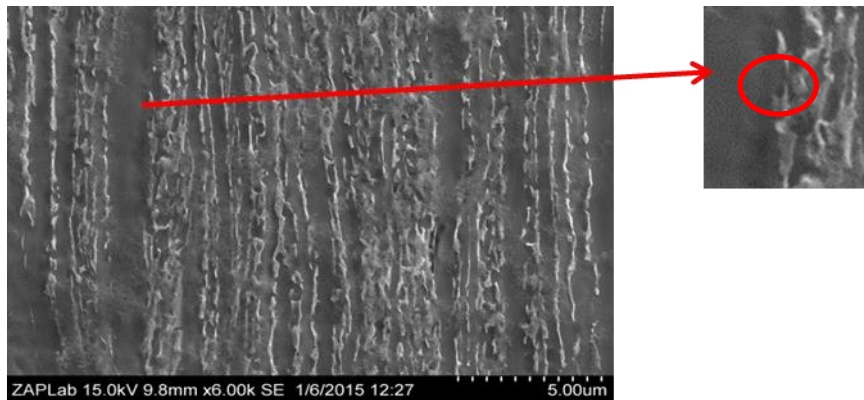


Figure 5.1: Microstructure, on the TN plane, of the extruded and cold-drawn Zr-2.5%Nb pressure tube. The red circle in the inset depicts an α/β region typical of that from which α/β micro-pillars were fabricated.

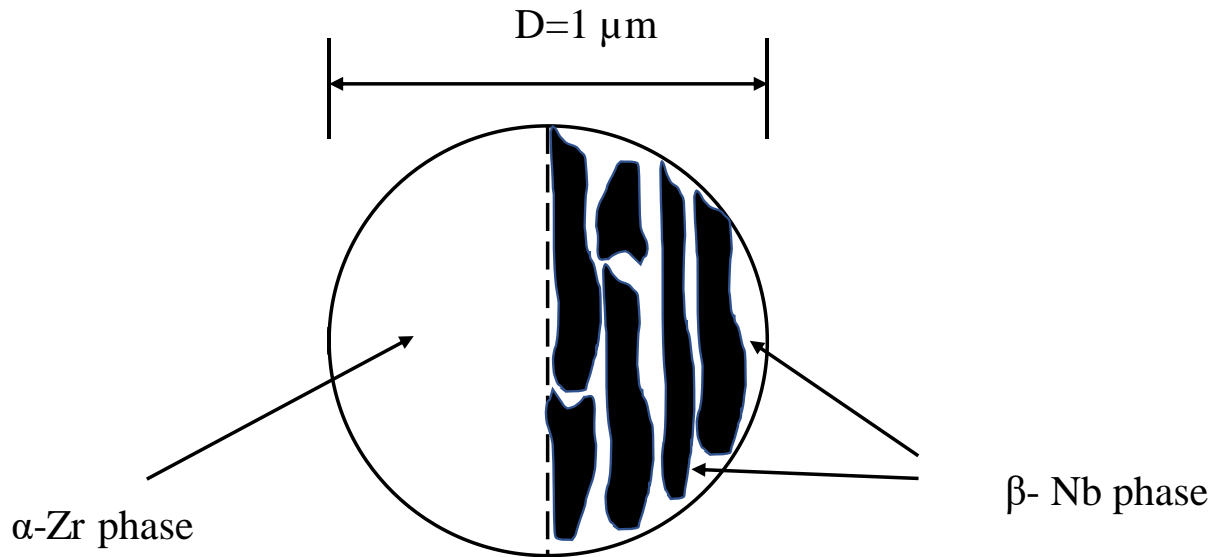


Figure 5.2: Schematic depiction of the typical microstructure found on the top surface of an α_{Zr}/β_{Nb} micro-pillar

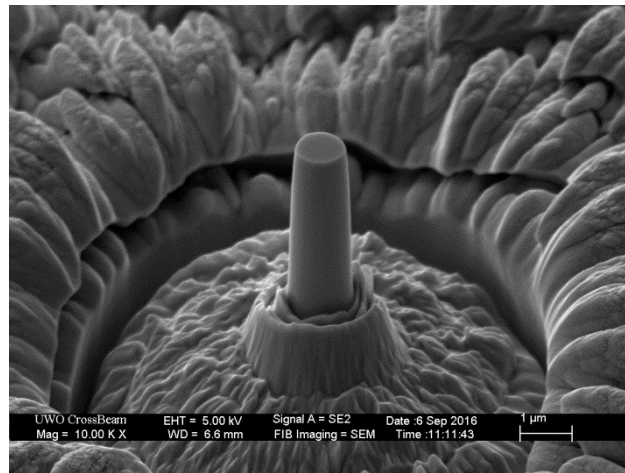


Figure 5.3: Typical FIB milled α_{Zr}/β_{Nb} micro-pillar made from the TN plane of a non-implanted Zr-2.5%Nb pressure tube

The micro-pillars were divided into two sets; non-implanted and Zr^{+} implanted. The implanted pillars were Zr^{+} implanted. The implanted pillars were exposed to 8.5 MeV Zr^{+} ($\varphi = 7.07 \times 10^{19}$ ions/m²) at either 25°C or 300°C using the Tandatron ion accelerator located at the University of Western Ontario (www.isw.physics.uwo.ca). This resulted in

peak Zr^{+} implantation depth of about 3 μm as calculated by SRIM software [1]. The average ion-induced atomic displacement, ψ , expressed in units of displacement per atom (dpa), was approximated using SRIM software and the Kinchin-Pease technique as [2]

$$\psi(dpa) = \frac{\varphi \times 10^8 \times \nu}{N} \quad (1)$$

where φ is the ion dose (ions/ m^2), ν is the calculated average number of atom displacements per ion and N is the atomic number density. The average damage level throughout the micropillar was about $\bar{\psi} \approx 6 dpa$.

The micro-pillars were then compressed at 25°C using a nano-indentation hardness tester equipped with a 10 μm diameter diamond flat punch. The compression tests were performed under constant loading rate of 0.10mN/sec to an axial true strain of about 15%. Forty-one α/β micro-pillars were tested in this study (**Table 5.1**).

Table 5.1: Listing of the micro-pillar compression tests performed.

Ion implantation condition	Pressure tube plane from which the micro-pillars were fabricated	Number of micro-pillars tested.	$\bar{\sigma}_{(\varepsilon=0.10)}$ (MPa)
Non-implanted	TN	8	2000±350
Zr^{+} Implanted ($\bar{\psi} \approx 6 dpa$ @ 25°C)	AN	6	2300±70
	TN	8	2900±300
Zr^{+} Implanted ($\bar{\psi} \approx 6 dpa$ @ 300°C)	AN	9	1700±200
	TN	10	1600±150
	Total number of micro-	41	

	pillars tested		
--	-----------------------	--	--

5.3 Results

Uniaxial compression true stress – true strain curves of the α_{Zr}/β_{Nb} micro-pillars are shown in **Figs. 5.4 -5.6**. The stress-strain response shows considerable variability for all test conditions. The average normal flow stress at 10% axial strain, $\bar{\sigma}_{(\varepsilon=0.10)}$, is given, along with the sample-to-sample scatter, in Table 5.1.

Results of EBSD analyses of the orientation of the α -Zr phase of each of the α/β micro-pillars is given in Table 5.2. These data are used, along with values of $\sigma_{(\varepsilon=0.10)}$, to approximate the critical resolved shear stress $\tau_{(\varepsilon=0.10)}$ for the deformation process at 10% axial strain (Section 5.4.2).

SEM images of typical deformed TN-oriented α/β micro-pillars for the non-implanted, Zr⁺-implanted at 25°C and Zr⁺-implanted at 300°C are shown in Figure 5.7. Axial cracking occurs along the α_{Zr}/β_{Nb} interface of micro-pillars that were Zr⁺-implanted at 300°C. This is discussed in Section 5.4.1.

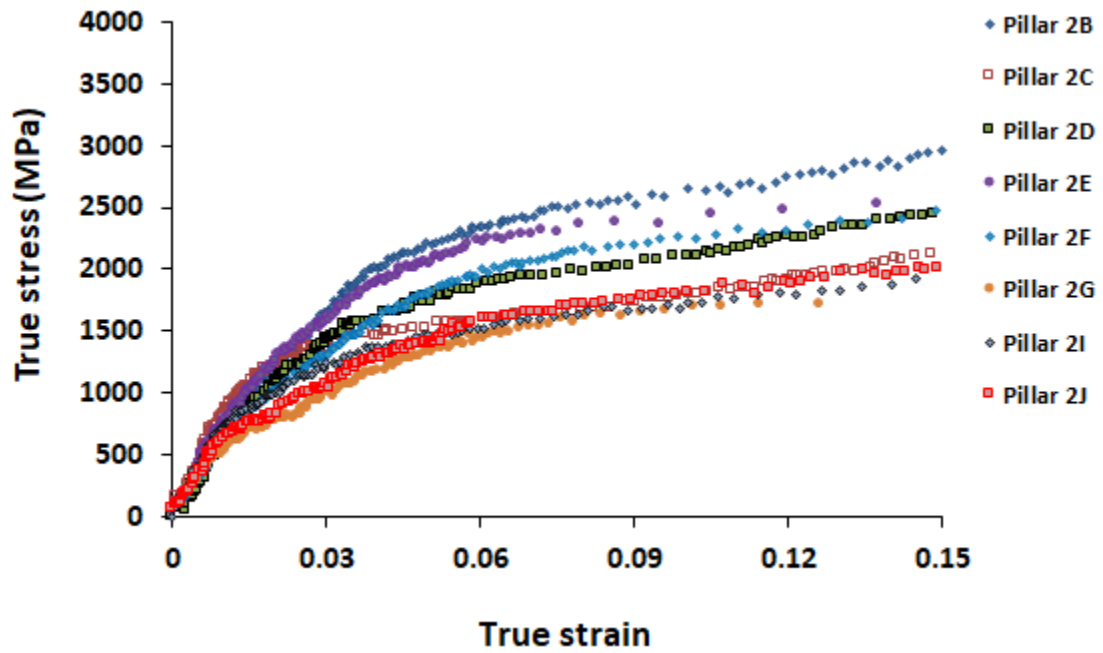
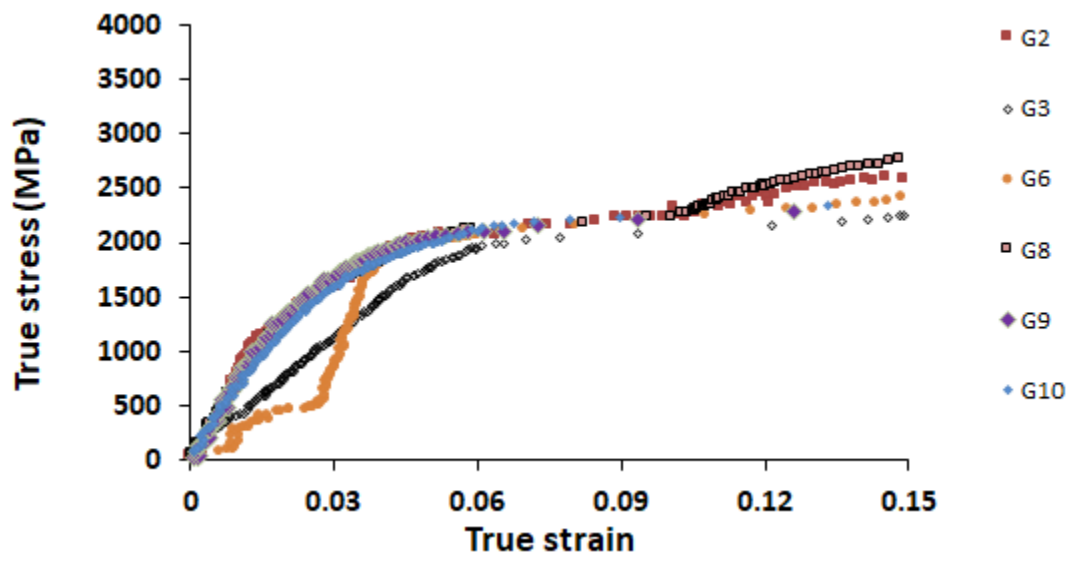
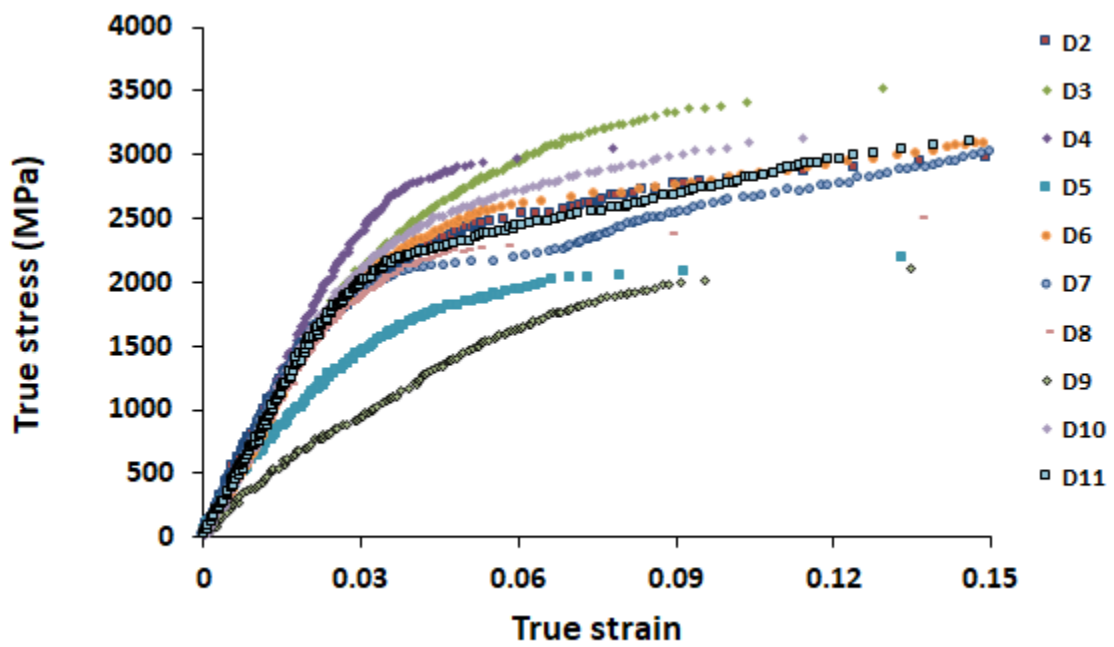


Figure 5.4: True stress versus true strain curves of the non-implanted TN micro-pillars.

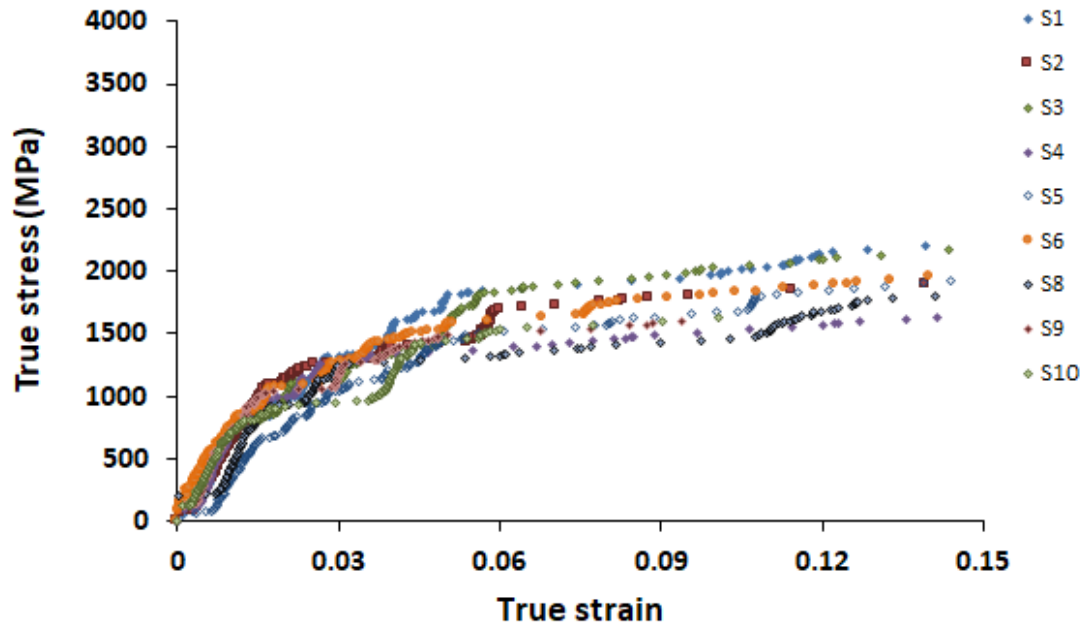


(a)

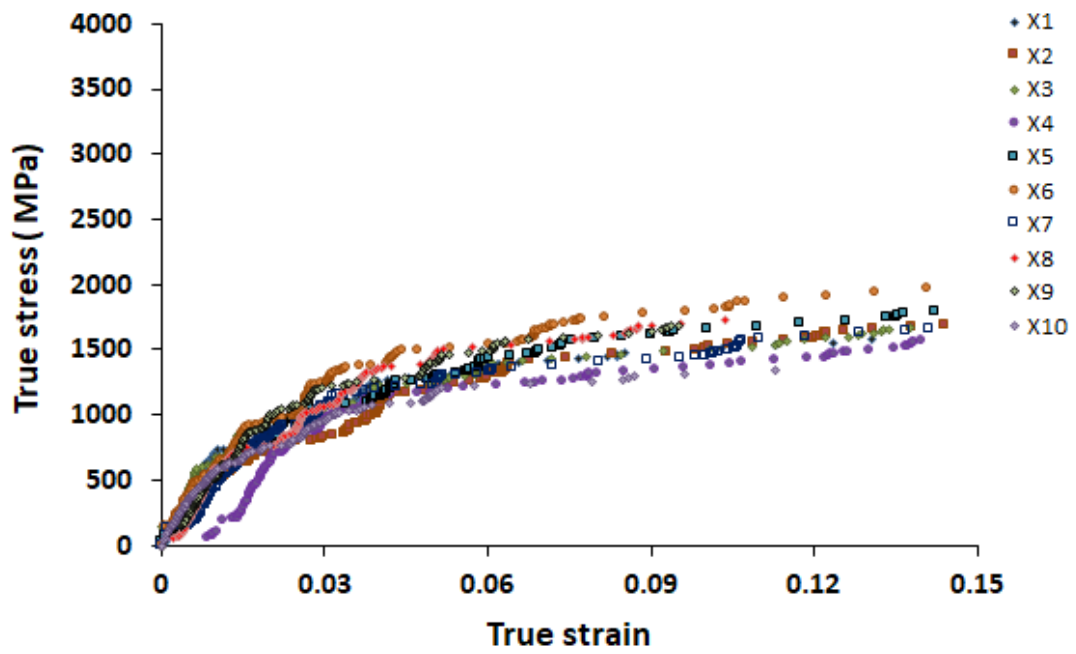


(b)

Figure 5.5: True stress versus true strain for the Zr^{+} -implanted ($\bar{\psi} \approx 6.0 \text{ dpa @ } 25^{\circ}C$) α/β -Zr micro-pillars fabricated from (a) the AN plane and (b) the TN plane of the Zr-2.5%Nb pressure tube.

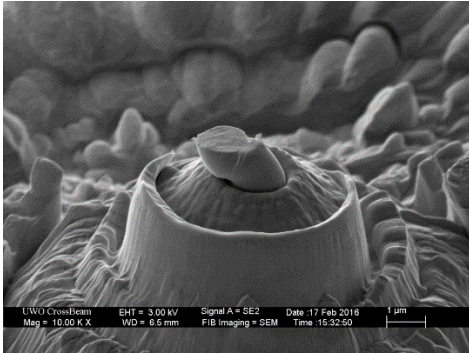


(a)

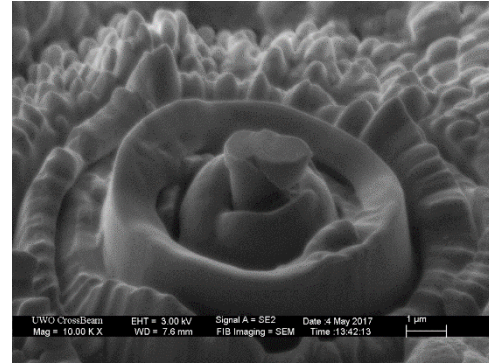


(b)

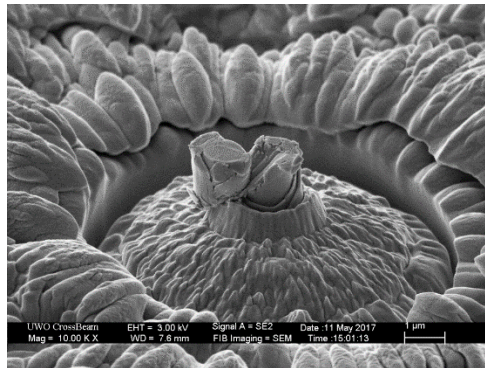
Figure 5.6: True stress versus true strain for the Zr^{+} -implanted ($\bar{\psi} \approx 6.0 \text{ dpa}$ @ 300°C) α/β -Zr micro-pillars fabricated from (a) the AN plane and (b) the TN plane of the Zr-2.5%Nb pressure tube.



(a)



(b)



(c)

Figure 5.7: TN-oriented α/β micro-pillars compressed at 25°C : (a) non-implanted, (b) Zr^{+} -implanted ($\bar{\psi} \approx 6 \text{ dpa}$) at 25°C , (c) Zr^{+} -implanted ($\bar{\psi} \approx 6 \text{ dpa}$) at 300°C .

Table 5.2: Approximate resolved shear stress ($\tau_{\varepsilon=0.10}$ Eq. 1), basal misorientation angle θ of the α -phase of each of the α_{Zr}/β_{Nb} micro-pillars.

Ion implantation condition	Pressure tube plane upon which micro-pillar was made	$\tau_{RSS}(MPa)$	Θ	Specimen designation		
Non-Implanted	TN	885	70.7	2B		
		852	10.2	2C		
		1039	20.3	2D		
		947	26.7	2E		
		1045	15	2F		
		796	74.9	2G		
		813	64.1	2I		
		850	53.7	2J		
		Zr⁺-Implanted ($\bar{\psi} \approx 6dpa @ 25^\circ C$)	TN	1247	42.3	D2
1600	28.6			D3		
1520	4.2			D4		
1399	5.3			D6		
1224	33.9			D7		
1213	28.2			D8		
1495	12.6			D10		
1381	3.5			D11		
AN	986		89.6	G2		
	749		57.8	G3		
	960		83.5	G6		
	782		82.2	G8		
	821		69.3	G9		
	1074		80	G10		
	Zr ⁺ -Implanted ($\bar{\psi} \approx 6dpa @ 300^\circ C$)		TN	642	87.4	X1
				641	85.6	X2
655		89.2		X3		
649		89.2		X4		
636		76.5		X5		
822		74.6		X6		
618		87.6		X7		
495		74.8		X8		
738		76.7		X9		
531		81.5		X10		

	AN	930	32.7	S1
		894	25.2	S2
		895	57.9	S3
		584	79.2	S4
		619	74.3	S5
		644	56.9	S6
		637	78.5	S8
		523	88.1	S9
		582	66.1	S10

5.4 Discussion

The objective of this study is to assess the uniaxial flow stress of α_{Zr}/β_{Nb} micro-pillars in the as-fabricated (non-implanted) condition and in two Zr^+ ion-implanted conditions such that the mechanical properties of similar-sized mixed α_{Zr}/β_{Nb} phase ligaments in the crack tip region of neutron irradiated Zr-2.5%Nb CANDU pressure tubes can be understood and predicted. Figure 5.8 shows a histogram of $\bar{\sigma}_{(\varepsilon=0.10)}$ for the α_{Zr}/β_{Nb} micro-pillars from this study in comparison to single crystal α_{Zr} micro-pillars in the non-implanted and the two Zr^+ implanted conditions [3].

5.4.1 Role of the α_{Zr}/β_{Nb} interface on the average micro-pillar flow stress

For all conditions the average flow stress $\bar{\sigma}_{(\varepsilon=0.10)}$ of the α_{Zr}/β_{Nb} micro-pillars is higher for the pillars made from the TN plane than from the AN plane of the Zr-2.5%Nb pressure tube. This anisotropy in $\bar{\sigma}_{(\varepsilon=0.10)}$ reflects the general transverse texture of the basal plane normal of the hcp α_{Zr} phase. Comparison of the $\bar{\sigma}_{(\varepsilon=0.10)}$ data for the TN α_{Zr}/β_{Nb} micro-pillars with that of the TN α_{Zr} micro-pillars indicates that $\bar{\sigma}_{(\varepsilon=0.10)}$ is of similar magnitude for both types of pillars when in the non-implanted condition. The

effect of Zr^{+} implantation on $\bar{\sigma}_{(\varepsilon=0.10)}$ is similar for the α/β and the α_{Zr} TN pillars in that in both cases $\bar{\sigma}_{(\varepsilon=0.10)}$ increases with Zr^{+} -implantation ($\bar{\psi} \approx 6dpa$) at 25°C however the percentage increase is slightly less (40% compared to 50%) for the α_{Zr}/β_{Nb} micro-pillars. Both types of micro-pillars display minimal, or no, increase in $\bar{\sigma}_{(\varepsilon=0.10)}$ when the Zr^{+} implantation is performed at 300°C. In fact, the α/β micro-pillars soften, on the average by 20%, compared to their non-implanted condition. The process of 300°C Zr^{+} implantation results in increased local fluctuations in the σ - ε flow curves obtained at 25°C. This is observed for both the α_{Zr}/β_{Nb} and the α_{Zr} micro-pillars. This is clearly illustrated when $\frac{d\sigma}{d\varepsilon}$ is plotted versus ε for the α_{Zr}/β_{Nb} micro-pillars (**Figure 5.9**). The magnitude of the $\frac{d\sigma}{d\varepsilon}$ fluctuations is greatest for the TN samples. The observed softening and increased stress fluctuations in the α_{Zr}/β_{Nb} and α_{Zr} micro-pillars after Zr^{+} implantation at 300°C, but not after Zr^{+} implantation at 25°C, suggests that thermally-activated recovery of the ion-induced crystallographic defect population being the cause. Our observation that this softening effect is greater in the α/β micro-pillars than in the α -Zr micro-pillars suggested that this recovery process occurs more quickly in the α/β interface regions.

The TN α_{Zr}/β_{Nb} micro-pillars that display softening when exposed to Zr^{+} -implantation at 300°C also display axial cracking along the central α_{Zr}/β_{Nb} interface during compression to high strain (**Fig 5.7c**). This cracking was not observed during compression of non-implanted TN α/β micro-pillars nor was it observed during compression of TN or AN

α_{Zr}/β_{Nb} micro-pillars that were Zr^+ implanted at 25°C and illustrate the role of thermal activation during high temperature Zr^+ implantation in weakening α_{Zr}/β_{Nb} interfaces.

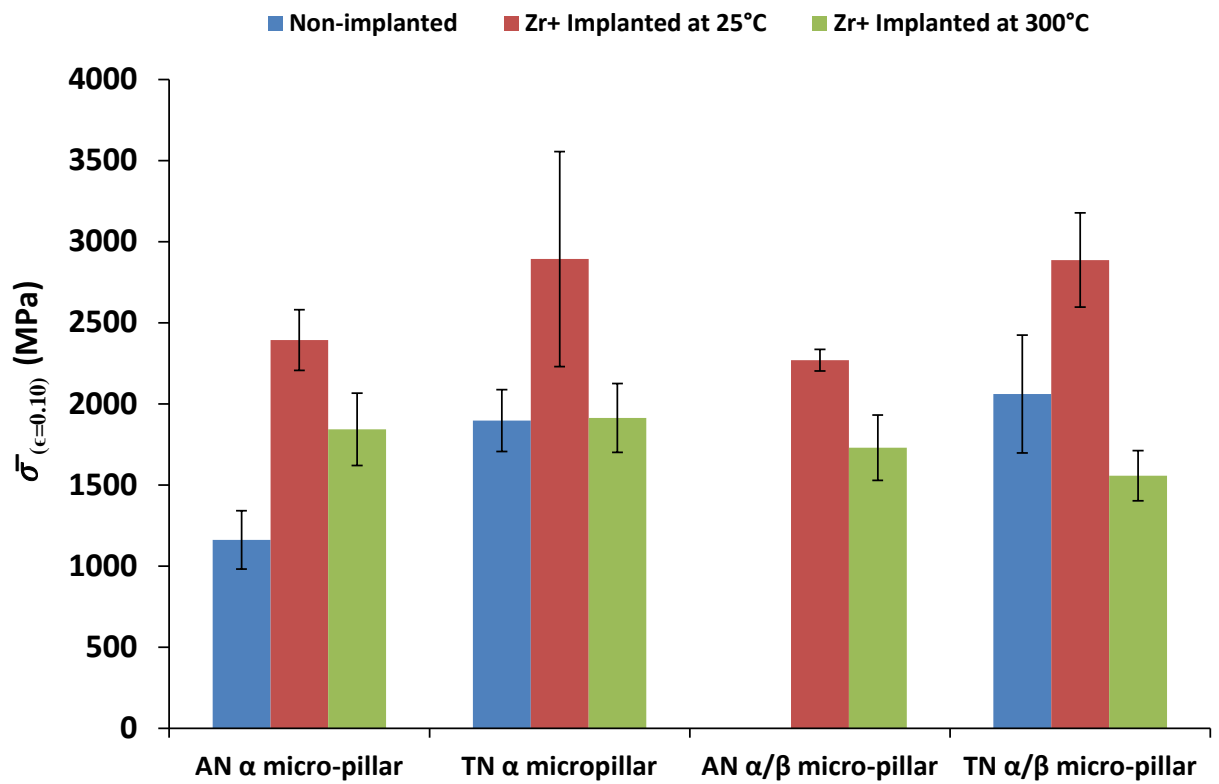
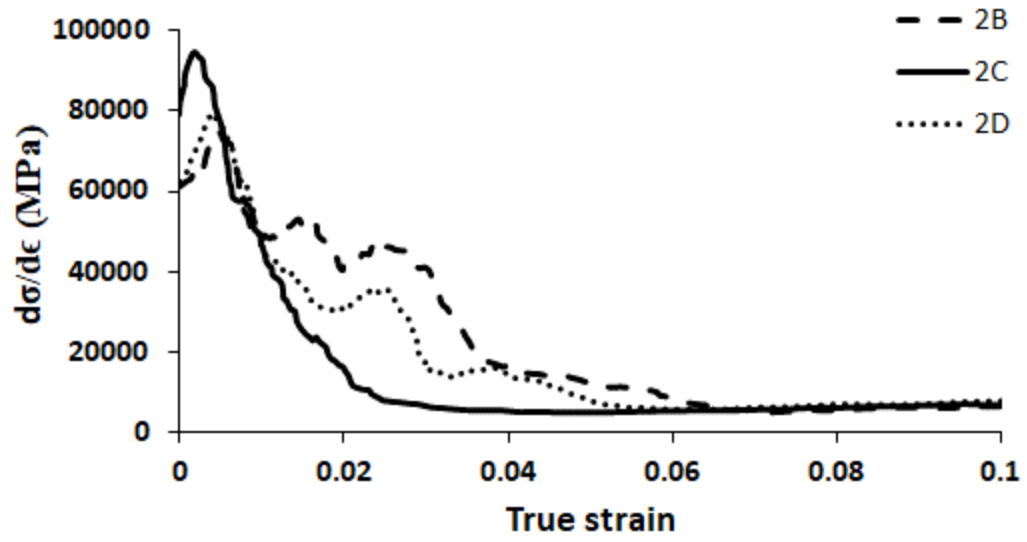
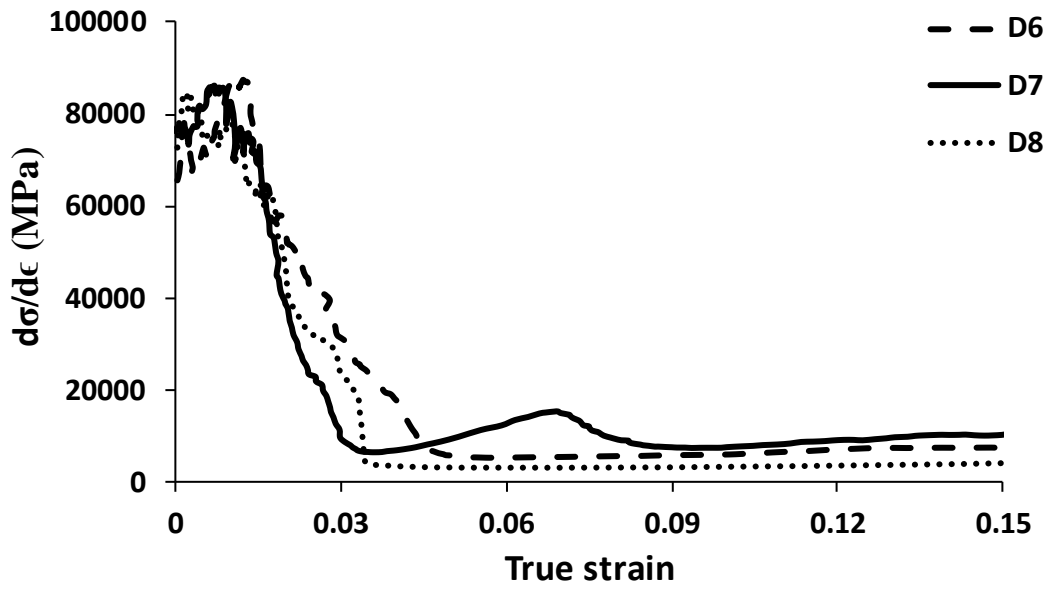


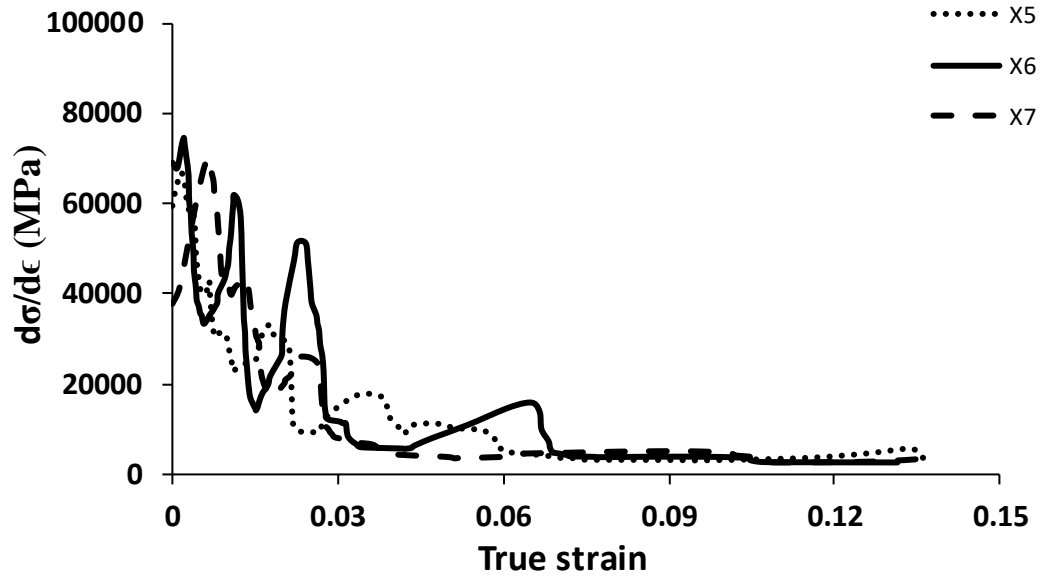
Figure 5.8: Effect of Zr^+ implantation on $\bar{\sigma}_{(\epsilon=0.10)}$ of the α/β micro-pillars and α_{Zr} micro-pillars [3] made from the AN and TN planes of a Zr-2.5%Nb pressure tube.



(a)



(b)



(c)

Figure 5.9: Plots of rate of change of flow stress with respect to strain, $\frac{d\sigma}{d\epsilon}$, versus true strain for TN α/β micro-pillars in: a) non-implanted condition, b) Zr^{+} implanted ($\bar{\psi} \approx 6dpa$) at 25°C, and c) Zr^{+} implanted ($\bar{\psi} \approx 6dpa$) at 300°C.

5.4.2 Orientation dependence of the critical resolved shear stress

The strength of a bicrystalline micro-pillar depends upon several factors such as: the orientation of the constituent phases and the volume occupied by each phase. Previous neutron diffraction studies have determined that the β -Nb phase has slightly higher yield stress and lower elastic modulus compared to the α -Zr phase ($\sigma_{y_{\beta-Nb}} \approx 480 MPa$, $E_{\beta-Nb} \approx 60 GPa$ while $\sigma_{y_{\alpha-Zr}} \approx 400 MPa$, $E_{\alpha-Zr} \approx 100 GPa$ [4]). Hence it can be assumed that the deformation in α/β bicrystal pillar would be activated first in the α -Zr phase. Ashton et al. [5] reported that for dual phase titanium alloys the orientation of the α phase relative to the β phase plays an important role in the micromechanical response of the alloy. The flow stress would be higher if the β phase

acts as barrier to mobile dislocations. As Zr-2.5%Nb has microstructural similarity with that of a dual α/β phase titanium alloy, the β -Zr could also have similar impact in micromechanical response. As reported in literature [6], [7], [8], [9], and [10] that the type of grain boundary would strongly affect the strength of bicrystal pillars.

Since we do not have information about the orientation of β -Nb phases in our micro-pillars, due to their small size making EBSD indexing impossible, we cannot calculate the precise angular misorientation between the α -Zr and β -Nb phases at the α/β boundaries. We can, however, obtain a first order approximation of the relative effect of α -Zr phase orientation on the critical resolve shear stress $\tau_{\varepsilon=0.10}$ of the α -phase within an α/β micro-pillar by assuming the crystallographic misorientation across all the α/β interfaces are the same and the volume fraction of the β -Nb filaments is small relative to that of the α -Zr phase. In such a condition, the measured $\bar{\sigma}_{(\varepsilon=0.10)}$ reflects, to a first approximation, the normal compressive stress in the α -Zr phase of the micro-pillar. We can then use the technique, described briefly below and in more detail in Ref. [3], to calculate $\tau_{\varepsilon=0.10}$

In this study both the mechanical flow stress, $\sigma_{\varepsilon=0.10}$, and the crystal orientation of the α -phase constituent of the α/β micro-pillars were measured. The Schmid law formulation expresses $\tau_{\varepsilon=0.10}$ as a function of $\sigma_{\varepsilon=0.10}$ as

$$\tau_{\varepsilon=0.10} = m\sigma_{\varepsilon=0.10} \quad (1)$$

Where the Schmid factor m is

$$m = \cos\phi\cos\lambda \quad (2)$$

and ϕ is the angle between the loading direction and the slip plane normal while λ is the angle between the loading direction and the slip direction. The maximum Schmid factor corresponding to deformation by each of the following mechanisms common to hcp crystals: $\{0001\}\langle 001 \rangle$ basal dislocation glide, $\{00\bar{1}0\}\langle 11\bar{2}0 \rangle$ prismatic dislocation glide, $\{10\bar{1}1\}\langle 11\bar{2}3 \rangle$ pyramidal dislocation glide, and $\{1\bar{1}02\} \langle 10\bar{1}1 \rangle$ twinning deformation was calculated (**Table 5.2**). During single-slip, Stage II, deformation one would expect a constant $\tau_{\varepsilon=0.10}$, of magnitude characteristic of the operative mechanism, to be insensitive to loading direction as indicated by the angle θ between the loading direction and the $\langle 0001 \rangle$ basal plane normal direction.

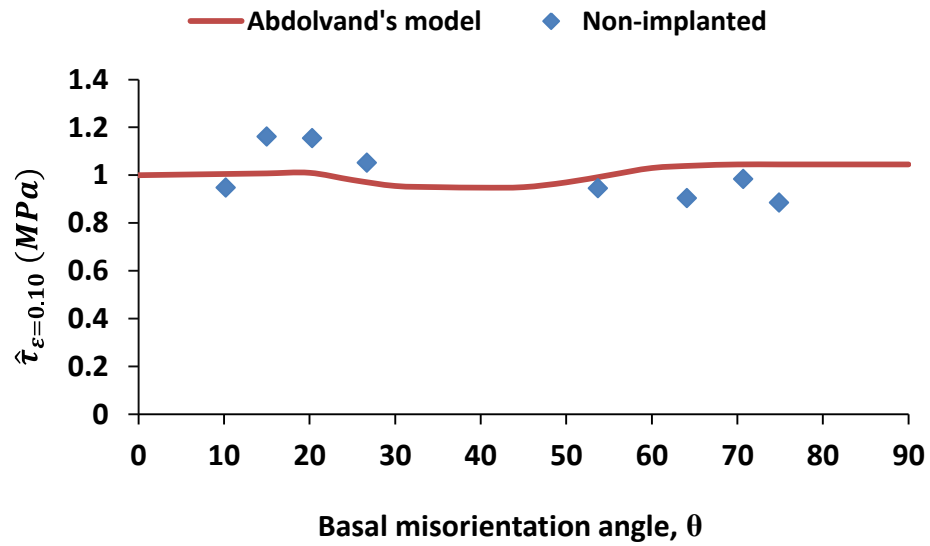
Figure 5.10 shows a plot of the normalized critical resolved shear stress expressed as

$$\hat{\tau}_{\varepsilon=0.10} = \frac{\tau_{\varepsilon=0.10}}{\tau_{\varepsilon=0.10\theta=0}} \quad (3)$$

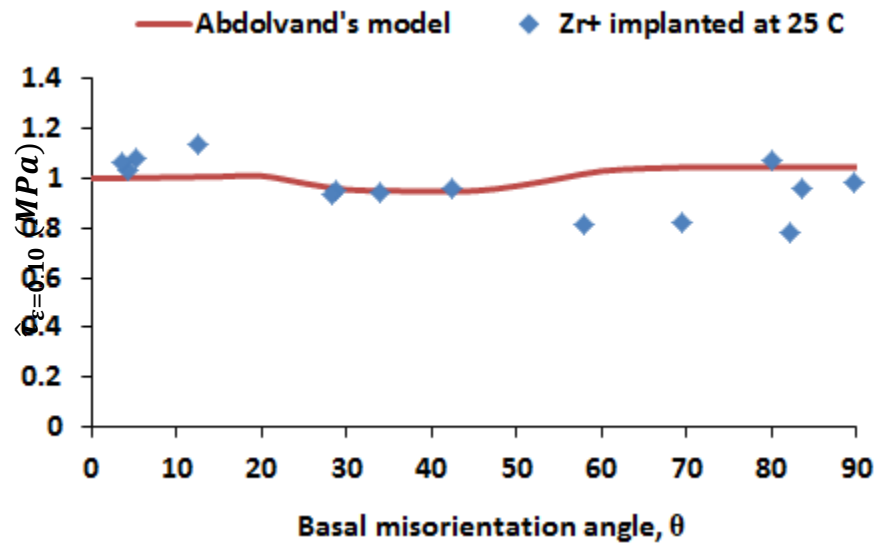
versus θ . We observed that $\hat{\tau}_{\varepsilon=0.10}$ of the α/β micro-pillars is not constant but depends upon θ . While this is contrary to what one would expect for single-crystal deformation by simple single-slip prismatic glide, it is consistent with that predicted for deformation occurring by concurrent dislocation slip and twinning.

We have compared our experimental results with a model proposed by Abdolvand et al. [11] to investigate the effects of grain boundary misorientation on twin inception during deformation of hcp bicrystals. Our experimental results match considerably well with the model of Abdolvand et al (**Fig. 5.10**). It should be noted that this model does not consider the effect of irradiation hardening and that our experiments includes α/β micro-

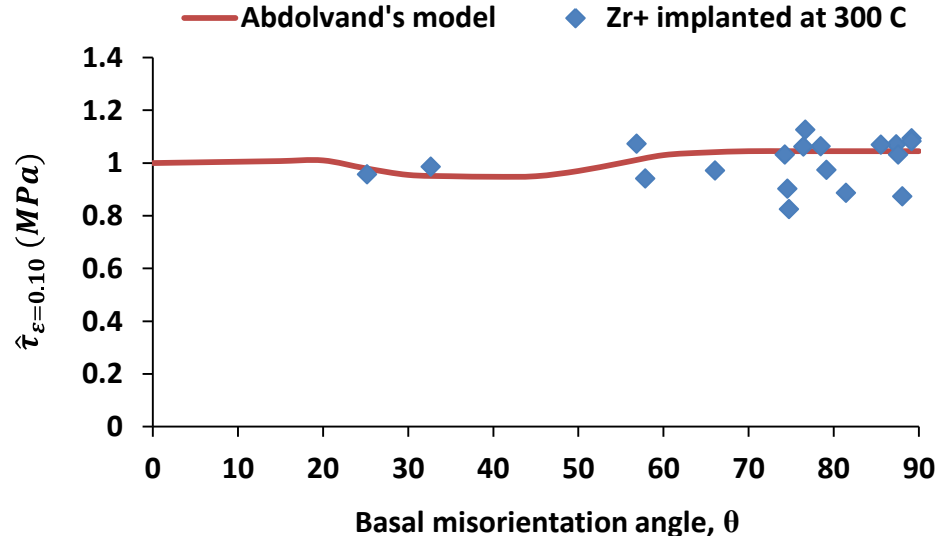
pillars with various thicknesses and volume fractions of β phase. Ashton et al. [5] reported that for dual phase titanium alloys, the variation of width of β phase and the relative crystallographic orientation of the α -phase with respect to β -phase orientation plays an important part in the stress-strain response of α/β colonies. For the samples that were Zr^+ implanted at $300^\circ C$ comparatively less variation in the $\hat{t}_{\varepsilon=0.10} - \theta$ trend (**Fig. 5.10**) and this may be the result of thermal energy rearranging the ion-induced crystal damage to promoted strain localization, through a dislocation channeling mechanism [12].



(a)



(b)



(c)

Figure 5.10: Variation in the normalized critical resolved shear stress $\hat{\tau}_{\varepsilon=0.10}$ (Eq. 3) with basal misorientation angle θ for α/β micro-pillars in the: a) non-implanted condition, b) Zr⁺ implanted ($\bar{\psi} \approx 6dpa$) at 25°C, and c) Zr⁺ implanted ($\bar{\psi} \approx 6dpa$) at 300°C. The solid line represents the trend predicted by the model of Abdolvand et al. [11]

5.5 Conclusions

In this study we have assessed the flow stress, at 25°C, of Zr-2.5%Nb micro-pillars containing a microstructure of mixed α -Zr and β -Nb phases in the non-implanted and in two Zr⁺-implanted ($\bar{\psi} \approx 6dpa$ at 25°C and 300°C) conditions. These tests were conducted to compare the mechanical response of α/β -phase ligaments with those of similar size α -phase ligaments, reported in Ref. 3, which occur at a crack tip during ductile fracture of neutron-irradiated Zr-2.5%Nb CANDU pressure tubes.

For all conditions tested, $\bar{\sigma}_{(\varepsilon=0.10)}$ is generally higher for the TN than for the AN oriented micro-pillars and this reflects the mechanical anisotropy of the hcp α -phase.

We observed that $\bar{\sigma}_{(\varepsilon=0.10)}$ is of similar magnitude for TN oriented α_{Zr}/β_{Nb} and α_{Zr} -phase micro-pillars in both the non-implanted and the Zr^+ implanted ($\bar{\psi} \approx 6dpa$ at $25^\circ C$) conditions and both types of micro-pillars displayed decreased $\bar{\sigma}_{(\varepsilon=0.10)}$, by about 20%, when the Zr^+ implantation was performed at $300^\circ C$. This softening effect is accompanied by increased local fluctuations in the σ - ε flow curves. These observations suggest that increased thermally-activated recovery of the Zr^+ -induced crystallographic defect population occurs when Zr^+ implantation is performed at an elevated temperature, $300^\circ C$ compared to $25^\circ C$. We observe that the degree of softening is greater in the α_{Zr}/β_{Nb} micro-pillars than in the α_{Zr} micro-pillars suggests that the recovery process occurs more quickly in the presence of α_{Zr}/β_{Nb} interfaces.

The TN α_{Zr}/β_{Nb} micro-pillars that display softening when exposed to Zr^+ -implantation at $300^\circ C$ also display axial cracking, occurring near the α_{Zr}/β_{Nb} interface region, during compression. This cracking was not observed during compression of non-implanted TN α_{Zr}/β_{Nb} micro-pillars nor was it observed during compression of TN or AN oriented α_{Zr}/β_{Nb} micro-pillars that were Zr^+ implanted at $25^\circ C$ and illustrates the role of thermal activation during Zr^+ ion implantation in weakening α_{Zr}/β_{Nb} interfaces.

We observed that concurrent operation of multiple deformation mechanisms gave rise to a normalized resolved critical shear stress $\hat{\tau}_{\varepsilon=0.10}$ which was not constant but varied with misorientation angle θ of the loading direction relative to $\langle 0001 \rangle$ of the α_{Zr} phase α_{Zr}/β_{Nb}

micro-pillar. The dependence of $\hat{\tau}_{\varepsilon=0.10}$ upon θ matched well with the computational results of Abdolvand et al [11] for deformation in bicrystalline α_{Zr} by multiple mechanisms involving twin inception, from grain boundaries, along with dislocation slip. For the samples that were Zr^+ implanted at 300°C comparatively less variation in the $\hat{\tau}_{\varepsilon=0.10} - \theta$ trend was observed and this may be the result of enhanced thermally-induced recovery of Zr^+ -induced crystal damage to promoted strain localization, through a dislocation channeling mechanism, in the region of the α_{Zr}/β_{Nb} interfaces.

5.6 Acknowledgements

The authors acknowledge the support of Dr. T. Simpson of the University of Western Ontario (UWO) Nanofabrication Laboratory for his assistance in preparing the micro-pillars and Mr. J. Hendriks of the UWO Tandetron Laboratory for his support in performing the Zr^+ implantations. The help of Mr. Ivan Barker and Prof. D. Moser of the UWO ZAP lab in the performance of the EBSD experiments is also gratefully acknowledged. The help of Prof. H. Abdolvand in calculating the Schmid factors and providing useful input discussions related to interpretation of the results is also gratefully acknowledged. Finally, we acknowledge the generous financial support of this research by the CANDU Owners Group of Canada (<http://www.candu.org>).

References

- [1] R. E. Stoller, M. B. Toloczko, G. S. Was, A. G. Certain, S. Dwaraknath, and F. A. Garner, “On the use of SRIM for computing radiation damage exposure,” *Nucl. Instruments Methods Phys. Res.*, vol. 310, no. September, pp. 75–80, 2013.
- [2] M. Li, M. A. Kirk, P. M. Baldo, D. Xu, and B. D. Wirth, “Study of defect evolution by TEM with in situ ion irradiation and coordinated modeling,” *Philos. Mag.*, vol. 92, no. 16, pp. 2048–2078, 2012.
- [3] M. I. Khan and R. J. Klassen, “Effect of Zr⁺ implantation and crystal orientation on the uniaxial deformation of Zr-2.5%Nb micro-pillars: Part 1, Deformation of single-phase α -Zr micro-pillars,” *Can. Metall. Q.*
- [4] S. Cai, M. R. Daymond, and R. A. Holt, “Modeling the room temperature deformation of a two-phase zirconium alloy,” *Acta Mater.*, vol. 57, no. 2, pp. 407–419, 2009.
- [5] P. J. Ashton, T. S. Jun, Z. Zhang, T. B. Britton, A. M. Harte, S. B. Leen, and F. P. E. Dunne, “The effect of the beta phase on the micromechanical response of dual-phase titanium alloys,” *Int. J. Fatigue*, vol. 100, pp. 377–387, 2017.
- [6] N. Kheradmand, H. Vehoff, and A. Barnoush, “An insight into the role of the grain boundary in plastic deformation by means of a bicrystalline pillar compression test and atomistic simulation,” *Acta Mater.*, vol. 61, no. 19, pp. 7454–7465, 2013.
- [7] K. S. Ng and A. H. W. Ngan, “Deformation of micron-sized aluminium bi-crystal pillars,” *Philos. Mag.*, vol. 89, no. 33, pp. 3013–3026, 2009.
- [8] P. J. Imrich, C. Kirchlechner, C. Motz, and G. Dehm, “Differences in deformation behavior of bicrystalline Cu micropillars containing a twin boundary or a large-angle grain boundary,” *Acta Mater.*, vol. 73, pp. 240–250, Jul. 2014.
- [9] I. Tiba, T. Richeton, C. Motz, H. Vehoff, and S. Berbenni, “Incompatibility stresses at grain boundaries in Ni bicrystalline micropillars analyzed by an anisotropic model and slip activity,” *Acta Mater.*, vol. 83, pp. 227–238, 2015.
- [10] C. S. Kaira, S. S. Singh, A. Kirubanandham, and N. Chawla, “Microscale deformation behavior of bicrystal boundaries in pure tin (Sn) using micropillar compression,” *Acta Mater.*, vol. 120, pp. 56–67, 2016.
- [11] H. Abdolvand and M. R. Daymond, “Multi-scale modeling and experimental study of twin inception and propagation in hexagonal close-packed materials using a crystal plasticity finite element approach - Part I: Average behavior,” *J. Mech. Phys. Solids*, vol. 61, no. 3, pp. 783–802, 2013.
- [12] F. Onimus, I. Monnet, J. L. Béchade, C. Prioul, and P. Pilvin, “A statistical TEM investigation of dislocation channeling mechanism in neutron irradiated zirconium

alloys," *J. Nucl. Mater.*, vol. 328, no. 2–3, pp. 165–179, 2004.

Chapter 6

6 Deformation of Zr⁺ implanted Zr-2.5%Nb alloy at 250°C

Uniaxial compression tests were performed at 250°C on non-implanted and Zr⁺ implanted ($\bar{\psi} \approx 6dpa @ 300^\circ C$) Zr-2.5%Nb α_{Zr} and α_{Zr}/β_{Nb} -phase micro-pillars (1 μm diameter and 3 μm height) to assess the effect of testing temperature on the normal yield stress, critical resolved yield shear stress, and strain hardening capacity. Surface cracking and increased serration of the stress – strain response, was observed for the Zr⁺ implanted micro-pillars indicating that Zr⁺-induced crystal damage either mobilizes or enhances oxygen-induced embrittlement through a dynamic strain-aging at 250°C in air. The anisotropy factor, $\sigma_{0.2\%TN}/\sigma_{0.2\%AN}$, of non-implanted α_{Zr} -phase micro-pillars decreased from about 1.5 to 0.9 with increasing testing temperature from 25°C to 250°C but remained essentially unchanged at about 0.9 for the Zr⁺ implanted micro-pillars. All micro-pillar conditions tested displayed reduced strain hardening capacity at 250°C compared to 25°C. All the non-implanted α_{Zr} -phase micro-pillars, regardless of crystal orientation, and specific Zr⁺ implanted micro-pillars, aligned for preferential basal dislocation glide, displayed decreasing normalized resolved flow shear stress $\hat{\tau}$ with increasing temperature from 25°C to 250°C consistent with increased thermal activation of obstacle-limited dislocation glide. In contrast, Zr⁺ implanted micro-pillars aligned for preferred prismatic dislocation slip displayed increasing $\hat{\tau}$ with increasing testing temperature indicating that the implantation process, followed by prolonged exposure to air at 250°C during testing, results in creation of stronger obstacles to prismatic dislocation glide.

6.1 Introduction

Zirconium alloys are widely used for structural components of nuclear reactor cores due to their low neutron absorption cross-section, good mechanical properties, and high corrosion resistance. One example of this is the Zr-2.5Nb alloy which is used for heavy water primary coolant pressure tubes in CANDU nuclear reactors. These tubes normally operate at temperature between 250 and 300°C [1]. The mechanical strength and ductility of this alloy has been studied extensively with large specimen testing [1][2][3][4] and with micro-/nano-indentation hardness and micro-pillar compression tests [5][6][7][8][9]. The mechanical strength of this material is anisotropic due to the elongated shape and crystallographic texture of its hcp α_{Zr} -phase matrix. In the as-fabricated condition its yield stress is about 20% higher when loaded in the circumferential (transverse) direction of the pressure tube than when loaded in the axial direction [8]. Neutron irradiation induces significantly hardening to this alloy and appears to reduce the extent of its mechanical anisotropy [9]. The bulk of previous investigations into the nature of this irradiation – induced hardening were conducted with nano-indentation hardness or micro-pillar compression tests performed on material that was Zr^+ implanted to impart similar levels of microstructural damage as neutron irradiation. In our previous papers the mechanical strength and ductility at 25°C of Zr^+ implanted and non-implanted α_{Zr} and α_{Zr}/β_{Nb} phase micro-pillars of Zr-2.5Nb pressure tube material were investigated [10][11]. Zr^+ implantation ($\bar{\psi} \approx 6dpa$) increased the flow strength for α_{Zr} and α_{Zr}/β_{Nb} micro-pillars fabricated along the axial and transverse directions of the pressure tube but flow strength was significantly reduced when the Zr^+ implantation temperature was increased from 25°C to 300°C. The presence of an interface in the micro-pillar resulted in lower

flow strength compared to single crystal α -phase micro-pillars. This was attributed to the α_{Zr}/β_{Nb} interface acting as a dislocation sink [12].

Since the micro-pillar mechanical testing described above was performed at only one temperature, 25°C, it is important that similar tests be performed at ion-implantation and mechanical test temperature that is within the 250-300°C operating temperature range of CANDU pressure tubes to confirm that the reported deformation effects and mechanisms are representative of what occurs in Zr-2.5Nb pressure tubing during service in a CANDU reactor. In this paper we present data on the effect of Zr⁺ implantation, performed at 300°C, on the magnitude and anisotropy of the yield stress and strain hardening capacity at 250°C, of α_{Zr} and α_{Zr}/β_{Nb} - phase micro-pillars made of Zr-2.5Nb pressure tube material.

6.2 Procedure

Small rectangular samples, about 1 cm x 1 cm x 0.4 cm, were cut from a non-irradiated extruded and 25% cold-drawn Zr-2.5%Nb CANDU pressure tube. Two orthogonal faces of the samples were labeled as Axial Normal (AN) and Transverse Normal (TN) with respect to the Axial, and Transverse (circumferential) directions of the tube. The AN and TN sides of the samples were polished and chemically etched to reveal the α_{Zr} and β_{Nb} phase microstructure. Areas of the microstructure, on the AN and TN sides, containing comparatively large α grains were selected for fabrication of single crystal α_{Zr} phase micro-pillars while clearly demarked α_{Zr}/β_{Nb} phase boundaries were selected for fabrication of α_{Zr}/β_{Nb} micro-pillars.

The micro-pillars, about 1 μm diameter and 3 μm height (Figure 6.1), were fabricated by Focused Ion Beam (FIB) milling with a 30 keV 10 nA Ga^+ beam. The tops of the pillars were further polished with low, 50 pA, Ga^+ beam current to minimize the depth of ion-induced crystal damage and promote high quality Electron Back Scattered Diffraction (EBSD) patterns. For the α/β micro-pillars the α -phase occupied half of the pillar diameter with the α/β grain boundary located along the axial mid-plane of the pillar.

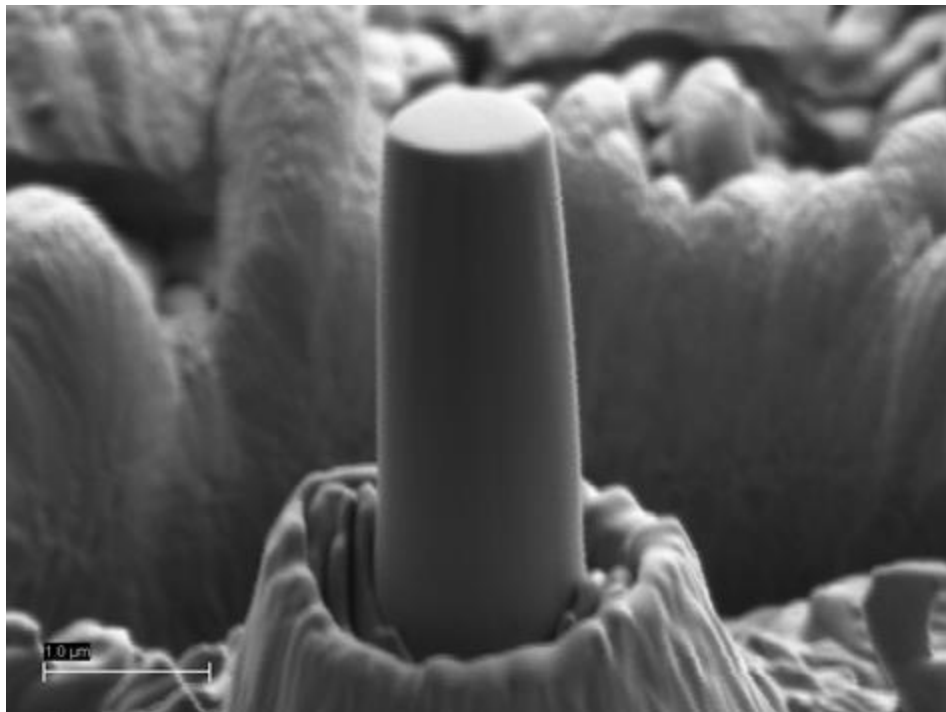


Figure 6.1: SEM image of a typical α_{Zr} -phase micro-pillar

Electron Backscattered Diffraction (EBSD) analyses were performed on the top surface of each micro-pillar to determine θ the basal misorientation angle of the α phase aligned in the axial direction of the pillar. The β_{Nb} phase of the $\alpha_{\text{Zr}}/\beta_{\text{Nb}}$ micro-pillars was not indexed by EBSD.

Half the micro-pillars were then Zr^+ implanted. The implantation was performed in vacuum at 300°C with 8.5 MeV Zr^+ ($\varphi = 7.07 \times 10^{19}$ ions/m²) at the Tandatron ion accelerator at the University of Western Ontario. This resulted in peak Zr^+ implantation depth of about 3 μm as calculated by SRIM software [13]. The average ion-induced atomic displacement ψ , expressed in units of displacement per atom (dpa), was determined using SRIM software and the Kinchin-Pease technique as [14]

$$\psi(dpa) = \frac{\varphi \times 10^8 \times \nu}{N} \quad [6.1]$$

where, φ , ion dose (ions/m²), ν is the calculated average number of atom displacements per ion and N is the atomic number density. The average damage level throughout the micro-pillar was about $\bar{\psi} \approx 6 dpa$.

The micro-pillars were then compressed at 250°C using a high-temperature nano-indentation hardness tester equipped with a 5 μm diameter diamond flat punch. These experiments were conducted at Canadian Nuclear Laboratory (Chalk River Ontario). The elevated test temperature was maintained with electric resistance heaters located on the indenter and directly below the sample. The sample-indenter assembly was allowed to equilibrate for 2 hours at 250°C prior to testing to ensure that $\pm 1^\circ C$ thermal stability was established. The compression tests were performed under constant loading rate of 0.10 mN/sec to an axial true strain of about 15%. Table 6.1 summarizes the tests performed.

Table 6.1: Listing of micro-pillar compression tests performed in this study

Ion implantation condition	Pressure tube plane from which the micro-pillar was fabricated	Number of micro-pillars tested
Non-implanted ($\bar{\psi} = 0$)	TN (α)	3 (Figure 6.2)
	TN (α/β)	3 (Figure 6.3)
Zr ⁺ Implanted ($\bar{\psi} \approx 6dpa @ 300^\circ C$)	AN (α)	4 (Figure 6.36)
	AN(α/β)	3 (Figure 6.47)
	TN (α)	3 (Figure 6.4)
	TN(α/β)	1 (Figure 6.5)
Total number of micro-pillars tested		17

6.3 Results

True stress – strain curves from all the micro-pillars tested are shown in Figure 6.2 – Figure 6.7: Figure 6.2 and Figure 6.3 show the curves for the non-implanted while Figure 6.4 and Figure 6.5 show the curves for the Zr⁺-implanted α_{Zr} and α_{Zr}/β_{Nb} micro-pillars of TN orientation. Figure 6.6 and Figure 6.7 show the curves for the Zr⁺-implanted α_{Zr} and α_{Zr}/β_{Nb} micro-pillars of AN orientation. The small size of the micro-pillars necessitates that the axial strain ε be determined from the measured deflection of the diamond flat punch which contacted the specimen. The associated load frame compliance therefore affects the magnitude of ε and resulted in an apparent elastic stiffness S which is of considerably smaller magnitude than the true elastic modulus E of the tested material. The stress – strain curves display a region of linear elastic deformation and a non-distinct elastic-plastic transition. The 0.2%-offset method was used to estimate the initial yield stress $\sigma_{0.2\%}$ (Table 6.2).

The stress-strain curves all display some post-yield strain hardening. The flow stress corresponding to 10% strain, $\sigma_{\varepsilon=10\%}$ is larger than $\sigma_{0.2\%}$ and this stress difference $\Delta\sigma$ reflects the degree of strain hardening (Table 6.2).

The resolved shear stress within the α phase corresponding to initial yielding was calculated by incorporating the EBSD-determined $\langle hkl \rangle$ α phase direction parallel to the axial direction of the pillar and Schmid's law as

$$\tau_{0.2\%} = m\sigma_{0.2\%} \quad [6.2]$$

Where the Schmid factor m is

$$m = \cos\phi\cos\lambda \quad [6.3]$$

and ϕ is the angle between the loading direction and the slip plane normal while λ is the angle between the loading direction and the slip direction. The Schmid factor corresponding to deformation by each of the following mechanisms common to the hcp α -Zr crystal: $\{0001\}\langle 0001 \rangle$ basal dislocation glide, $\{10\bar{1}0\}\langle 11\bar{2}0 \rangle$ prismatic dislocation glide, $\{10\bar{1}1\}\langle 11\bar{2}3 \rangle$ pyramidal dislocation glide, and $\{1\bar{1}02\} \langle 10\bar{1}1 \rangle$ twinning deformation was calculated. Table 2 lists the maximum m for each of the tests performed.

Post-deformation SEM images of typical TN-oriented α_{Zr} micro-pillars are shown in Figure 6.8. The Zr^+ implanted pillars but not the non-implanted pillars displayed axial cracking after deformation at 250°C. Closer examination of a cracked micro-pillar indicated that the cracks initiate at the sample surface.

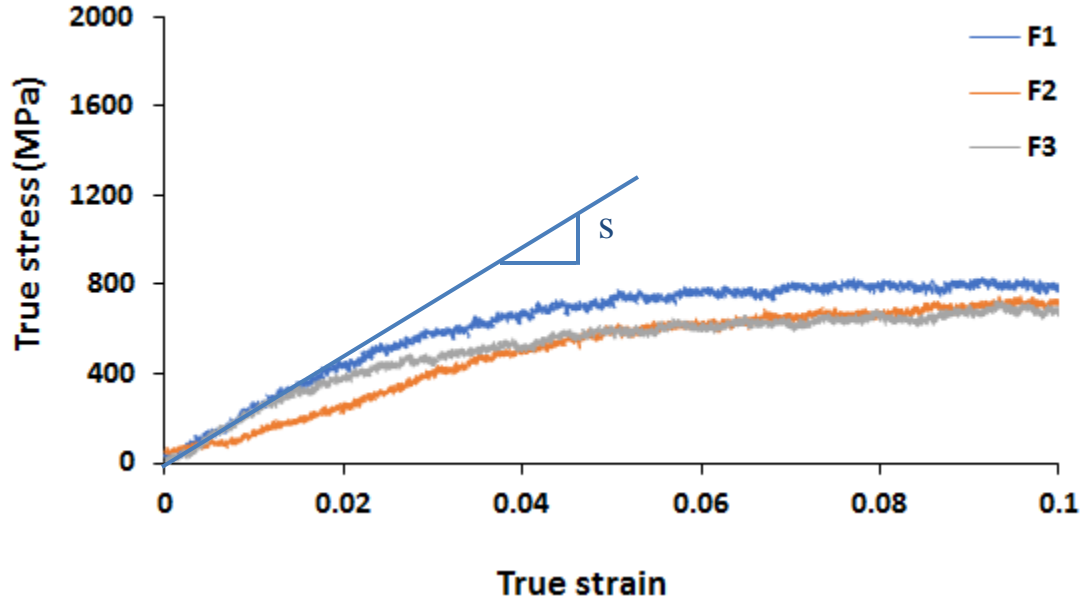


Figure 6.2: True stress versus true strain response of the TN-oriented non-implanted α_{Zr} micro-pillars compressed at 250°C

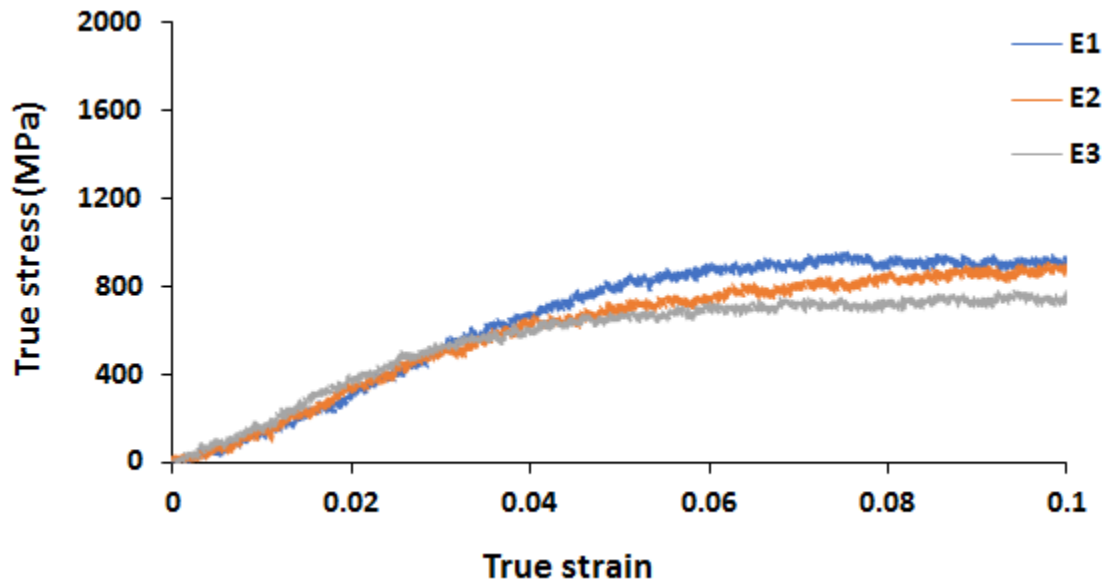


Figure 6.3: True stress versus true strain response for TN-oriented non-implanted α_{Zr} / β_{Nb} micro-pillars compressed at 250°C

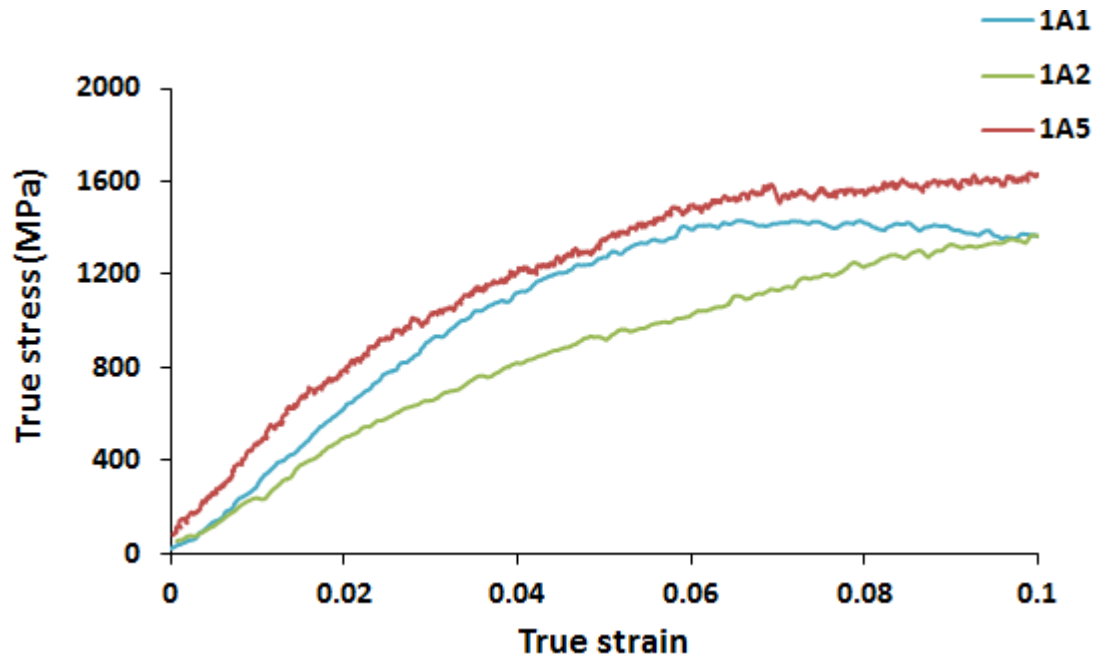


Figure 6.4: True stress versus true strain response for TN-oriented Zr⁺ implanted α_{Zr} micro-pillars compressed at 250°C

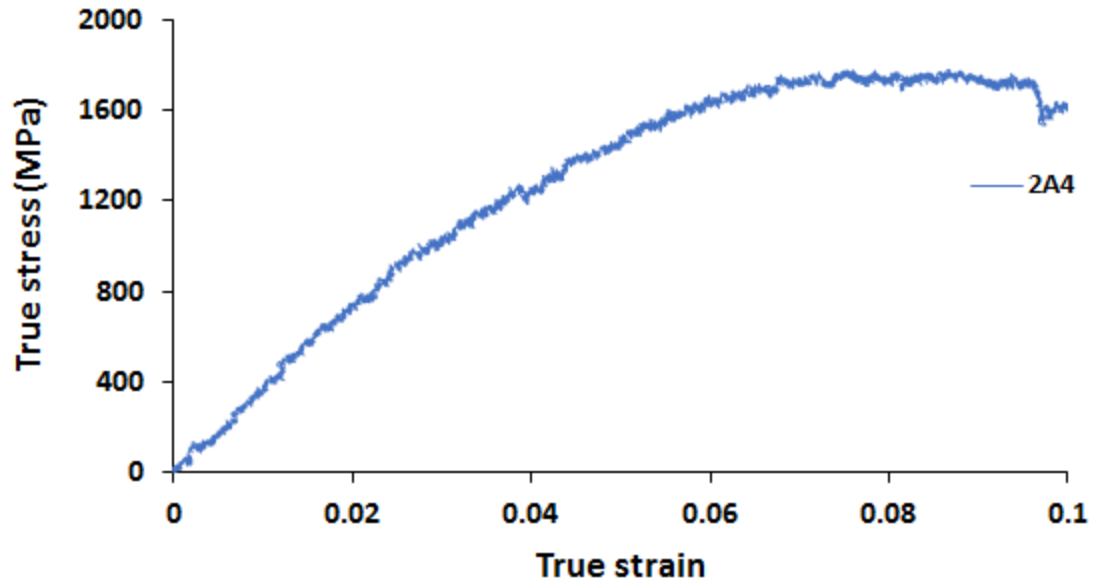


Figure 6.5: True stress versus true strain response for TN-oriented Zr^+ implanted α_{Zr} / β_{Nb} micro-pillar compressed at $250^\circ C$

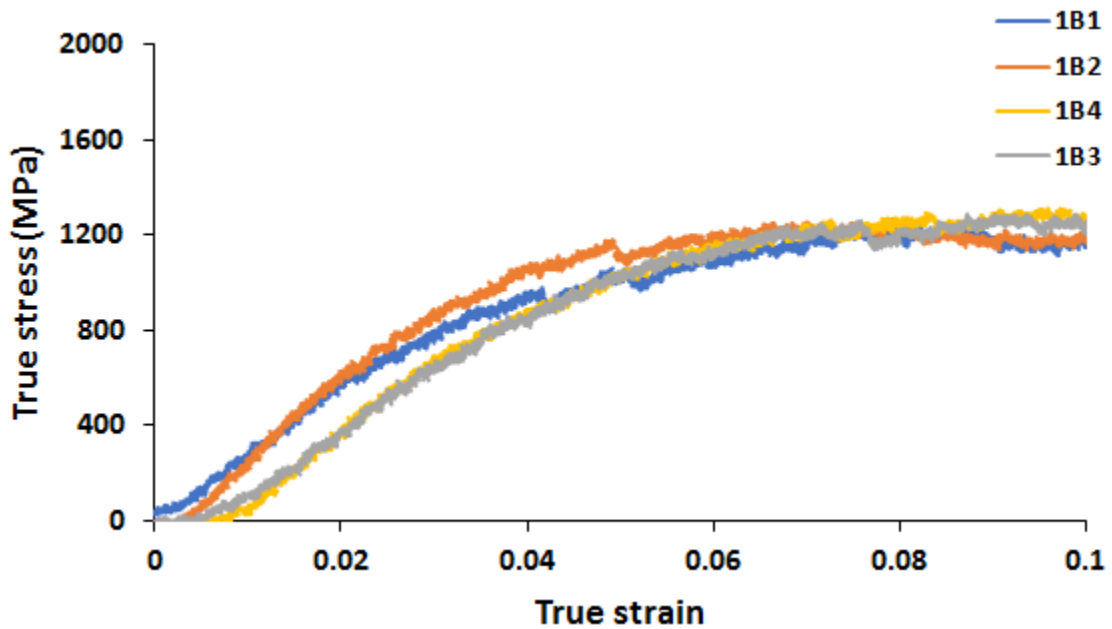


Figure 6.6 : True stress versus true strain response for AN-oriented Zr^+ implanted α_{Zr} micro-pillars compressed at $250^\circ C$

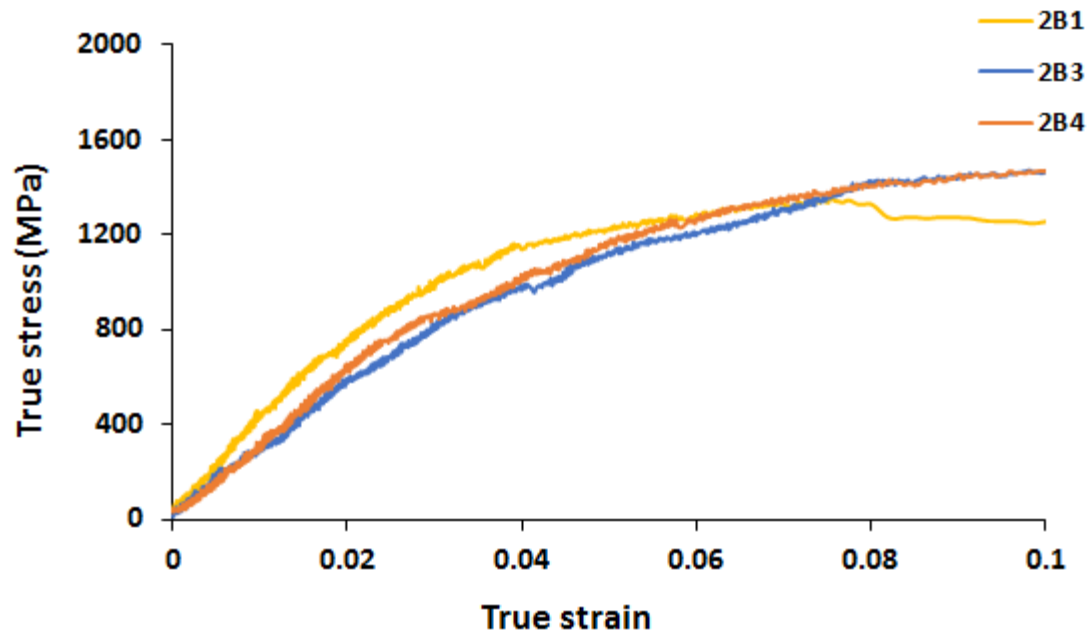


Figure 6.7: True stress versus true strain response for AN-oriented Zr^+ implanted α_{Zr} / β_{Nb} micro-pillars compressed at $250^\circ C$

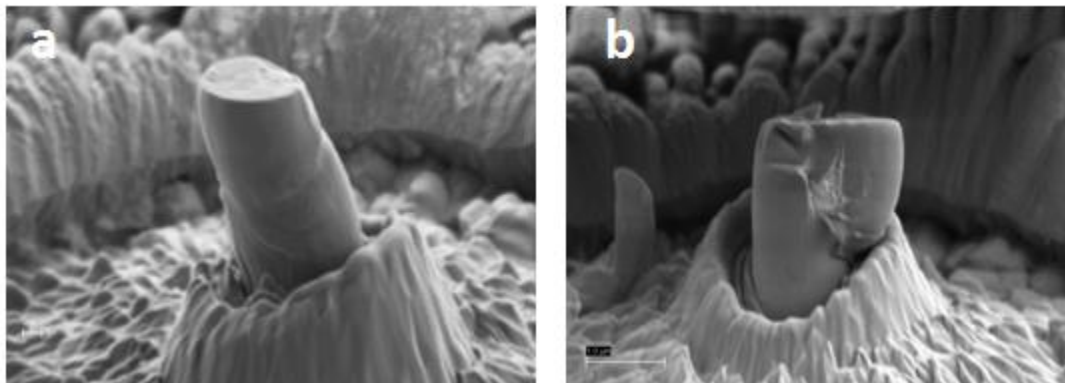


Figure 6.8: post-deformation SEM images of (a) non-implanted and (b) Zr^+ -implanted micro-pillars compressed at $250^\circ C$

Table 6.2: Listing of initial yield stress ($\sigma_{0.2\%}$), flow stress at 10% strain ($\sigma_{10\%}$), stress difference ($\Delta\sigma = \sigma_{10\%} - \sigma_{0.2\%}$), θ basal misorientation angle of the α -phase corresponding to the axial direction of the micro-pillar, maximum calculated Schmid factor m , and the critical resolved shear stress ($\tau_{0.2\%}$) for all the micro-pillars tested in this study

Ion implantation condition	Pressure tube plane on which micro-pillar was made	Microstructural phase type	$\sigma_{0.2\%}$ (MPa)	$\sigma_{10\%}$ (MPa)	$\Delta\sigma$ (MPa)	θ	m	Slip system	$\tau_{0.2\%}$ (MPa)	Specimen Designation
Non-Implanted ($\bar{\psi} \approx 0dpa$)	Transverse Normal (TN)	α	600	810	210	81.8	0.4502	Prism	270	F1
			591	722	131	21.5	0.4998	Basal	295	F2
			592	715	123	29.9	0.42	Basal	248	F3
		α/β	857	937	80	26.9	0.3315	Basal	284	E1
			706	872	166	31.7	0.4061	Basal	286	E2
			606	752	146	75	0.4489	Prism	272	E3
Zr ⁺ -Implanted ($\bar{\psi} \approx 6dpa$)	Transverse Normal (TN)	α	1040	1501	461	56.6	0.4218	Basal	438	1A1
			762	1509	747	62.1	0.4	Prism	304	1A2
			1030	1804	774	80.7	0.4502	Prism	463	1A5
		α/β	1329	1729	400	55.9	0.29	Basal	385	2A4

	Axial (AN)	Normal	α	956	1283	327	89.6	0.4373	Prism	418	1B1
				1084	1300	216	83.9	0.4332	Prism	469	1B2
				1065	1412	347	71.6	0.3605	Prism	384	1B3
				1040	1577	537	86	0.4832	Prism	502	1B4
		α/β	1117	1333	216	87.1	0.4373	Prism	488	2B1	
			1074	1567	493	83.8	0.42	Prism	451	2B3	
			1019	1562	543	81.6	0.4199	Prism	427	2B4	

6.4 Discussion

This paper presents new data on the stress-strain response, at 250°C, of α_{Zr} and α_{Zr}/β_{Nb} phase Zr-2.5Nb micro-pillars in the non-implanted and Zr⁺-implanted ($\bar{\psi} \approx 6dpa @ 300^\circ C$) conditions. The objective is to assess the effect of temperature on the flow strength, $\sigma_{0.2\%}$ and $\tau_{0.2\%}$, and the work hardening capacity, $\Delta\sigma$, of the α_{Zr} and α_{Zr}/β_{Nb} phases of irradiated Zr-2.5Nb pressure tube material.

6.4.1 Cracking of Zr⁺ implanted micro-pillars

A unique observation of this study is that the Zr⁺-implanted α_{Zr} and α_{Zr}/β_{Nb} -phase micro-pillars displayed a strong tendency to crack during uniaxial compression at 250°C (Fig. 6.8). Previous compression tests performed at 25°C on similar 300°C Zr⁺ implanted micro-pillars did not display axial cracking [10][11]. The 300°C Zr⁺ implantation was performed in high vacuum thus it is unlikely that significant oxidation of the micro-pillars occurred during the implantation process. The micro-pillars in our study however were all exposed to atmospheric air at 250°C for extended time during the compression testing.

Analysis of the degree of serration of the stress-strain response is shown in Figure 6.9 where $d\sigma/d\varepsilon$ is plotted versus ε for TN-oriented α micro-pillars tested in the Zr⁺-implanted ($\bar{\psi} \approx 6dpa @ 300^\circ C$) and tested in compression in air at 25°C and 250°C. At low values of strain, $\varepsilon < 0.04$, The variation in $d\sigma/d\varepsilon$ is significantly larger for the micro-pillars tested at 250°C than those tested at 25°C. This is consistent with a different population of obstacles, with different strength characteristics, controlling the dislocation glide process during deformation at 250°C compared to 25°C. Since all the micro-pillars

in Figure 6.9 were subjected to the same Zr^+ implantation ($\bar{\psi} \approx 6dpa @ 300^\circ C$) one can surmise that the observed axial cracking and increased serrations in the stress-strain response at $250^\circ C$ occurs by either diffusive rearrangement of ion-induced crystal damage into larger obstacles, that offer more resistance to dislocation glide, or onset of an oxygen-induced dynamic strain-aging process where ion-induced crystal defects enhance the ingress of mobile oxygen resulting in creation of new obstacles to dislocation glide. The later mechanism has been observed to operate in cold-worked Zr-2.5Nb particularly at elevated temperatures [15][16][17].

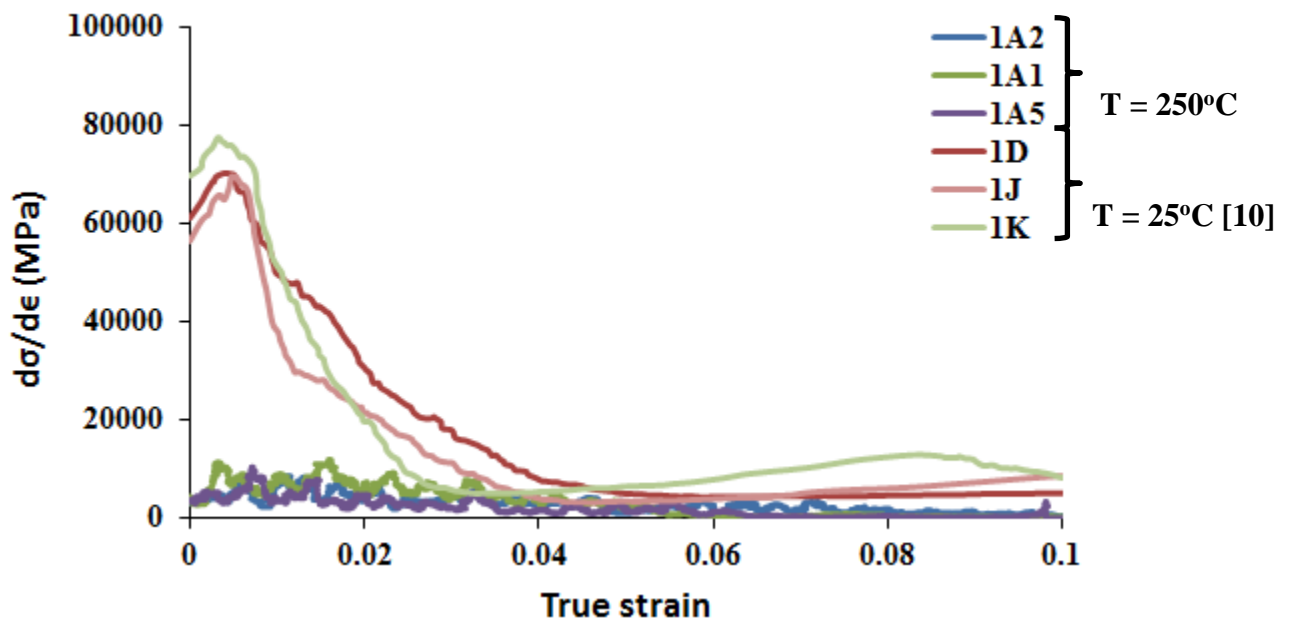


Figure 6.9: $d\sigma/d\varepsilon$ with true strain (ε) during uniaxial compression of TN-oriented α micro-pillars in the non-implanted and the Zr^+ implanted ($\bar{\psi} \approx 6dpa @ 300^\circ C$) condition. The data from the $25^\circ C$ test performed on a Zr^+ implanted micro-pillar are obtained from σ - ε data presented in Reference [10]

6.4.2 Effect of testing temperature on $\sigma_{0.2\%}$ of non-implanted micro-pillars

Figure 6.10 presents a histogram of the $\sigma_{0.2\%}$ of TN- and AN-oriented α_{Zr} - and α_{Zr}/β_{Nb} -phase micro-pillars compressed at 250°C. Figure 6.11 shows a similar histogram for previously reported $\sigma_{0.2\%}$ data from similarly Zr⁺ implanted α_{Zr} - and α_{Zr}/β_{Nb} -phase micro-pillars compressed at 25°C.

The non-implanted TN-oriented α_{Zr} - and α_{Zr}/β_{Nb} -phase micro-pillars displayed a decrease in the average $\sigma_{0.2\%}$ of about 40% and 50% when the testing temperature was increased from 25°C to 250°C. The presence of the β_{Nb} -phase in the TN-orientated non-implanted α_{Zr}/β_{Nb} micro-pillars resulted in a significant, 30% and 17%, increase in the average $\sigma_{0.2\%}$ relative to that of the non-implanted α -phase micro-pillars when tested at 25°C and 250°C. It should be noted that the volume fraction of α_{Zr} - and β_{Nb} -phases within all the α_{Zr}/β_{Nb} micro-pillars was essentially the same; 50% of the micro-pillar was pure α_{Zr} -phase while 50% was α/β lamellae.

Deformation of the non-implanted micro-pillars occurs primarily by a process of thermally-activated obstacle-limited dislocation glide [18]. The operation of this mechanism is consistent with the observed increase in $\sigma_{0.2\%}$ for the α_{Zr}/β_{Nb} micro-pillars compared to the α_{Zr} micro-pillars when tested at 25°C (Figure 6.11).

Further analysis of the data in Figures 6.10 and 6.11 indicate that, for the non-implanted α -phase micro-pillars, the yield stress anisotropy factor, $\sigma_{0.2\%TN}/\sigma_{0.2\%AN}$, decreases from about 1.5 to 0.9 with increasing testing temperature from 25°C to 250°C. This suggests that thermal activation of dislocations past obstacles in the non-implanted α -

phase occurs more rapidly upon $\{0001\}\langle 0001 \rangle$ basal slip systems which, because of the crystallographic anisotropy of the α -phase in the Zr-2.5Nb starting material, are more active during deformation of the TN oriented, than the AN oriented micro-pillars.

6.4.3 Effect of testing temperature on $\sigma_{0.2\%}$ of Zr⁺ implanted micro-pillars

The Zr⁺ implanted ($\bar{\psi} \approx 6dpa @ 300^\circ C$) micro-pillars displayed quite different temperature dependence of $\sigma_{0.2\%}$. Zr⁺ implantation resulted in 11% decrease and 34% increase in $\sigma_{0.2\%}$ for TN and AN oriented α -phase micro-pillars tested at 25°C, the average $\sigma_{0.2\%}$ increased by 35% for the Zr⁺ implanted TN-oriented α -phase micro-pillars tested at 250°C compared to 25°C.

The anisotropy factor, $\sigma_{0.2\%TN}/\sigma_{0.2\%AN}$, of the Zr⁺ implanted α -phase micro-pillars remained constant at about 0.9 for test temperatures of 25°C and 250°C. This decreased anisotropy is the result of differential ion-induced hardening along the different dislocation slip systems with prismatic dislocation slip being more inhibited than pyramidal dislocation slip [15]. The similarity of the anisotropy factor for compression tests performed on the Zr⁺ implanted micro-pillars at 25°C and 250°C indicates that the degree of differential hardening is not highly temperature dependent.

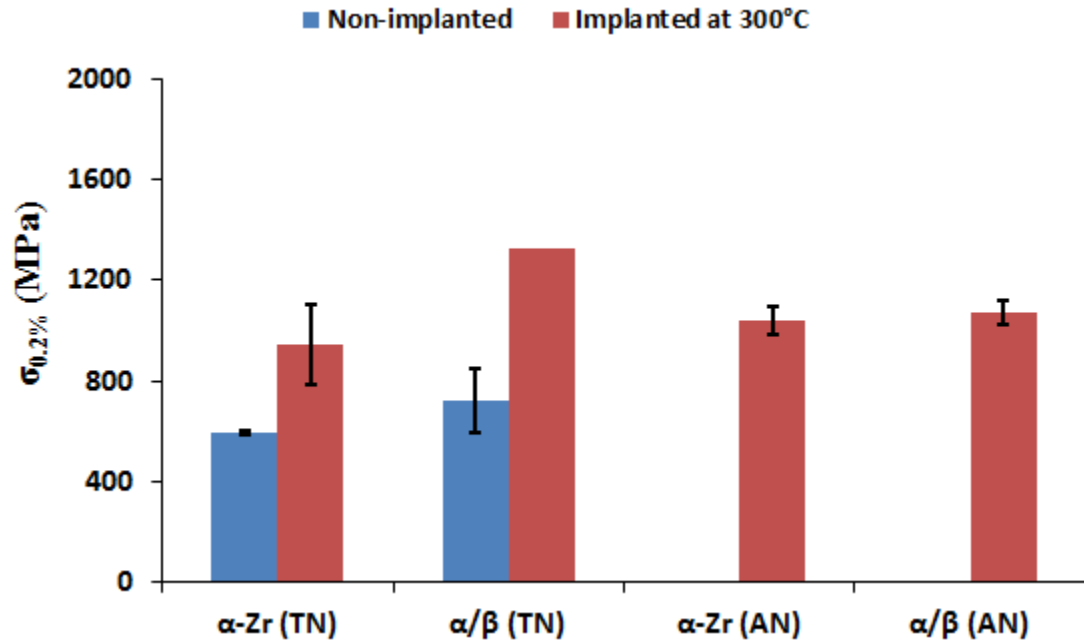


Figure 6.10: Measured average $\sigma_{0.2\%}$ from the various types of micro-pillars compressed at 250°C. The scatter bars represent the measured sample-to-sample variability in $\sigma_{0.2\%}$ as indicated by the data in Table 6.2

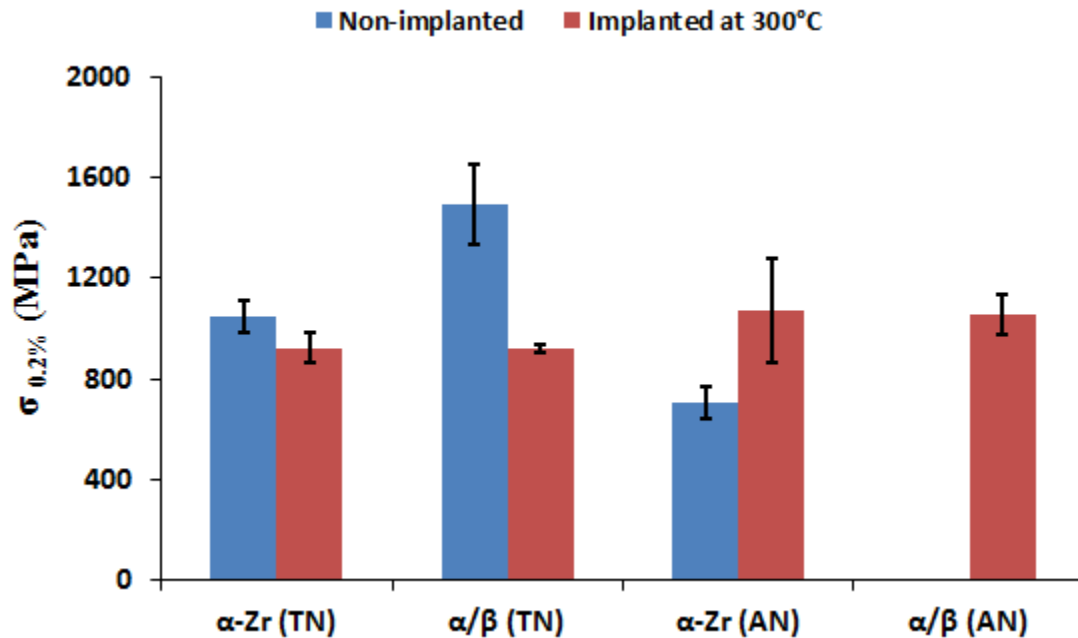


Figure 6.11: Measured average $\sigma_{0.2\%}$ from the various types of micro-pillars compressed at 25°C. The data in this plot were previously reported [10][11]

6.4.4 Effect of Zr^{+} implantation and testing temperature on strain hardening of micro-pillars

In this study we use the parameter $\Delta\sigma = \sigma_{10\%} - \sigma_{0.2\%}$ as an indication of strain-hardening capacity (Table 2). Figure 6.12 presents a histogram of $\Delta\sigma$ of TN- and AN-oriented α - and α/β -phase micro-pillars compressed at 25°C [10][11] and 250°C.

For the non-implanted α_{Zr} - and α_{Zr}/β_{Nb} -micro-pillars the strain hardening capacity is much higher for pillars compressed at 25°C compared to 250°C. For both types of non-implanted micro-pillars the decreased $\Delta\sigma$ is indicative of enhanced thermal activation of dislocations past microstructural obstacles at 250°C compared to 25°C.

Zr^{+} -implanted ($\bar{\psi} \approx 6dpa @ 300^{\circ}C$) α -phase micro-pillars tested at 25°C showed about 1.5 times higher $\Delta\sigma$ than those tested at 250°C. The α/β -phase micro-pillars displayed

lower $\Delta\sigma$ at either test temperature. To summarize, strain hardening capacity is affected by both testing temperature and prior Zr^+ implantation: Increasing the test temperature lowers $\Delta\sigma$ while Zr^+ implantation results in increases $\Delta\sigma$.

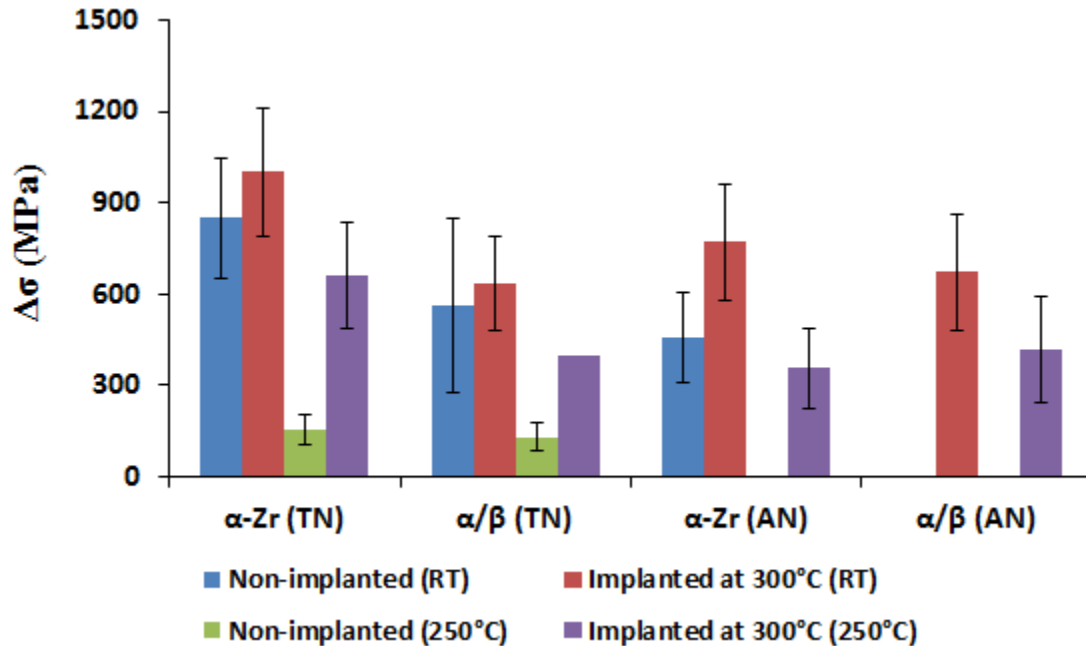


Figure 6.12: Variation of strain-hardening capacity $\Delta\sigma$ obtained from micro-pillar compression tests performed on non-implanted and Zr^+ implanted α_{Zr} - and α_{Zr}/β_{Nb} micro-pillars at 25°C (RT) 250°C. The data from the 25°C tests were obtained from σ - ϵ data reported in [10][11]

6.4.5 Orientation dependence of $\tau_{0.2\%}$ of α -phase deformation at 250°C

Figure 6.14 shows the calculated Schmid factor m (Eq. 2) for hcp α -phase deformation via the mechanisms of $\{10\bar{1}0\}\{11\bar{2}0\}$ prismatic slip, $\{0001\}\{0001\}$ basal slip, and $\{1\bar{1}02\} \langle 10\bar{1}1 \rangle$ twinning as a function of basal misorientation angle relative to the loading direction. Included in the figure are the maximum measured values of m for the TN and AN α -phase micro-pillars of this study (Table 6.2). Based on their basal

misorientation angles, the majority of the α -phase micro-pillars of this study can be divided into two general groups: i) pillars with misorientation angle between 20° and 65° , which deform primarily by basal dislocation slip, and ii) pillars with basal misorientation angle greater than 65° , which deform primarily by prismatic dislocation slip.

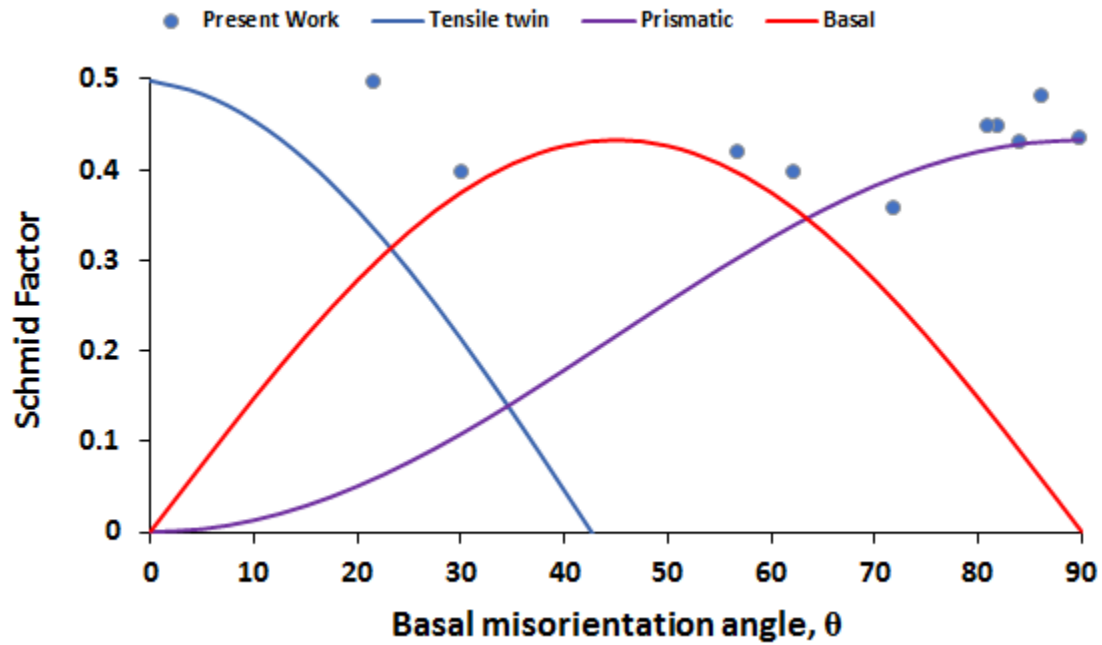


Figure 6.13 Calculated Schmid factor for deformation along $\{10\bar{1}0\}\langle 11\bar{2}0\rangle$ prismatic slip, $\{0001\}\langle 0001\rangle$ basal slip and $\{1\bar{1}02\} \langle 10\bar{1}1 \rangle$ twinning systems (solid lines) as a function of basal misorientation angle with respect to the loading direction. Superimposed on the curves are the measured maximum Schmid Factors m for each of the α -micro-pillars of this study (Table 6.2)

Figure 6.14 shows the variation of temperature normalized resolved shear stress

$$\hat{\tau} = \tau_{0.2\%} / \tau_{0.2\%_{298K}} \quad [6.4]$$

for α -phase micro-pillars aligned for deformation by $\{0001\}\langle 0001 \rangle$ basal slip and $\{10\bar{1}0\}\langle 11\bar{2}0 \rangle$ prismatic slip as a function of testing temperature. The $\hat{\tau}$ values for the selected micro-pillars from this study were obtained by normalizing the measured $\tau_{0.2\%}$ (Table 2) with respect to $\tau_{0.2\%_{298K}}$ obtained from similar α -phase micro-pillars reported previously [10]. $\hat{\tau}$ of our non-implanted micro-pillars follow the same temperature dependence as data from other studies; namely, $\hat{\tau}$ decreases as testing temperature increases. This is consistent with the expected increased thermal activation of dislocation glide past microstructural obstacles that occurs at 250°C compared to 25°C. The α -phase micro-pillars oriented for preferred basal dislocation slip show the same $\hat{\tau} - T$ trend as those oriented for preferred prismatic dislocation slip, indicating that the kinetics of thermally-activated dislocation glide is largely the same for both deformation mechanisms in the non-implanted α -phase.

Unlike the non-implanted case, the Zr^+ implanted ($\bar{\psi} \approx 6dpa @ 300^\circ C$) micro-pillars that were aligned for preferred prismatic dislocation slip displayed an increasing $\hat{\tau}$ with increasing testing temperature while those aligned for basal dislocation slip displayed a decreasing $\hat{\tau}$ with increasing testing temperature (Figure 14). This increase in $\hat{\tau}$ indicate that prior Zr^+ implantation at 300°C tends to enhance diffusion agglomeration of oxygen and/or Zr^+ -induced crystal defects to create stronger obstacles to dislocation glide on prismatic slip systems but not basal slip systems at 250°C. It has been previously

reported that the critical resolved shear stress for dislocation glide decreases more rapidly with increasing temperature on basal than on prismatic slip systems [19][20][21].

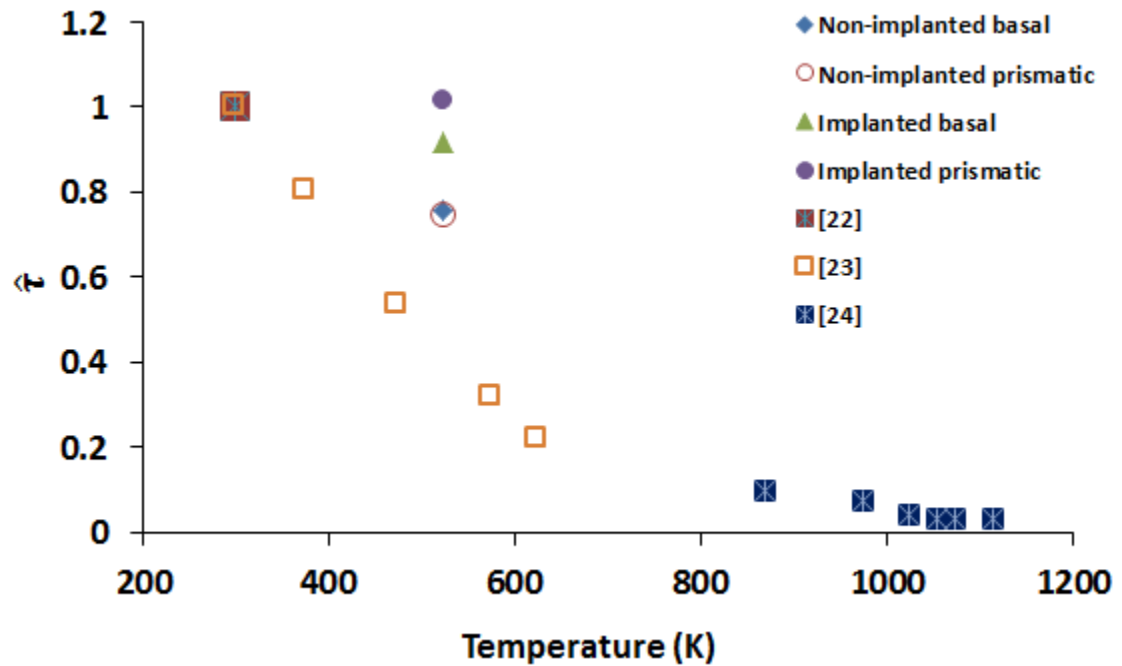


Figure 6.14: variation of $\hat{\tau}$ with temperature for hcp α -phase Zr-2.5Nb subjected to $\{0001\}\langle 0001 \rangle$ basal slip deformation [22][23][24]. Included in the plot are $\hat{\tau}$ data from tests performed in this study and in our previous study [10] for α -phase samples subjected to $\{0001\}\langle 0001 \rangle$ basal slip and $\{10\bar{1}0\}\langle 11\bar{2}0 \rangle$ prismatic slip deformation

6.5 Conclusions

In this study we investigated the uniaxial compressive flow stress, at 250°C, of FIB-fabricated α - and α/β -phase micro-pillars (1 μm diameter and 3 μm height) made from Zr-2.5%Nb pressure tube material. The micro-pillars were fabricated from the AN and TN planes of the pressure tube and were tested in the non-implanted and Zr⁺-implanted

($\bar{\psi} \approx 6dpa @ 300^\circ C$) conditions. The dependence upon testing temperature of yield strength $\sigma_{0.2\%}$, critical resolved shear stress $\tau_{0.2\%}$, and strain hardening capacity $\Delta\sigma$ were assessed.

Surface cracking was observed to occur in all of the Zr^+ implanted micro-pillars. This was in contrast to the non-implanted micro-pillars, tested at $250^\circ C$, and similarly Zr^+ implanted micro-pillars tested at $25^\circ C$ which did not display surface cracking. The surface cracking was accompanied by increased serration in the stress – strain response. These findings indicate that prior Zr^+ implantation results in increased brittleness and unstable plastic deformation at $250^\circ C$. We suggest that this occurs either by thermally - enhanced rearrangement of ion-induced crystal damage into larger obstacles that offer more resistance to dislocation glide or to the onset of an oxygen-induced dynamic strain-aging process whereby ion-induced crystal defects enhance the ingress of mobile oxygen resulting in creation of stronger obstacles to dislocation glide.

The anisotropy factor, $\sigma_{0.2\%TN}/\sigma_{0.2\%AN}$, of non-implanted α -phase micro-pillars decreased from about 1.5 to 0.9 with increasing testing temperature from $25^\circ C$ to $250^\circ C$ whereas it remained essentially unchanged at about 0.9 for the Zr^+ implanted micro-pillars tested over the same temperature range. This suggests that, for the non-implanted α -phase, increasing the testing temperature results in proportionally greater reduction in the critical resolved shear stress for $\{0001\}\{0001\}$ basal dislocation slip, which is the primary deformation mode of the TN micro-pillars, compared to $\{10\bar{1}0\}\{11\bar{2}0\}$ prismatic dislocation slip, which is the primary deformation mode of the AN micro-pillars. The decreased anisotropy displayed by the Zr^+ implanted micro-pillars confirms previous

findings that $\{10\bar{1}0\}\langle 11\bar{2}0\rangle$ prismatic dislocation slip is more inhibited by Zr^{+} -induced microstructural defects than $\{0001\}\langle 0001\rangle$ basal dislocation slip. The similarity of the anisotropy factor for Zr^{+} implanted micro-pillars tested at 25°C and 250°C indicates that the degree of differential hardening is not highly temperature dependent.

The strain hardening capacity, $\Delta\sigma$, of both the non-implanted and the Zr^{+} implanted α -phase micro-pillars decreased with increasing test temperature from 25°C to 250°C however the magnitude of $\Delta\sigma$, at a given temperature, was increased for the Zr^{+} implanted micro-pillars. Increasing the testing temperature therefore lowers $\Delta\sigma$ by increasing the rate of thermal activation of dislocation past microstructural obstacles while Zr^{+} implantation increases $\Delta\sigma$ via implantation-induced crystal defects which act as obstacles to dislocation glide.

The temperature-normalized critical resolved shear stress $\hat{\tau}$ of our non-implanted α -phase micro-pillars aligned for both basal and prismatic dislocation glide and our Zr^{+} implanted micro-pillars aligned for basal dislocation glide displayed decreasing $\hat{\tau}$ with increasing temperature from 25°C to 250°C. This is consistent with increased thermal activation of dislocation glide past microstructural obstacles that occurs at 250°C. Since, in the non-implanted case, the α -phase micro-pillars oriented for preferred basal dislocation slip show the same $\hat{\tau} - T$ trend as those oriented for preferred prismatic dislocation slip indicating that the kinetics of the thermally-activated dislocation glide was largely the same.

The Zr^{+} implanted α -phase micro-pillars that were aligned for preferred prismatic dislocation slip displayed an increasing $\hat{\tau}$ with increasing testing temperature. This

indicates that prior Zr^{+} implantation followed by prolonged exposure to air at 250°C tends to result in stronger obstacles to dislocation glide on prismatic slip systems than on basal slip systems.

The experimental data presented in this paper will be helpful for life-cycle assessment of pressure tubes in the existing reactors and predicting the material properties of Zr-2.5%Nb alloy at high temperature.

6.6 Acknowledgements

The authors acknowledge the support of Dr. T. Simpson of the University of Western Ontario (UWO) Nanofabrication Laboratory for his assistance in preparing the micro-pillars and Mr. J. Hendriks of the UWO Tandetron Laboratory for his support in performing the Zr^{+} implantations. The help of Mr. I. Barker and Prof. D. Moser of the UWO ZAP lab in the performance of the EBSD experiments is also acknowledged. The help of Drs. V. Bhakhri and S. St. Lawrence of the Canadian Nuclear Laboratory for supplying the test materials and performing the 250°C micro-pillar compression tests is gratefully acknowledged. The help of Prof. H. Abdolvand of the UWO for useful discussions and suggestions related to interpretation of the EBSD results is also gratefully acknowledged. Finally, we acknowledge the generous financial support of this research by the Candu Owners Group of Canada (<http://www.candu.org>).

References

- [1] D. D. Himbeault, C. K. Chow, and M. P. Puls, “Deformation Behavior of Irradiated Zr-2.5Nb Pressure Tube Material,” *Metall. Trans. A, Phys. Metall. Mater. Sci.*, vol. 25, no. 1, pp. 135–145, 1994.

- [2] F. Long *et al.*, “Effect of neutron irradiation on deformation mechanisms operating during tensile testing of Zr-2.5Nb,” *Acta Mater.*, vol. 102, pp. 352–363, 2016.
- [3] N. Christodoulou, P. A. Turner, E. T. C. Ho, C. K. Chow, and M. R. Levi, “Anisotropy of Yielding in a Zr-2.5Nb Pressure Tube Material,” *Met. Mat Trans A*, vol. 31, no. February, pp. 409–420, 2000.
- [4] Y. S. Kim, “Role of Twinning and Slip in Deformation of a Zr-2.5Nb Tube,” in *Zirconium in the Nuclear Industry: 15th International Symposium*, B. Kammenzind and M. Limbäck, Eds. West Conshohocken, PA: ASTM International, 2009, pp. 227–243.
- [5] M. Gallagher *et al.*, “Variations in nanomechanical properties of back-end Zr-2.5Nb pressure tube material,” *J. Nucl. Mater.*, vol. 442, no. 1–3, pp. 116–123, Nov. 2013.
- [6] Q. Wang, F. Long, Z. Wang, N. Guo, and M. R. Daymond, “Orientation dependent evolution of plasticity of irradiated Zr-2.5Nb pressure tube alloy studied by nanoindentation and finite element modeling,” *J. Nucl. Mater.*, vol. 512, pp. 371–384, 2018.
- [7] Q. Wang, C. Cochrane, F. Long, H. Yu, and M. R. Daymond, “Micropillar compression study on heavy ion irradiated Zr-2.5Nb pressure tube alloy,” *J. Nucl. Mater.*, vol. 511, pp. 487–495, 2018.
- [8] R. O. Oviasuyi and R. J. Klassen, “Assessment of the anisotropic flow stress and plastic strain of Zr-2.5%Nb pressure tubes at temperature from 25 °c to 300 °c,” *J.*

- Nucl. Mater.*, vol. 429, no. 1–3, pp. 7–12, 2012.
- [9] R. O. Oviasuyi and R. J. Klassen, “Anisotropic deformation of Zr ion irradiated Zr-2.5%Nb micro-pillars at 25 °c,” *J. Nucl. Mater.*, vol. 421, no. 1–3, pp. 54–57, 2012.
- [10] M. I. Khan and R. J. Klassen, “Effect of Zr⁺ implantation and crystal orientation on the uniaxial deformation of Zr-2.5%Nb micro-pillars: Part 1, Deformation of single-phase α -Zr micro-pillars,” *Can. Metall. Q. Submitted*
- [11] M. I. Khan and R. J. Klassen, “Effect of Zr⁺ implantation and crystal orientation on the uniaxial deformation of Zr-2.5%Nb micro-pillars: Part 2, Deformation of two-phase alpha/beta micro-pillars,” *Can. Metall. Q. Submitted*.
- [12] A. Kunz, S. Pathak, and J. R. Greer, “Size effects in Al nanopillars: Single crystalline vs. bicrystalline,” *Acta Mater.*, vol. 59, no. 11, pp. 4416–4424, Jun. 2011.
- [13] R. E. Stoller, M. B. Toloczko, G. S. Was, A. G. Certain, S. Dwaraknath, and F. A. Garner, “On the use of SRIM for computing radiation damage exposure,” *Nucl. Instruments Methods Phys. Res.*, vol. 310, no. September, pp. 75–80, 2013.
- [14] M. Li, M. A. Kirk, P. M. Baldo, D. Xu, and B. D. Wirth, “Study of defect evolution by TEM with in situ ion irradiation and coordinated modeling,” *Philos. Mag.*, vol. 92, no. 16, pp. 2048–2078, 2012.
- [15] R. O. Oviasuyi and R. J. Klassen, “Anisotropic deformation of Zr ion irradiated Zr

- 2.5 % Nb micro-pillars at 25 ° C,” *J. Nucl. Mater.*, vol. 421, no. 1–3, pp. 54–57, 2012.
- [16] R. Thomas *et al.*, “Materialia Characterisation of irradiation enhanced strain localisation in a zirconium alloy,” *Materialia*, vol. 5, no. February, p. 100248, 2019.
- [17] L. Balogh, D. W. Brown, P. Mosbrucker, F. Long, and M. R. Daymond, “Dislocation structure evolution induced by irradiation and plastic deformation in the Zr-2.5Nb nuclear structural material determined by neutron diffraction line profile analysis,” *Acta Mater.*, vol. 60, no. 15, pp. 5567–5577, 2012.
- [18] D. Caillard, M. Rautenberg, and X. Feugas, “Dislocation mechanisms in a zirconium alloy in the high-temperature regime: An in situ TEM investigation,” *Acta Mater.*, vol. 87, pp. 283–292, 2015.
- [19] A. Akhtar, “Prismatic slip in zirconium single crystals at elevated temperatures,” *Metall. Trans. A*, vol. 6, no. 6, pp. 1217–1222, 1975.
- [20] I. J. Beyerlein and C. N. Tomé, “A dislocation-based constitutive law for pure Zr including temperature effects,” *Int. J. Plast.*, vol. 24, no. 5, pp. 867–895, May 2008.
- [21] M. Knezevic, M. Zecevic, I. J. Beyerlein, J. F. Bingert, and R. J. McCabe, “Strain rate and temperature effects on the selection of primary and secondary slip and twinning systems in HCP Zr,” *Acta Mater.*, vol. 88, pp. 55–73, 2015.

- [22] J. Gong, T. Benjamin Britton, M. A. Cuddihy, F. P. E. Dunne, and A. J. Wilkinson, "(a) Prismatic, (a) basal, and (c+a) slip strengths of commercially pure Zr by micro-cantilever tests," *Acta Mater.*, vol. 96, pp. 249–257, 2015.
- [23] S. Wang, F. Giuliani, and T. Ben Britton, "Variable temperature micropillar compression to reveal b a N basal slip properties of Zircaloy-4," *Scr. Mater.*, vol. 162, pp. 451–455, 2019.
- [24] A. Akhtar, "Basal slip in zirconium," *Acta Metall.*, vol. 21, no. 1, pp. 1–11, 1973.

Chapter 7

7 Discussion and Future Works

7.1 Discussions

This chapter summarizes the key results of the three previous chapters. In addition a general discussion correlating these results with the objectives of the thesis and recommendations for future work is also provided. As a recap, the prime objective of this research project was to investigate the mechanical properties of Zr^{+} implanted Zr-2.5%Nb alloy pressure tubes at the micron length scale at different temperatures. To obtain localized mechanical properties, micropillar shaped samples were prepared with and without interfaces. And these samples were compressed at room temperature and at 250° to investigate the effect of test temperature on deformation.

In chapter 4, micropillars were prepared with only α_{Zr} phase in the pillar top to assess the micromechanical deformation mechanism of this single phase. It is really important to know the properties of this phase as it occupies the largest volume fraction of the Zr-2.5%Nb microstructure. The α_{Zr} phase is present in other important zirconium alloys such as Zircaloy calandria tubing and fuel sheath material. In our study, the micro-pillars were implanted to an average crystal damage level of 6dpa at room temperature and at 300°C. These results were compared with non-implanted pillars. Length scale dependence was observed for the non-implanted samples; the compressive strength was significantly higher compared to bulk polycrystalline samples. The typical anisotropy of Zr-2.5%Nb was also present at micron length scale but anisotropic ratio was higher compared to bulk samples. Although Zr^{+} implantation at both temperatures hardened the samples, the effect was reduced at higher implantation temperature. This is most likely due to increased

strain localization, and our observation of increased serration in the stress-strain response suggests that irradiation damage implanted at elevated temperature, 300°C compared to 25°C, promotes strain localization. The normalized shear stress displayed an initial increase and after that a decreasing trend with the increase of basal misorientation angle.

In chapter 5, the pillars were implanted and compressed in a similar fashion to chapter 4. The important difference being that the pillar top surface had alternate layers of α_{Zr}/β_{Nb} interface with half of the pillar top occupied by α_{Zr} phase. This experiment was conducted to observe the effect of the presence of interfaces on the deformation of implanted and non-implanted samples. It was observed that for α_{Zr} and α_{Zr}/β_{Nb} pillars fabricated in the TN direction there was not much difference in $\bar{\sigma}_{(\epsilon=0.10)}$ value in both non-implanted and room temperature implantation conditions. However, with the increase in implantation temperature the strength of α_{Zr}/β_{Nb} micropillars was decreased by about 20%. Increased local fluctuations in σ - ϵ curves indicate increased thermally activated recovery at higher implantation temperature. It was also observed that the presence of the α_{Zr}/β_{Nb} interfaces influences the orientation dependence of the deformation.

Chapter 6, presents the deformation mechanism of implanted and non-implanted Zr-2.5%Nb micropillars compressed at 250°C. Surface cracking was observed in micropillars implanted at 300°C. These cracks were not present in non-implanted samples or samples implanted at room temperature. As the surface cracking was accompanied by increased serration in the stress-strain response, this is probably because of thermally enhanced rearrangement of ion-induced crystal damage into larger obstacles.

With the increase in test temperature, anisotropy factor, $\sigma_{0.2\%TN}/\sigma_{0.2\%AN}$ for non-implanted samples decreased significantly. For the implanted samples increase in test temperature did not have noticeable impact on anisotropy factor. Anisotropy factor remaining the same for Zr^{+} implanted micro-pillars tested at 25°C and 250°C is probably an indication that hardening of AN and TN phases is not highly temperature dependent. With the increase in test temperature, for non-implanted samples critical resolved shear stress decrease for both basal and prismatic dislocation glide. Whereas for implanted samples, the critical resolved shear stress value for prismatic slip remained unchanged indicating the presence of strong obstacle to dislocation glide.

In previous research, typically single crystal or bicrystal Zr alloy samples were fabricated from very large α -grain size annealed samples, usually of pure Zr or Zr-Sn (Zircaloy) composition. To the best of our knowledge the present thesis research is the first to report direct experimental evidence for the length scale dependence of the uniaxial flow stress of α_{Zr} phase and α_{Zr}/β_{Nb} - phases of extruded and cold-drawn for Zr-2.5%Nb pressure tube material.

Anisotropic ratio was around 1.5 for non-implanted samples at micron length scale compared to 1.2-1.3 for bulk polycrystalline samples. Ion implantation results in decreased anisotropy as it selectively hardens the slip systems. As a general rule, it can be stated that increase in implantation temperature and test temperature results in decreased anisotropy due to thermally activated dislocation glide.

Although it is mentioned in literature that axial normal samples observe more strain hardening compared to transverse normal samples. In our experiments we did not observe

this trend. The probable reason could be that the results in literature are from bulk samples, which means those samples had strong texture. But in our case, as the pillar top had single phase we observed that pillars fabricated from both the axial normal and transverse normal direction of pressure tube had similar basal misorientation angle. It was also observed that the basal misorientation angle has strong influence on the deformation of α_{Zr} micropillars.

The results presented in this thesis are novel and provide valuable information regarding the deformation of Zr-2.5%Nb alloy at sub-micron length scale. The mechanical properties of α_{Zr} and $\alpha_{\text{Zr}}/\beta_{\text{Nb}}$ micropillars at various implantations and test temperatures would be helpful for assessing the ductile fracture due to surface cracks.

7.2 Future Works

Although the present work accumulated a considerable amount of new data, there were a few limitations. If these issues are addressed in future, it would build upon our findings and lead to a more complete understanding of the micromechanical deformation of Zr-2.5%Nb alloys. Specific suggestions for future work are provided below.

The nano-indentation machine used for room temperature experiments was ex-situ, the high temperature experiments were conducted in-situ at Chalk River Laboratories. We applied load-controlled compression system, which is good for gathering mechanical properties. But to obtain deformation related properties, namely to investigate the slip planes activated during deformation, a nano-indentation machine with in-situ observation ability is more desirable with displacement-controlled mode. As in displacement-

controlled mode you can apply load to create specific amount of displacement and then observe the deformation in-situ.

All these experiments were conducted in a fixed strain rate. Conducting these experiments at variable strain rate would allow us to understand the strain rate dependent variation of mechanical properties at sub-micron length scale.

Detailed EBSD mapping of the general sample surface, instead of just the surface of already fabricated micro-pillars, would have allowed a selection of micro-pillars with a larger range of angular misorientation to be constructed and tested. This would have greatly improved the investigation of the dependence of the critical resolved shear stress upon basal plane normal-loading axis misorientation. In-situ TEM compressions of implanted micro-pillars at different temperatures could be done to directly image the interaction of ion-induced crystal defects with moving dislocations during the plastic deformation process.

Curriculum Vitae

Name:	Md Imran Khan
Post-secondary Education and Degrees:	Concordia University Montreal, Quebec, Canada
	2010-2013 MASC in Mechanical Engineering MASC thesis title: Influence of Cooling Rate on Microsegregation Behavior of Magnesium Alloys
	2004-2009 BSc in Mechanical Engineering Bangladesh University of Engineering and Technology Dhaka-1000, Bangladesh
Honours and Awards:	Western Engineering Scholarship (WES) 2014-2018
	Partial tuition fee remission scholarship (Concordia University) 2010-2011
Related Work	Teaching Assistant
Experience	The University of Western Ontario 2014-2018 Research Assistant The University of Western Ontario 2014-2019

Refereed Journal and Conference Publications

1. Md. Imran Khan and R. J. Klassen, Micromechanics of plasticity of Zr-2.5%Nb alloy, 11th International Conference on CANDU® Maintenance and Nuclear Components October 1-4, 2017, Toronto, Ontario, Canada
2. Md. Imran Khan and R. J. Klassen, Effect of Zr+ implantation and crystal orientation on the uniaxial deformation of Zr-2.5%Nb micro-pillars: Part 1, Deformation of single-phase α -Zr micro-pillars, Submitted in Canadian Metallurgical Quarterly
3. Md. Imran Khan and R. J. Klassen, Effect of Zr+ implantation and crystal orientation on the uniaxial deformation of Zr-2.5%Nb micro-pillars: Part 2, Deformation of two-phase α/β micro-pillars, Submitted in Canadian Metallurgical Quarterly
4. Md. Imran Khan and R. J. Klassen Deformation of Zr+ implanted Zr-2.5%Nb alloy at 250°C, to be submitted in Journal of Nuclear Materials